

# **An Experimentally-validated Agent-based Model to Study the Emergent Behavior of Bacterial Communities**

Eric Leaman

Thesis submitted to the faculty of the Virginia Polytechnic Institute and State University in  
partial fulfillment of the requirements for the degree of

Master of Science  
In  
Mechanical Engineering

Bahareh Behkam, Chair

Mark R. Paul

Ryan S. Senger

December 9<sup>th</sup>, 2016  
Blacksburg, VA

Keywords: chemotaxis, quorum sensing, quorum quenching, flagellated bacteria, computational  
biology

Copyright © 2016 Eric Leaman

# An Experimentally-validated Agent-based Model to Study the Emergent Behavior of Bacterial Communities

Eric Leaman

## Academic Abstract

Swimming bacteria are ubiquitous in aqueous environments ranging from oceans to fluidic environments within a living host. Furthermore, engineered bacteria are being increasingly utilized for a host of applications including environmental bioremediation, biosensing, and for the treatment of diseases. Often driven by chemotaxis (*i.e.* biased migration in response to gradients of chemical effectors) and quorum sensing (*i.e.* number density dependent regulation of gene expression), bacterial population dynamics and emergent behavior play a key role in regulating their own life and their impact on their immediate environment. Computational models that accurately and robustly describe bacterial population behavior and response to environmental stimuli are crucial to both understanding the dynamics of microbial communities and efficiently utilizing engineered microbes in practice. Many existing computational frameworks are finely-detailed at the cellular level, leading to extended computational time requirements, or are strictly population scale models, which do not permit population heterogeneities or spatiotemporal variability in the environment. To bridge this gap, we have created and experimentally validated a scalable, computationally-efficient, agent-based model of bacterial chemotaxis and quorum sensing (QS) which robustly simulates the stochastic behavior of each cell across a wide range of bacterial population sizes. We quantitatively and accurately capture emergent behavior in both isogenic QS populations and the altered QS response in a mixed QS and quorum quenching (QQ) microbial community. Finally, we show that the model can be used to predictively design synthetic genetic components towards programmed microbial behavior.

# An Experimentally-validated Agent-based Model to Study the Emergent Behavior of Bacterial Communities

Eric Leaman

## **General Audience Abstract**

Bacteria are an integral part of life and possess a host of characteristics that make them a powerful tool with which to confront many modern day problems. Using genetic engineering and the burgeoning field of synthetic biology, these single-celled organisms can be manipulated to perform many useful tasks such as detecting oil spills or other environmental pollutants, producing pharmaceuticals such as insulin, and even invading and killing cancer cells. Accurate computational simulations of microbial behavior will aid in the efficient design of such synthetic bacteria-based systems and reduce dependency on the current time-intensive “guess and check” paradigm. Towards this goal, we have built a comprehensive computer simulation of bacterial swimming behavior, response to chemo-effector concentration gradients called chemotaxis, a form of microbial communication called quorum sensing (QS), and a form of communication disruption called quorum quenching (QQ). Not only do we demonstrate an unprecedented level of accuracy in predicting experimental results, but we also couple the simulation with synthetic biology to precisely tune bacteria QS behavior, neither of which have previously been reported in literature. The overarching outcome of this thesis is a tool that could be used to improve the design process of useful bacteria-based systems in diverse areas of biotechnology.

## **Acknowledgements**

Foremost, I wish to thank my advisor Prof. Bahareh Behkam for giving me the opportunity to work in her lab and for her continuous support throughout this endeavor. Her strive to complete every aspect of her work with unmatched quality, coupled with enthusiasm and a desire to help others succeed has benefitted me immensely as a developing researcher. I greatly look forward to continuing my work towards a Ph.D. in the MicronBASE laboratory. I also wish to thank Prof. Mark Paul and Prof. Ryan Senger for their time spent serving on my committee and their insightful comments regarding this work, as well as everything I have learned from them during my studies.

I also wish to acknowledge and thank the past and present members of MicronBASE, Matt Long, Kellen Weigland, Carmen Damico, Chris Suh, Zhou Ye, Carolyn Mottley, Appy Mukherjee, Ying Zhan, and Peter Windes. In particular, I appreciate the numerous research discussions I've had with Carmen and Chris, all of the help with microfabrication from Zhou, Carolyn's help with questions regarding biology and chemistry, and Peter's help with computational modeling. Additionally, I greatly appreciate the advice of Pedro Silva from Dr. Senger's lab regarding RBS design and substitution, and I wish to thank Dr. Yong Woo Lee and Jamelle Simmons for generously providing the equipment and support for preliminary microplate experiments.

I am very grateful for my wonderful family who has supported me throughout my life and in my many interests over the years. My sister Christy deserves special recognition for her numerous last minute proof-reads of my work and from whom I have gained much of my writing skill.

Finally, I am thankful to the mechanical engineering department and to the Institute for Critical Technology and Applied Science at Virginia Tech for the opportunity to study here. This

work has been partially supported by the National Science Foundation (IIS-117519 and CAREER award, CBET-1454226).

# Table of Contents

<b>Academic Abstract</b> .....	<b>ii</b>
<b>General Audience Abstract</b> .....	<b>iii</b>
<b>Acknowledgements</b> .....	<b>iv</b>
<b>List of Figures</b> .....	<b>viii</b>
<b>List of Tables</b> .....	<b>x</b>
<b>Nomenclature</b> .....	<b>xi</b>
<b>Chapter I: Introduction</b> .....	<b>1</b>
1.1 Motivation.....	1
1.2 Background .....	2
1.2.1 Bacterial Motility .....	3
1.2.2 Chemotaxis in <i>E. coli</i> .....	6
1.2.3 Bacterial Quorum Sensing .....	9
1.3 Classifications of Models and a Review of the State-of-the-art .....	12
1.3.1 The Keller-Segel Model.....	13
1.3.2 Agent-based Modeling.....	14
1.4 Objectives and Organization of the Thesis .....	16
<b>Chapter II: Computational Framework and Agent-based Modeling</b> .....	<b>19</b>
2.1 Modeling Basic Bacterial Motility: Run-and-tumble in the Absence of a Chemo-effector	19
2.2 Modeling Bacterial Chemotaxis .....	24
2.3 Modeling Quorum Sensing .....	26
2.4 Modeling Quorum Quenching .....	30
2.5 Modeling Bacterial Growth in an Agent-based Model.....	30
2.6 Numerical Model and Functional Process Flow .....	32
2.6.1 Numerical Computation Scheme .....	32
2.6.2 A Computationally-efficient Method to Account for Cell-cell Interactions.....	35
2.6.3 Model Information and Process Flow .....	37
2.6.4 Investigation of the Effects of Mesh Size and Time Step on Model Predictions .....	40
<b>Chapter III: Experimental Validation of the Model</b> .....	<b>43</b>
3.1 Microfluidic Platform Utilized for Chemotaxis and QS Experiments.....	43
3.1.1 Microfluidic Device Design.....	43
3.1.2 Device Fabrication .....	44
3.1.3 Microfluidic Device Modeling .....	45
3.2 Experimental Validation of the Chemotaxis Model .....	47

3.2.1 Microfluidic Experiments and Data Analysis .....	47
3.2.2 Determination of Kinetic Parameters and Model Validation .....	50
3.3 Experimental Validation of QS Model .....	52
3.3.1 Measurement of the Effective Diffusivity of a Small Solute in Dense Populations of Motile Bacteria.....	53
3.3.2 Experimental Methods for QS Validation .....	58
3.4 Engineering a QS Response: Model Utility for Application-driven Design .....	69
3.4.1 QS Response in the Absence of a Chemical Gradient .....	69
3.4.2 QS Response in a Community of QS and QQ Bacteria.....	70
3.4.3 Designing and Modeling QS Constructs with Altered Sensitivity .....	78
<b>Chapter IV Discussion of Results and Future Work.....</b>	<b>82</b>
4.1 Discussion .....	82
4.2 Future Work .....	88
<b>References .....</b>	<b>91</b>

## List of Figures

Figure 1.1: The Flagellar Motor.....	4
Figure 1.2: Bacterial Swimming.....	6
Figure 1.3: The Chemotaxis Pathway in <i>E. coli</i> .....	7
Figure 1.4: The <i>luxIR</i> Circuit of <i>Vibrio fischeri</i> .....	10
Figure 1.5: The Relevant Physical Scale vs. Computational Time (expense) Scale for Microbial Modeling Approaches .....	12
Figure 2.1: Plots of Log-normally Distributed $\theta$ Values .....	22
Figure 2.2: Agent Movement and Phase Change in Simulations .....	23
Figure 2.3: Simulated Random-walk Motility and Chemotaxis .....	26
Figure 2.4: Plot of a Hill Function for $H = 1$ , $H = 2.5$ , and $H = 5$ .....	27
Figure 2.5: Plot of Relative Population Size vs Time for non-constant Doubling Times .....	32
Figure 2.6: Steps for Numerically Solving Equation 2.14 using the ADI Method.....	34
Figure 2.7: Diffusion Simulation Validation in the $x$ - (a) and $y$ -directions (b).....	35
Figure 2.8: Efficient Modelling of Cell-cell Collision Events.....	36
Figure 2.9: 10-minute Average of Population Density as a Function of $x$ -location (left) and the Emergent Structure of a Coarse Interactions Mesh as Demonstrated by Trajectories of 50 Agents over a 1000 s (right).....	37
Figure 2.10: Chart of Model Process Flow .....	39
Figure 2.11: The Effect of Time Step on Simulated Chemotaxis for an Optimized Chemical Gradient.....	40
Figure 2.12: The Effect of Mesh Size on Activation Time.....	41
Figure 3.1: Microfluidic Device used for Experiments .....	44
Figure 3.2: Fabrication of Microfluidic Device .....	46
Figure 3.3: COMSOL Simulations of L-aspartic Acid Diffusion in PEG-DA Device .....	47
Figure 3.4: Image Processing for Measuring Chemotaxis Metrics.....	49
Figure 3.5: Simulated and Experimental Chemotaxis Response .....	51
Figure 3.6: Schematic of the Microfluidic Device Used to Measure Effective Diffusivity in the Presence of Motile Bacteria.....	53
Figure 3.7: Image Processing and Data Analysis for Diffusivity Measurements.....	57
Figure 3.8: Results of Diffusivity Measurement Experiments .....	57
Figure 3.9: Determination of Experimental QS Activation Time.....	63
Figure 3.10: Activation Time Depends in Part on Initial Conditions .....	66
Figure 3.11: Experimental Validation of the QS Model.....	68
Figure 3.12: QS Activation in a Homogeneous Distribution of Bacteria .....	69
Figure 3.13: Experimental and Simulation Results for Mixed QQ and QS Bacterial Communities .....	72
Figure 3.14: AiiA Protein Dynamics and Enzymatic Degradation of AHL .....	75
Figure 3.15: Representative Images of QS-QQ Experiments and Simulations .....	75
Figure 3.16: Population Dynamics in 6 Simulations of the 3.0:1 Scenario for QS and QQ Strains .....	77
Figure 3.17: Relative Population Size versus Time for a Simulation of the 3.2:1 Case.....	78
Figure 3.18: Application of the Model as a Genetic Design Tool for Synthetic Biology .....	81
Figure 4.1: Activation Time as a Function of Normalized Population Growth Rate ( $dP^*/dt$ ) and RBS Strength Relative to BBa_B0034 .....	84

Figure 4.2: The Effects of Growth Rate **(a)** and Up-regulation Threshold  $Q_0$  **(b)** ..... 85

Figure 4.3: HCT-116 Tumor Spheroid Colonized with QS *Salmonella* Typhimurium VNP20009  
Expressing GFP as an Indicator of QS Activation while Constitutively Expressing RFP ..... 88

## List of Tables

Table 3.1: Parameters used in Simulations for Chemotaxis Model Validation .....	52
Table 3.2: Optimal QS Parameters .....	67
Table 3.2: Parameters Used in the AiiA Model.....	73

## Nomenclature

$\lambda_i$	reciprocal of mean run or tumble time ( $i = T$ or $i = R$ )
$\tau_i$	duration of either run or tumble
$P$	probability of phase change
$\vec{V}_b$	Bacterium velocity vector
$\Delta t$	time step
$\theta_T$	tumble angle
$r$	coefficient for Box-Muller transformation
$\theta_{T,\mu}$	mean tumble angle
$\theta_{T,\sigma}$	standard deviation of tumble angle
$\theta$	agent's present bearing
$C$	number of bound chemoreceptors
$\tau_0$	average run time in the absence of a chemical gradient
$\sigma$	chemotactic sensitivity
$C_T$	total number of chemoreceptors
$s$	local chemoeffector concentration
$K_d$	chemoeffector dissociation constant
$A_T$	AHL generation rate
$A_1$	basal AHL generation rate
$A_2$	upregulated AHL generation rate
$Q$	local AHL concentration
$H$	Hill coefficient

$Q_0$	upregulation threshold concentration
$G_i$	immature GFP
$G_m$	mature GFP
$k_{tr}$	the maximum rate of $G_i$ production
$k_{G_m}$	the rate of $G_i$ maturation
$\mu$	growth rate
$\mu_0$	initial growth rate at $t = 0$
$k_{deg}$	maximum rate of protease-mediated degradation of GFP
$K_m$	half-maximal concentration of GFP for protease-mediated degradation
$D_{AHL}$	diffusivity of AHL
$\vec{V}$	fluid velocity field
$R_d$	relative rate of AHL degradation
$Q^-$	rate of AHL degradation due to AiiA
$k_{cat}$	specific rate of enzymatic degradation of AHL by AiiA
$A$	AiiA concentration
$K_A$	concentration of AHL when AiiA-mediated degradation is half-maximal
$k_A$	constitutive rate of production of AiiA
$k_{A,deg}$	relative rate of AiiA degradation
$P^*$	population size relative to the initial population
$P(t)$	population size as a function of time
$P_0$	initial population size at $t = 0$
$\tau_g$	agent doubling time

$p_{dbl}$	probability of an agent doubling at a given point in time
$\Delta t_g$	amount of time required for population to increase by one agent
$\Delta x_c, \Delta y_c, \Delta s_c$	spacing of the interactions mesh
CMC	chemotaxis migration coefficient
$N(x)$	number of agents or bacteria at location $x$
$w$	width of the channel or simulation domain
CPC	chemotaxis partition coefficient
$D_{eff}$	effective diffusivity of fluorescein in the presence of motile bacteria
$u$	streamwise fluid velocity
$Q_{IC}$	initial concentration of AHL inside an agent
$\alpha$	scaling parameter for setting $Q_{IC}$
$\beta$	experimentally measured initial condition
$\eta_{RBS}$	scaling parameter for modeling RBSs of varying strength
$n_{luxI}$	number of copies of the <i>luxI</i> gene

## Chapter I: Introduction<sup>1</sup>

### 1.1 Motivation

Bacteria play a central role in a wide range of disciplines from microbiology to medicine to engineering. For instance, bacteria are crucial for directed bioremediation efforts, where motility and chemotaxis may be exploited to cause preferential localization at the source of a toxic compound [1]–[3]. From a biomedical standpoint, microbial population dynamics can be critical both for the development of novel therapeutics and in the study of pathogenesis, such as in the development of tumor-targeting bacteria to combat cancer or in the quorum sensing-mediated onset of cholera [4]–[6]. Bacteria can also be employed as biosensors to detect pollutants such as heavy metals and organic compounds or can even be used for drug screening [7]–[10]. Moreover, in their natural environments, bacteria live in heterogeneous, spatially-structured communities, underpinning their survival and behavior through many complex interactions that are often irreproducible in the laboratory [11], [12]. Likewise, the engineering of synthetic microbial consortia has demonstrated immense benefit over single-species systems for performing complex functions [13]. With the advent of synthetic biology, applications such as these are being advanced at an accelerating pace. As complexity increases, systems-level models are essential for both understanding and effectively designing complex systems [14]. The ability to both accurately and efficiently model population dynamics will greatly aid in our exploitation of the ways in which bacteria move, invade, synthesize, and metabolize. To date, a number of models for chemotaxis, physical interactions, gene expression, and microbial communication have been developed, but a comprehensive, experimentally-verified, and computationally-inexpensive simulation of these

---

<sup>1</sup> Portions of this chapter are from an accepted manuscript entitled “Nanoscale Bacteria-Enabled Autonomous Drug Delivery System (NanoBEADS) for Cancer Therapy” by Suh, S., Leaman, E. and Behkam, B., which will comprise a chapter in *Encyclopedia of Medical Robotics* in the volume “Micro and Nano Robotics.” SS and EL conducted the experiments, and SS, EL, and BB wrote the manuscript.

elements has not been reported. Through rigorous experimentation and validation, this need was addressed by making appropriate simplifying assumptions to produce a computationally inexpensive but robust agent-based, biologically-accurate computational model of emergent behavior in a bacterial population.

## **1.2 Background**

Bacteria are prokaryotic organisms that are among the simplest of forms of life, but nevertheless exhibit complex behavior that stems from a form of molecular cognition, representing constant monitoring and response to their physical environment [15]. They possess a variety of molecular tools for sensing a wide variety of stimuli from damaged DNA to mechanical forces to biomolecular signals and even maintaining an adaptive immune system [15]–[17]. They can exist in many morphologies and phenotypes, each best suited for the cells' native environment [18]. Many species possess some form of motility (*i.e.* the ability to translocate) and have the ability to preferentially localize in favorable locations via a taxis mechanism (*e.g.* chemotaxis in response to the gradient of a chemo-effector). Moreover, many are known to express multiple types of extracellular signals, which are used for both inter- and intra-species communication known as *quorum sensing* (QS) [19]. The physiology of prokaryotes is thus an engaging topic (see [20]).

The goal for this thesis was to develop an experimentally-validated model that captures the relevant physical phenomena involved in regulating emergent behavior in motile and chemotactic populations of flagellated bacteria in a computationally-efficient framework. Specifically, we focused on accurately predicting the amount of time required for genes controlled by a quorum sensing system to be expressed in a dynamic population and how the number density and spatial distribution of population, presence of non-quorum sensing and/or quorum quenching bacteria affect the activation time. The model's capabilities include the simulation of bacterial motility and

chemotaxis, cell-cell interactions, mass transport, and bacterial growth, all of which must be considered for accurate predictions. Further, a model for enzyme-based quorum quenching (QQ) was also developed, allowing us to use the computational framework to simulate interacting QQ and QS populations in a microbial community. A brief review of the biology relevant to this research is presented in the sections that follow.

### 1.2.1 Bacterial Motility

Motile bacteria can actively translocate through space via several mechanisms. Specifically, four modes of active motility have been well-characterized to date: swimming, swarming, gliding, and twitching [21]. Twitching motility, a form of gliding, involves small polar appendages on the cell body called type IV pili [18], [21]. By extending and retracting the 6 nm-diameter fibrillar protein complexes, bacteria are able to move across a moist surface on the order of tenths of microns per second [18], [21]. Recent work has suggested that the pili even allow the bacteria to “walk upright,” and, in the case of *Pseudomonas aeruginosa*, slingshot themselves from one location to another [22], [23]. In addition to twitching, bacteria can also perform gliding motility without pili, moving up to 10  $\mu\text{m/s}$  [21]. While a detailed understanding of the propulsion mechanism in gliding motility is still lacking, recent experiments using *Myxococcus xanthus* have shown that the rotation of an intracellular helical structure creates forces between the cell membrane and a solid surface [24], [25].

The remaining forms of active motility, swimming and swarming, both involve the use of helical flagella to propel the cells [18]. Both of these modes are employed by the model Gram-negative genera *Escherichia coli* and *Salmonella enterica*, but are used by many other types of bacteria as well. The flagellum is a rigid, polymorphic structure typically 5  $\mu\text{m}$  to 10  $\mu\text{m}$  in length and 20 nm in diameter [20]. It is driven by a supramolecular rotary motor embedded in the cell

membrane that is powered by a proton ( $H^+$ ) gradient, capable of rotating at 300 Hz and generating a torque output on the order of 1200 pN·nm [20], [26]. The flagellar filament is connected to the motor via a flexible coupling called the hook, which, in function, is not unlike a universal joint employed in mechanical systems [27]. The motor, shown in Figure 1.1, is comprised of a number of protein subunits. Together, MotA and MotB span the cytoplasmic membrane and function as a stator and as force-generating units, which are able to dynamically adapt to changes in load [28], [29]. The major features of the rotor are the MS-ring and C-ring, while the P-ring and L-ring are thought to act as bushings for the rod, a central filament which translates rotational motion from the rotor to the hook [18], [28].

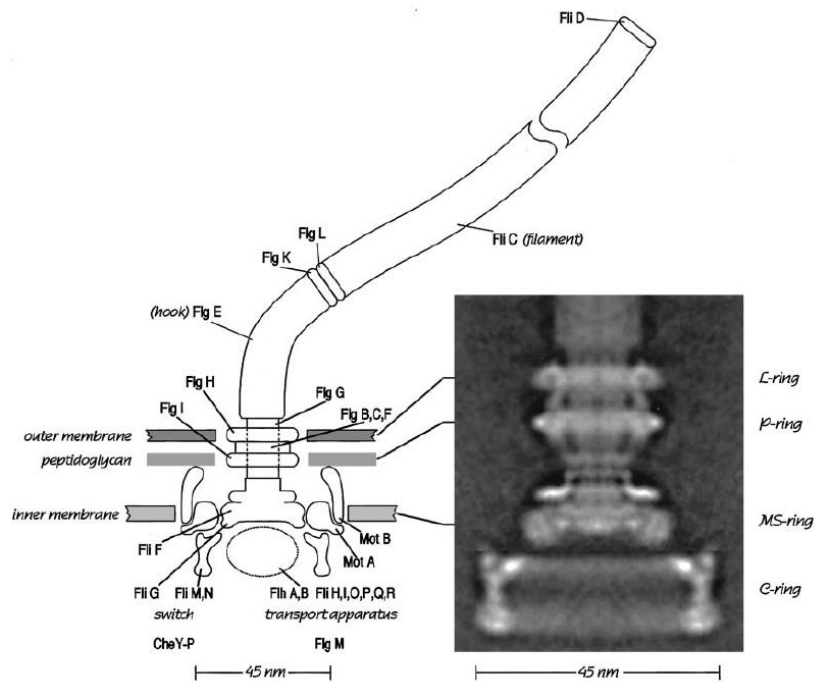


Figure 1.1: The Flagellar Motor. The major proteins and components that make up the motor and the flagellum are shown schematically on the left, and the image on the right shows a rotationally-averaged transmission electron micrograph of the motor. Reproduced from [28] with permission.

*E. coli* bacteria are peritrichously flagellated, expressing 4-7 flagella anchored to motors distributed randomly over the cell membrane when in their planktonic (*i.e.* free-swimming) state

[28]. While swimming is likely the most familiar form of flagellar motility, swarming cells also rely on flagella to provide a propulsive force. When in a swarming phenotype, the cells elongate from 2-4  $\mu\text{m}$  to up to 20  $\mu\text{m}$  in length and become hyperflagellated, expressing 2-3-fold more flagella than a planktonic cell [30], [31]. With the right water content and substrate stiffness, *E. coli* and *Salmonella* Typhimurium are able to use this mode of motility to move across a surface using the lipid-polysaccharide component of the outer membrane as a wetting agent [32]. In contrast to swimming motility, swarming cells likely do not use chemotaxis to bias their movement but require a nutrient-rich environment throughout the surface on which they move [32].

Due to their small size, swimming bacteria experience significant viscous effects (Reynolds number on the order of  $10^{-4}$ ) and their dynamics are dominated by viscous rather than inertial forces [33]. At such scales, the reciprocal-styles of movement that are intuitive in the inertial-dominated macroscopic world are ineffective, leading to the so-called scallop theorem [33]. To move, a scallop slowly opens its shell and then ejects a stream of water by quickly closing it again, leading to a transient force that propels the animal [33]. If a bacterium were to try such a strategy, it would simply oscillate in place; no net displacement could be achieved.

Contrary to swimming organisms at a larger scale, flagellated bacteria take advantage of viscous forces for propulsion. *E. coli* and *Salmonella* swim in a series of nearly-straight runs during which all of the flagella synchronously rotate in the counterclockwise direction and come together to form a coherent bundle [28]. This way, as the rotating helix propagates the waveform of the flagella, the viscous drag forces acting on the parts of the filament that are oriented at an angle with respect to the long axis of the bundle create a force in the direction opposite to wave propagation [34]. This is possible because the magnitude of the viscous drag on a thin rod moving in the normal direction with respect to its axis being greater than that of the drag when it moves

lengthwise [35]. Interrupting the runs are periods of tumbling caused by a reversal in the direction of rotation of the motors from counterclockwise to clockwise. When this occurs, the normally left-handed helices begin to morph into right-handed helices, starting from the hook and moving outwards [20]. In consequence, the unbalanced forces on the flagella act in concert with rotational diffusion to reorient the cell in a pseudo-random direction [20], [36]. Figures 1.2a and 1.2b show a peritrichously flagellated bacterium in a run phase and a tumble phase, respectively. On average, *E. coli* swim at a constant speed of 21  $\mu\text{m/s}$  for 1.00 s and tumble for 0.14 s [27].

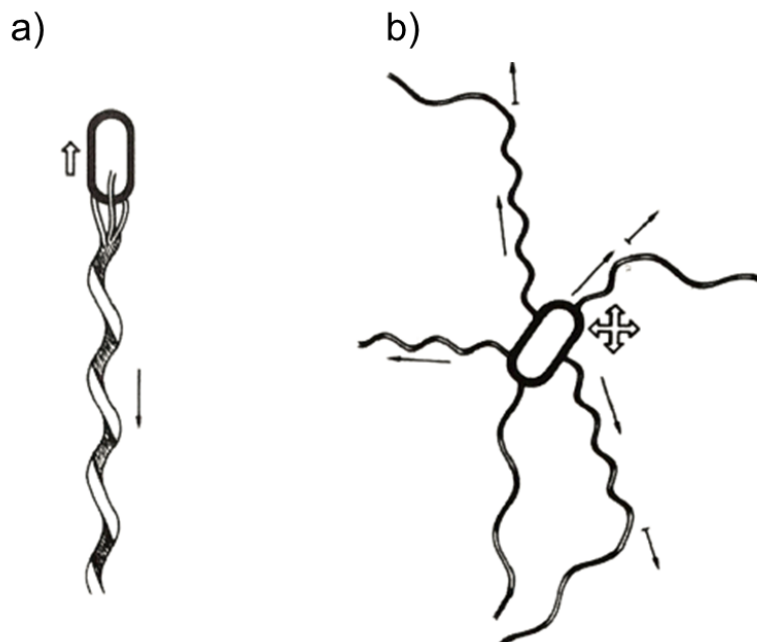


Figure 1.2: Bacterial Swimming. Schematics show a rod-shaped flagellated bacterium (*e.g. E. coli*) in a run phase (a) and a tumble phase (b). The rotation of the flagellar bundle creates a net force that propels that bacterium forward. Upon reversal of the motors, the bundle breaks apart and the bacteria are reoriented. Reproduced from [145] with permission.

### 1.2.2 Chemotaxis in *E. coli*

Bacterial chemotaxis is the result of an intracellular signaling cascade that ends in a perturbed probability of tumble, leading to a bias in the net movement of a cell. In essence, chemotaxis describes the sensing of and response to a gradient in the concentration of a variety of chemicals

(or chemoeffectors). For instance, the amino acids L-aspartic acid and serine are well-characterized chemoattractants for *E. coli*. Examples of chemorepellents include alcohols such as ethanol or hydrophobic amino acids (*e.g.* L-leucine) [37].

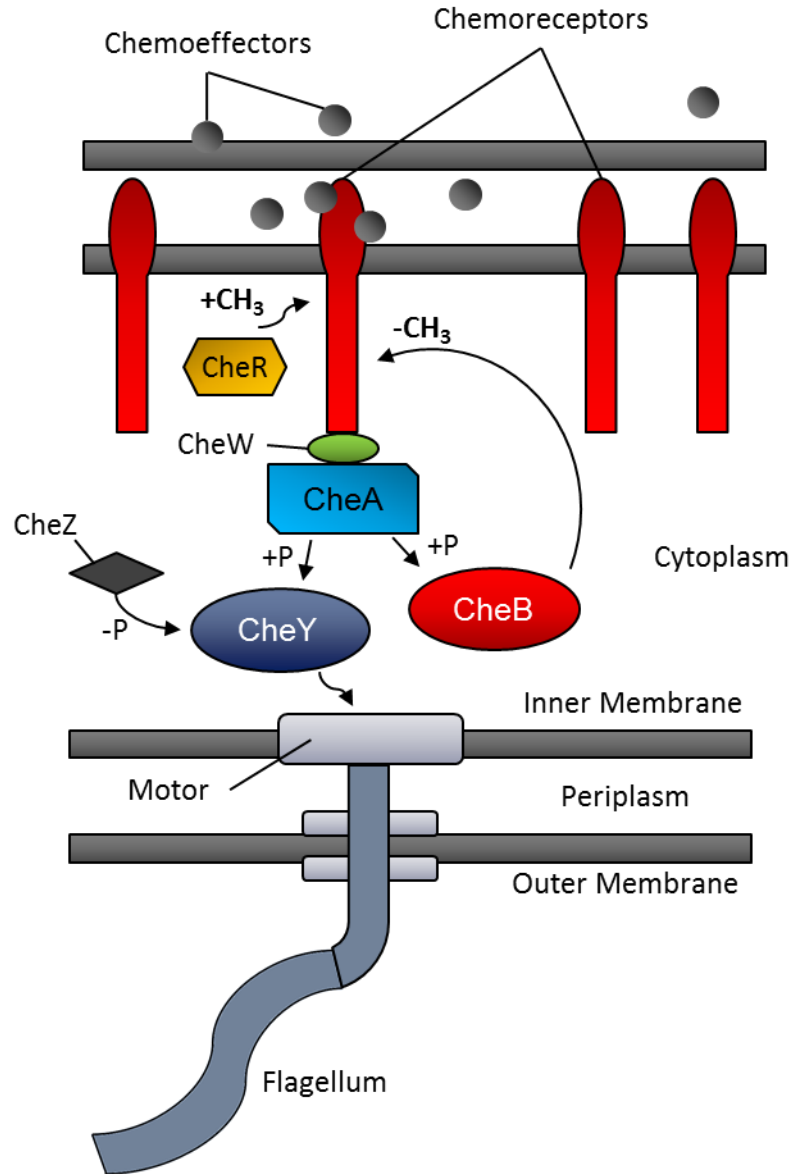


Figure 1.3: The Chemotaxis Pathway in *E. coli*. Chemoreceptors phosphorylate CheA at a rate determined by rate of chemoeffector binding and level of methylation. Changes in the rate of phosphorylation of CheY and CheB lead to changes in tumble frequency and the rate of receptor demethylation, respectively. CheZ works to “reset” CheY by removing phosphate groups.

The chemotaxis signaling cascade shown in Figure 1.3, begins with a transmembrane receptor anchored with its effector-binding domain in the periplasm. These receptors make up the methyl-accepting protein (MCP) class [18]. There are four known MCPs in *E. coli*: Tsr for a taxis response to serine and repellents, Tar for a taxis response to aspartate and repellents, Trg for taxis to ribose, glucose, and galactose, and Tap for taxis towards dipeptides [18]. When a chemoattractant freely diffuses through the outer membrane and binds with its chemoreceptor, it sets off a chain of events beginning with a modulation in the rate of autophosphorylation of the histidine kinase CheA, mediated by interactions between the chemoreceptor and a coupling factor, CheW [18], [27]. When CheA is phosphorylated, it in turn activates CheY, which then diffuses through the cytoplasm and causes the motor to reverse direction and rotate clockwise upon binding with the switch complex FliM [18], [27]. Higher concentrations of activated (phosphorylated) CheY therefore increase the frequency of tumble events. CheB, a methyl esterase with the function of removing methyl groups from the chemoreceptor, is also activated by phosphorylated CheA [18], [27]. CheR meanwhile adds methyl groups to the chemoreceptor at a steady rate [18]. The level of methylation acts as a sort of molecular memory by controlling the activity of the chemoreceptor relative to the rate of chemoeffector binding. In fact, bacteria exhibit perfect adaptation to chemoattractant signals based on this mechanism, which has been argued to function as a robust integral feedback control system [38].

The end result of the signaling cascade is a reduced tumble frequency when swimming up gradients of a chemoattractant or an increased frequency of tumble when swimming up repellent gradients [39]. Overall, this leads to a biased Brownian motion in the favorable direction.

### 1.2.3 Bacterial Quorum Sensing

Quorum sensing (QS) is the regulation of genes based on the local population density and has been shown to regulate a large number of functions in bacteria, including biofilm formation, virulence, antibiotic production, among many others [40]. This is accomplished by the secretion and detection of compounds called autoinducers (AIs), which diffuse throughout the extracellular environment [19]. Genetic processes are regulated according to the concentration of AI detected. While the amount of AI can effectively act as a measure of the cell number density in the vicinity, it has been proposed that bacteria may actually use this information to determine the mass transfer properties of their local environment in a process termed diffusion sensing [41]. Others have unified the two theories under the umbrella term “efficiency sensing,” referencing the fact that both group and individual benefits may be incurred when certain genes are expressed only in large populations where the loss of extracellular material is limited [42]. For simplicity and based on its prevalent use in recent literature, the term quorum sensing will be used throughout this thesis.

Several types of QS systems and signals have been discovered. In Gram-negative bacteria (*e.g. E. coli*), AIs are acyl-homoserine lactones (AHLs) or similar small molecules that can diffuse freely through the cell membrane [43]. In contrast, Gram-positive bacteria (*e.g. Bacillus*) secrete oligopeptides for QS [43]. AHLs are often part of a feed-forward loop, in which the enzyme that encodes an AI is upregulated, in addition to other genes, in response to the detection of that AI [43]. Many bacteria express multiple types of AIs. The proteins that receive AHL signals (LuxR and its homologues) often have a high specificity for their ligands [19]. In contrast, the gene for the enzyme that produces another type of signal, AI-2, has been detected in over 500 bacterial genomes [43], [44]. This signal is thought to facilitate interspecies communication. Interestingly,

one study even identified a potential interaction between QS in *E. coli* and the human hormone epinephrine, potentially indicating QS extends even to communication with mammalian cells [45].

QS circuits are commonly employed for practical applications using synthetic biology. Traditionally, the model circuit has been the *luxIR* system of *Vibrio fischeri*, which is natively used as a part of a symbiotic relationship with the Hawaiian Bobtail Squid [19]. This relationship is maintained when the bacteria colonize the light organ on the underside of the animal and produce light (bioluminescence) at high number densities, helping the animal hunt effectively at night [19]. In return for this service, the bacteria are well-nourished inside the squid. By regulating bioluminescence via QS, valuable energy is not wasted by producing light when it is not needed [19].

The regulatory genetic circuit of *V. fischeri*, shown in Figure 1.4, is robust and simple, making it ideal for use in recombinant hosts. The transcriptional regulator LuxR is produced at a relatively high basal rate and becomes activated upon binding with AHL [19]. Dimers of LuxR-

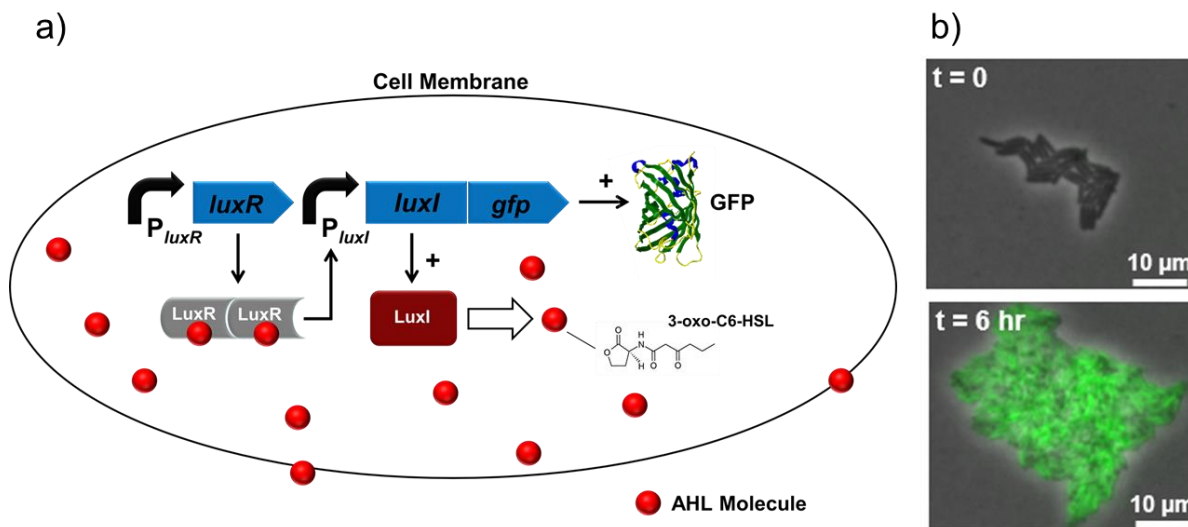


Figure 1.4: The *luxIR* Circuit of *Vibrio fischeri*. (a) A schematic of the circuit as implemented in this thesis, in which *luxCDBEG* have been replaced with *gfp*. Activated LuxR, produced at a high basal rate, promotes the transcription of genes downstream of the *luxI* promoter ( $P_{luxI}$ ). (b) A growing colony of QS *E. coli* harboring the circuit express green fluorescent protein (GFP) at high number densities.

AHL then bind to the *luxI* promoter, upregulating transcription of the *lux* operon containing *luxI* and the genes *luxCDBEG*, which together encode the luciferase, a light-producing enzyme [19]. This AHL-controlled production of *luxI* mRNA ultimately leads to the feed-forward behavior of the circuit.

The ease of bacterial genetic modification makes QS systems readily amenable to synthetic modification, allowing population-level programming of bacteria. The applications of synthetic QS-based genetic systems have been demonstrated extensively in literature [46]–[55]. Notably, You *et al.* [46] demonstrated regulated cell death as a function of population size, and [48] showed that QS could be used to induce the invasion of cancer cells. Danino *et al.* [50] paired a QS circuit with another encoding a quorum quenching enzyme to create a biological clock with tunable frequency. Most recently, Cao *et al.* [55] used the circuit in *E. coli* as a tool to demonstrate collective space-sensing for a multicellular system responding to both a diffusible signal and nutrient availability, which may explain how scale invariance is achieved during mammalian organ development.

### 1.3 Classifications of Models and a Review of the State-of-the-art

There are several primary approaches for modeling bacterial behavior. We categorized these models as being one of three types: Keller-Segel-like, agent-based at the population-scale and, and agent-based at the single-cell scale. Figure 1.5 shows the approximate computational time and physical domain scales of these modeling approaches. In this section, the formulation of and the advantages and disadvantages of these models are reviewed, and a brief review of the state-of-art in modeling bacterial behavior is presented.

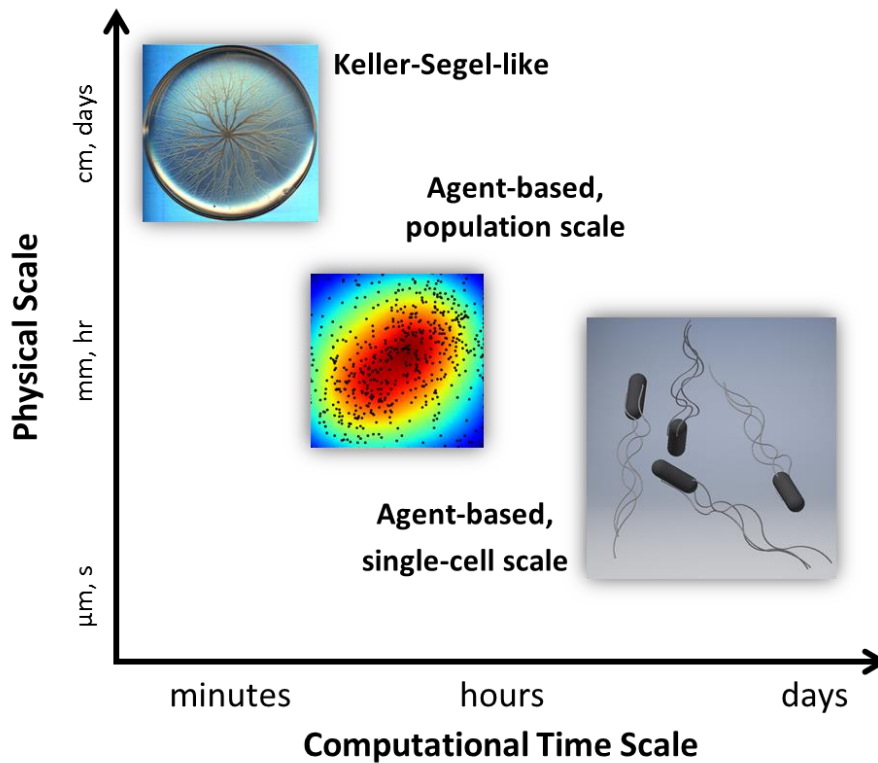


Figure 1.5: The Relevant Physical Scale vs. Computational Time (expense) Scale for Microbial Modeling Approaches

### 1.3.1 The Keller-Segel Model

Since Adler's 1966 report of traveling bands of *E. coli* up a chemoattractant concentration gradient [56], there has been considerable effort to track, quantify, and model the dynamics of motile microorganisms. Experimentally, the motile behavior of individual bacteria in response to chemical stimuli was elucidated in the early 1970s [36] [57]. A plethora of experimental studies regarding motility and chemotaxis have been published since, most of which are fundamentally based on the collective behavior of individual cells. In contrast, many models have been at the population-scale in a homogenous environment. Perhaps the best-known and most widely used population-scale model is the Keller-Segel model, which assumes that a population of chemotactic bacteria behaves mathematically according to an advection-diffusion process. The population is represented as a concentration, with the diffusive term representing the random movements due to motile behavior and the advective term capturing biased migration due to chemical gradients [58]. Though used extensively to model populations of bacteria, this model was derived from observations of population-scale transport and thus cannot be used to predict the behavior of individual cells [58], [59]. Over time, the model was refined to include physiological cellular processes. Notably, Segel [60] derived theoretical expressions to describe the time rate of change of the number of bound chemoreceptors and used them to determine the sensitivity of a bacterium's migratory response to a chemical gradient. Alt [61] later generalized the model and extended its applicability to two and three dimensions. However, it was not until 1989 when Rivero *et al.* [62] utilized an empirical relation describing a bacterium's tumbling probability as a function of chemo-effector binding that the equations could truly be used to represent the collective behavior of individual cells [63].

The primary advantage of Keller-Segel-like models is that, in general, they are relatively easy to construct and solve, and they often require fewer parameters than an agent-based model [12]. This type of model has been described as a “demonstration” model, or one which is not particularly well-suited for simulations of specific populations but rather can elucidate “general principles” [12], [64]. While this characterization could be attractive depending on the model purpose, it also highlights the main disadvantage of using a Keller-Segel-like model. That is, populations are homogeneous, and emergent behavior is built into the governing equations [12]. In contrast, emergent behavior in an agent-based model arises do to the collective behavior of individuals, which could produce a more realistic simulation [12]. Hellweger *et al.* [12] make the interesting observation that as Keller-Segel-like models (or strictly population-level models) are made more complex, by adding various population classes for example, they become more like an agent-based model.

### *1.3.2 Agent-based Modeling*

Enhanced computing power in the recent decades has made agent-based models, which describe the behavior of each individual cell, feasible. In general, this type of model is advantageous in situations where heterogeneities occur between cells, but holds the disadvantage of being more complex to build and solve than a Keller-Segel-like model [12]. Notable agent-based models at the single-cell scale, incorporating chemotaxis, chemical species transport, and hydrodynamic interactions, include one developed by Dillon *et al.* [65], which simulates the swimming dynamics of individual bacteria in detail, including flagellar rotation. More recently, another such model was developed by Hopkins and Fauci [66] which treated bacteria as point sources of gravity in a fluid field. The authors were able to simplify their simulation to two-dimensions to improve computational speed and showed that a Rayleigh-Taylor instability occurs due to cell accumulation

and consumption of a diffusing nutrient, thus affecting the movement of the cells [66]. Such a phenomenon could not have been studied *in silico* without the single-cell scale model. Nevertheless, these models are greatly detailed at the micro- and nanoscales, but extension to larger domains is prohibitive due to significant increase of computational time.

Exemplary studies using the more common class of agent-based model, one in which the expensive physics external to the cell are not calculated in detail, include the pioneering work of Kreft *et al* [67], [68], who created BacSim to simulate colony growth and biofilm formation and dynamics at the individual-cell level. Gregory *et al.* [69] presented a framework to model bacterial evolution using simple virtual objects (*e.g.* cells, proteins, etc.) based on a learning classifier system to allow for adaptability. Such a program allowed for studies that would have been long and/or difficult experimentally to be conducted quickly. A number of agent-based models that include the intracellular chemotactic signaling network have been published, including Bray *et al.*'s [70] detailed program that demonstrated how subtle details of chemotaxis may not be seen in experimental studies. Specifically, they found that cooperative interactions were needed between neighboring chemoreceptors in order to match published data on swimming behavior in various gradients. Another study resulted in the creation of RapidCell, a program that the researchers used to show how bacterial chemotaxis depends on the rate of adaption and shape of the chemical gradient [71]. Shortly thereafter, Kalinin *et al.* [72] demonstrated that using a simple logarithmic relation for the sensing of chemoattractants, first observed by Brown and Berg in 1974 [73], could be used in an agent-based model to reproduce experimental results. In recognition of the important role diverse species play in close interactions, a number of agent-based models have been employed to study biofilms. For instance, Poplawski *et al.* employed CompuCell3D, a program designed to study morphogenesis without regard to a particular species, to elucidate growth and

pattern formation in a biofilm [74]. In an effort to standardize the approach to modeling biofilms and accelerate progress, iDynoMiCS was presented in 2011, which implemented four major improvements over existing models, including the modeling of a biofilm pressure field, secretion of the extracellular polymeric substance (EPS) that makes up the biofilm matrix, the ability to simulate both heterogeneous and homogenous systems, and a consideration of the cells' metabolism in simulated growth rate [75]. Other notable studies include those conducted in Haseloff's group [76], [77] to show spatial patterns in a biofilm using an agent-based formulation. In a more behaviorally-comprehensive approach, Wei *et al.* [78] created a model capturing intracellular chemotaxis signaling and QS in a 3D diffusive environment, using it to demonstrate a hypothetical synthetic microbial network. They used their model to demonstrate how the state of genetic logic gates could be controlled by QS during taxis towards a point source. More recently, part of the same group studied the effects of QS in a diverse biofilm containing a fraction of agents that were resistant to compounds that inhibit the QS signal [79]. The authors then demonstrated how QS inhibition can affect the spatial structure of communities of QS bacteria, cheaters (non-QS bacteria that benefit from the QS activation of other bacteria in the community), and QS bacteria resistance to inhibition. Most notably, their results suggest that the most effective strategy to combat QS-mediated virulence in biofilms would involve a combination of EPS-targeting drugs and QS inhibitors. However, their results have not yet been experimentally verified.

#### **1.4 Objectives and Organization of the Thesis**

In order to make accurate predictions of the time required for QS-regulated behavior in dynamic populations of bacteria, we have developed a computational model capable of simulating bacterial motility, chemotaxis, physical interactions, growth, mass transport, and competition in a mixed QQ-QS community. All aspects of the model were experimentally verified by engineering custom

plasmids for *E. coli* and performing experiments in a well-controlled microfluidic environment. To our knowledge, no model exists which is able to accurately predict the time required for a QS-controlled genetic switch to be turned on in a spatiotemporally-dependent manner. Moreover, we have extensively validated the model's predictions of both chemotaxis and QS activation times, which is absent or minimal in most previously published modeling work. The model presented herein holds great utility for rationally designing QS networks for a wide range of applications where time and space are significant to success, including drug delivery, biosensing, and bioremediation, among others. The remainder of the thesis is organized according to the following:

**Chapter 2:** This chapter describes the development of the computational model. Specifically, all governing equations are derived and given in their final form. Their descriptions and incorporation into the computational framework are logically organized, beginning with the model of bacterial motility. Next, a mathematical descriptions of chemotaxis, QS, QQ, and growth are presented. The numerical approach to solving the model is discussed, followed by a description of the novel methods used to account for cell-cell interactions and the QS initial condition. The logical processes flow of the model is summarized, and finally, the effects of time step and mesh size are characterized.

**Chapter 3:** The third chapter details all experimental methods and the results of both experiments and simulations. The design and fabrication of the microfluidic device used for all experiments is described, as are the assumptions made in order to model the flow-free environment created inside. Next, experimental validations of virtually all aspects of the model are presented. First, the chemotaxis model alone was fit to the experimental data comprising linear chemoattractant gradients spanning three orders of magnitude. Next, the results of experiments to quantify the effects of advection on mass transport inside the device are presented along with detailed

descriptions of data analysis. Validation and fitting of the QS model based on experiments with QS bacteria alone in the presence of a chemoattractant gradient is detailed. The fitted model is then used to make predictions for several alternative QS scenarios, including in the absence of a chemoattractant gradient, in a microbial community with QQ bacteria, and in populations harboring rationally-tuned genetic circuits. In each case, experimental results are presented alongside simulation data.

**Chapter 4:** The concluding chapter outlines the original contributions of this work to the field of biological systems modeling, limitations of the model are discussed, and predictions are made regarding QS in several hypothetical cases. A set of pilot experiments and their results demonstrating biomedical application of rationally designed QS bacteria are described. Finally, future work stemming from this thesis is outlined.

## Chapter II: Computational Framework and Agent-based Modeling

There are several features that are fundamental to building an accurate model of bacterial migration and communication. These include a simulation of the random walk that characterizes basic flagellar motility, the proper adjustment of this motility model to account for biased migration in the presence of chemical gradients, and the solution to a set differential equations describing the production, sensing, degradation, and transport of chemical signals. The following sections describe the development of each of these features, which were implemented in the computational model as modules capable of functioning independently of one another. Specifically, the model is capable of simulating motility, chemotaxis, QS, growth, mass transport, and accounts for physical cell-cell interactions. Additionally, a model of QQ was developed and included in order to simulate distinct, competing populations in a microbial community.

### 2.1 Modeling Basic Bacterial Motility: Run-and-tumble in the Absence of a Chemo-effector

Flagellated bacteria such as *E. coli* and *S. Typhimurium* migrate according to a random walk in a so-called “run-and-tumble” fashion when in their planktonic state (*i.e.* freely-swimming). A run is a nearly-linear translocation in space during which the flagellar filaments form a coherent helical bundle with which a cell propels itself forward at a constant rate. The run phase is interspersed with periods of tumbling, during which the bacterium is reoriented due to Brownian motion. The probability  $P(\tau)$  of such an event occurring increases with time during the run phase according to a Poisson process,

$$P(\tau) = \int_0^{\tau} \lambda_i e^{-\lambda_i t} dt, \quad 2.1$$

here  $\lambda_i^{-1}$  is the mean run or tumble duration, and  $\tau$  is the duration of the particular event [80]. The actual frequency of tumble occurrences depends on a signaling cascade stemming from the

temporal binding and dissociation of external chemical signals, discussed in Section 1.2.2. Thus, in the absence of such signals, a large collection of run times resembles an exponential distribution [27]. For a typical *E. coli* bacterium, the average run duration is about 1 s, while the average tumble duration is about 0.1 s, also distributed exponentially [27].

The stochastic nature of cell motility was captured in the model by randomly sampling phase durations from an exponential distribution. At the start of a simulation, a predetermined number of agents (representing bacteria) were initially placed at random locations inside the computational domain. Each agent was initially assigned either a run timer or a tumble timer. Specifically, the value of each was chosen by solving Equation 2.1 for  $\tau$  and setting  $P(\tau)$  equal to a number between 0 and 1, randomly and uniformly chosen using the L'Ecuyer Algorithm with Bays-Durham shuffle [81]. Noting that the distributions of  $1 - P$  and  $P$  are equivalent,

$$\tau = -\lambda_i^{-1} \ln(P). \quad 2.2$$

Each agent in the run phase moved linearly through continuous space in steps of  $V_b \Delta t$ , where  $V_b$  is the speed of the agent and  $\Delta t$  is the time step. The average speed of an *E. coli* cell is about 21  $\mu\text{m/s}$ , while its diffusion coefficient is on the order of 0.2  $\mu\text{m}^2/\text{s}$  [27], [82]. Over the length of a 1 s run, the deviation from a straight path can be estimated as  $\langle x^2 \rangle = \sqrt{2Dt} \approx 0.6 \mu\text{m}$ . Lateral movement due to diffusion was thus considered negligible. Cells in the tumble phase were held stationary in space for the duration of their timer. Whenever the timer of an agent expired, that individual switched phase and was assigned a new timer during the next time step.

In addition to run and tumble durations, accurate modeling of changes in direction from one run to the next is critical for recapitulation of experimental results. This change in direction was defined as the tumble angle  $\theta_T$  (see Figure 2.2) and was also modeled as a stochastic process. It was noted that a log-normal distribution produces a qualitatively good match of experimental

data published in studies of bacterial motility and tracking (namely [36], [83]) and is also known to be common in natural processes [84]. A log-normal distribution of tumble angles was created by first calculating a uniformly distributed coefficient using the Box-Muller transformation,

$$r = \sqrt{-2\ln(x_1)} \cos(2\pi x_2), \quad 2.3$$

where  $x_1$  and  $x_2$  are random, uniformly distributed numbers between 0 and 1 [81]. A tumble angle with a mean of  $\theta_{T,\mu}$  and standard deviation of  $\theta_{T,\sigma}$  following a log-normal distribution was then calculated as

$$\theta_T = \exp(Br + A) \quad 2.4$$

where

$$A = \ln\left(\frac{\theta_{T,\mu}^2}{\sqrt{\theta_{T,\sigma}^2 + \theta_{T,\mu}^2}}\right) \text{ and } B = \sqrt{\ln\left(1 + \frac{\theta_{T,\sigma}^2}{\theta_{T,\mu}^2}\right)}. \quad 2.5$$

The natural logarithm of the resulting selection of  $\theta_T$  values is normally distributed, that is  $\ln(\theta_T) \sim \mathcal{N}(\theta_{T,\mu}, \theta_{T,\sigma}^2)$ . Figure 2.1 shows the relative distribution of  $\theta_T$  from a 9-minute simulation of 50 agents and a published experimental distribution [36].

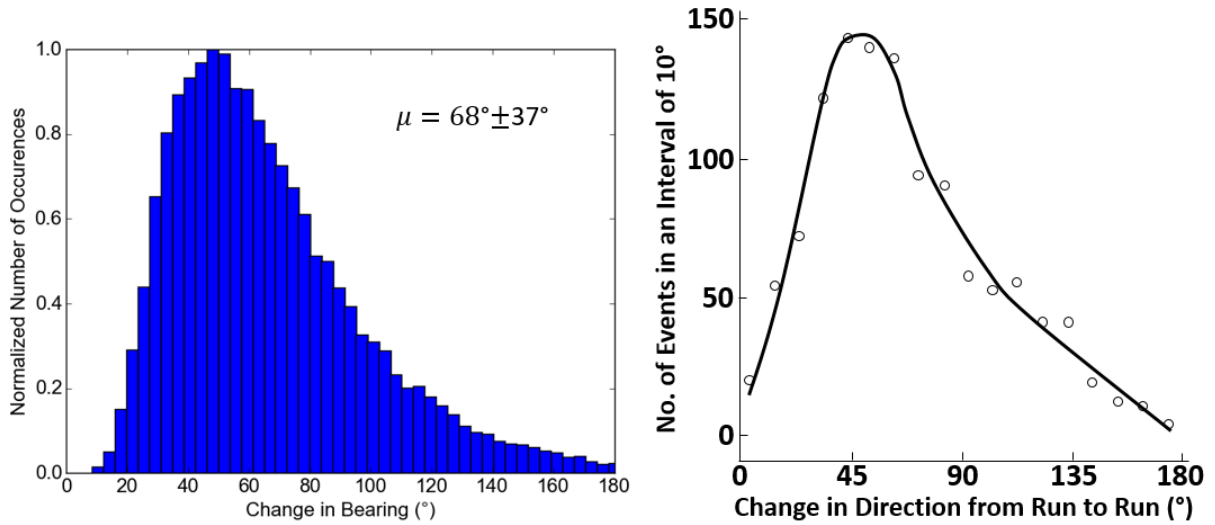


Figure 2.1: Plots of Log-normally Distributed  $\theta$  Values Sampled During a 9-minute Simulation (left) and the Experimental Data Recorded by Berg and Brown [36] (right)

Figure 2.2 shows how phase changes occur for agents in the simulation. An agent runs at a speed of  $|V_b|$  oriented with an orientation defined with respect to the  $y$ -axis. When the run timer reaches zero, a tumble angle is sampled and added to the agent's previous bearing while the agent is held stationary in space for its tumble duration. Once this tumble timer expires, the agent moves forward at the same previous swimming speed but in a new direction.

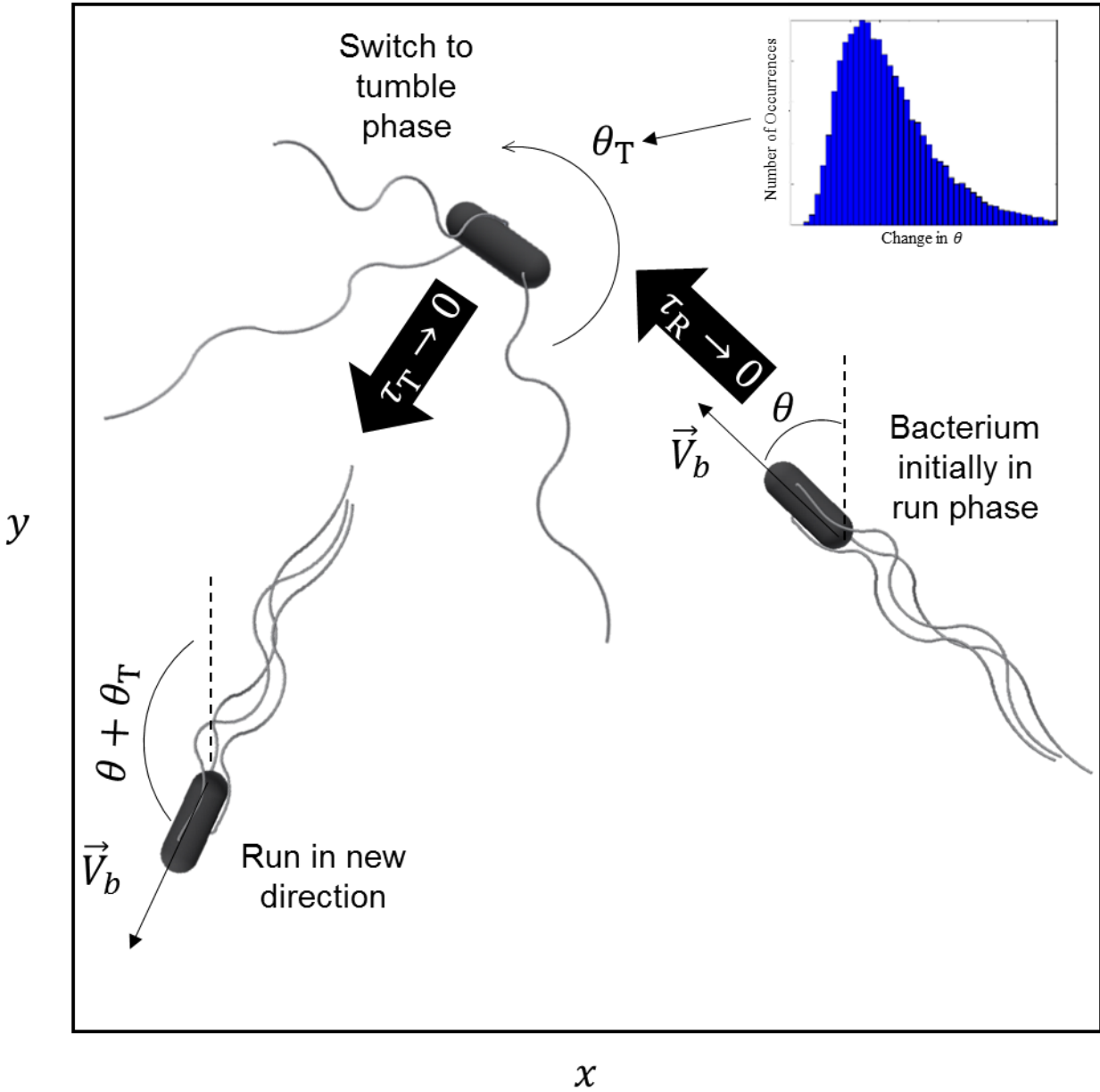


Figure 2.2: Agent Movement and Phase Change in Simulations

## 2.2 Modeling Bacterial Chemotaxis

Chemotaxis is a critical process that helps bacteria localize in chemically-favorable environments. During chemotaxis, the mean run duration  $\lambda_{\text{R}}^{-1}$  is perturbed by the binding and dissociating of chemical signals to a bacterium's chemoreceptors. These signals are typically chemical compounds that the bacterium is either attracted to or repelled by (*i.e.* chemoattractants and chemorepellents, respectively). A molecular memory mechanism allows the cell to detect concentration gradients. When moving towards the source of a chemoattractant, L-aspartate for instance, the tumbling frequency is reduced, thereby extending the length of the run up the chemical gradient. In analogous fashion, the detection of a toxin, such as hydrogen peroxide, in increasing concentration raises the probability of a tumble event. In this way, bacterial motility can be biased in a favorable direction.

Brown and Berg [36], [73] observed that the natural logarithm of the mean run durations of *E.coli* varied linearly as a function of the temporal derivative of the number of bound chemoreceptors. Rivero *et al.* [62] later suggested that bacteria are indifferent to temporal concentration changes versus those that are due to the cells' movement through spatial gradients. The run duration therefore depends on both the temporal and spatial derivative of chemo-effector concentrations. This rate of change is represented by the material derivative,

$$\frac{DC^{\pm}}{Dt} = \frac{\partial C}{\partial t} \pm \vec{V}_b \cdot \nabla C, \quad 2.6$$

where  $C$  is the number of bound receptors [62]. The mean run time can then be modeled as [62], [63]

$$\tau(\mathbf{x}, t) = \tau_0 \exp\left(\sigma \frac{DC^{\pm}}{Dt}\right), \quad 2.7$$

where  $\mathbf{x} = x, y, z$ ,  $\tau_0$  is the average run duration in a chemically isotropic environment, and  $\sigma$  is the chemotactic sensitivity. Rivero *et. al.* [62] maintained the assumption by Berg and Brown [73] of Michaelis-Menten-like receptor-ligand binding kinetics,

$$C(s) = \frac{C_T s}{K_d + s} \quad 2.8$$

where  $C_T$  is the total number of chemoreceptors for a bacterium,  $s = s(\mathbf{x}, t)$  is the local chemoeffector concentration, and  $K_d$  is the dissociation constant for the binding of a chemoeffector to a receptor. The mean run time can be determined from Equation 2.7 as

$$\tau^\pm(x) = \tau_0 \exp \left[ \sigma \frac{C_T K_d}{(K_d + s)^2} \left( \frac{\partial s}{\partial t} \pm \vec{V}_b \cdot \nabla s \right) \right]. \quad 2.9$$

For bacteria swimming up a chemoattractant gradient (increasing concentration)  $\tau = \tau^+$ , while  $\tau = \tau^-$  for movement away from the chemoattractant source (decreasing concentration). This behavior is reversed in chemorepellent gradients, such that  $\tau^+$  and  $\tau^-$  always indicated movement in a favorable or unfavorable direction, respectively.

Chemotactic behavior was implemented in the model by defining a chemical concentration field in continuous space using either COMSOL simulation results (see Section 3.1.1) or an analytical solution for diffusion in space and time (see Section 4.1). The mean run time was calculated for each agent based upon the change in concentration between successive runs. Equation 2.2 was then used to calculate a stochastic run duration, taking  $\lambda_R^{-1} = \tau^\pm$ . Figure 2.3 shows the trajectories of three individual agents over a 100 s simulation period. No chemoeffector gradient was modeled for the case shown in the Figure 2.3a, while a chemoattractant diffusing from the center of the field was used for the case shown in Figure 2.3b.

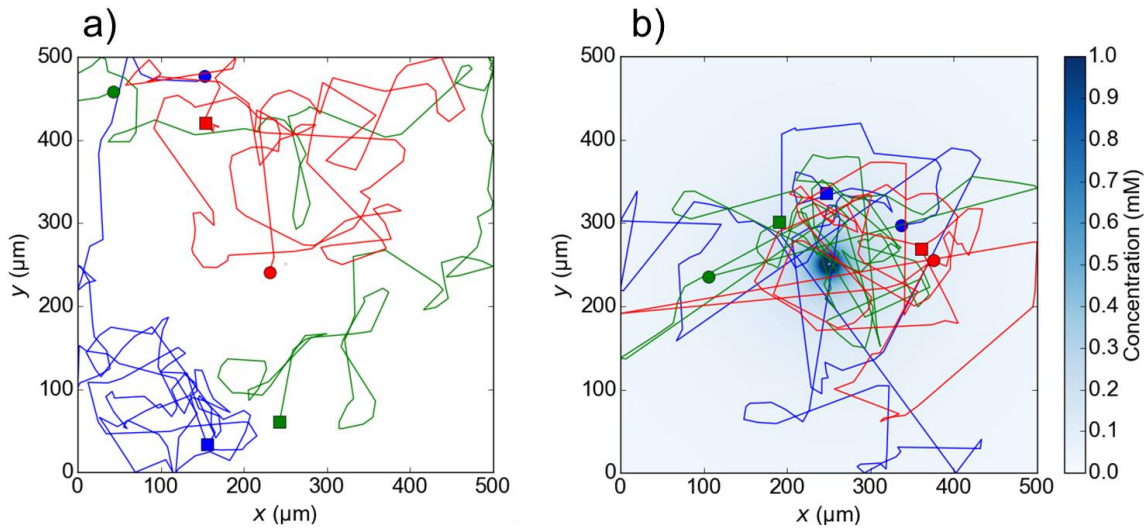


Figure 2.3: Simulated Random-walk Motility and Chemotaxis. The trajectories of 3 agents (each represented by a differently-colored trace) during a 100 s simulation period in the (a) absence and (b) presence of a chemoattractant source. Circular and square markers denote the starting and ending positions of each trace, respectively. Figure (b) was generated using the analytical solution derived by Futrelle and Berg [136] for the diffusion of a chemoattractant from a capillary tube.

### 2.3 Modeling Quorum Sensing

Many species of bacteria utilize QS as a mechanism for intercellular communication via the secretion of small signaling molecules, whereby it is generally assumed that the local population density is inferred from the sensed concentration of the signal [41], [85]. The *luxIR* system of *Vibrio fischeri* is a model QS system and is often employed in synthetic genetic constructs to program bacterial behavior [40], [46]–[52], [86], [87]. This simple and robust genetic machinery was therefore chosen for this thesis and used to control the expression of green fluorescent protein (GFP), (Figure 1.4). In this system, an acyl-homoserine lactone (AHL) signaling compound (3-oxohexanoyl-homoserine lactone) is produced by the AHL synthase LuxI, which is expressed at a low, constitutive rate in the absence of AHL. As the concentration of AHL increases, its rate of binding with the transcriptional regulator LuxR, which is produced at a high constitutive rate, increases. The LuxR-AHL complex binds to the *luxI* promoter region of the DNA and sharply

upregulates the transcription of *luxI* thus creating a positive feedback loop with AHL. This process can be captured using a Hill function,

$$A_t = A_1 + A_2 \frac{Q^H}{Q^H + Q_0^H}, \quad 2.10$$

where  $A_1$  and  $A_2$  are the constitutive and upregulated rates of AHL generation, respectively,  $Q = Q(\mathbf{x}, t)$  is the local concentration of AHL,  $Q_0$  is the concentration at which production is considered to be “upregulated,” and  $H$  is the Hill constant [88], [89]. Figure 2.4 shows the characteristic switch-like behavior of a Hill function with respect to the Hill coefficient.

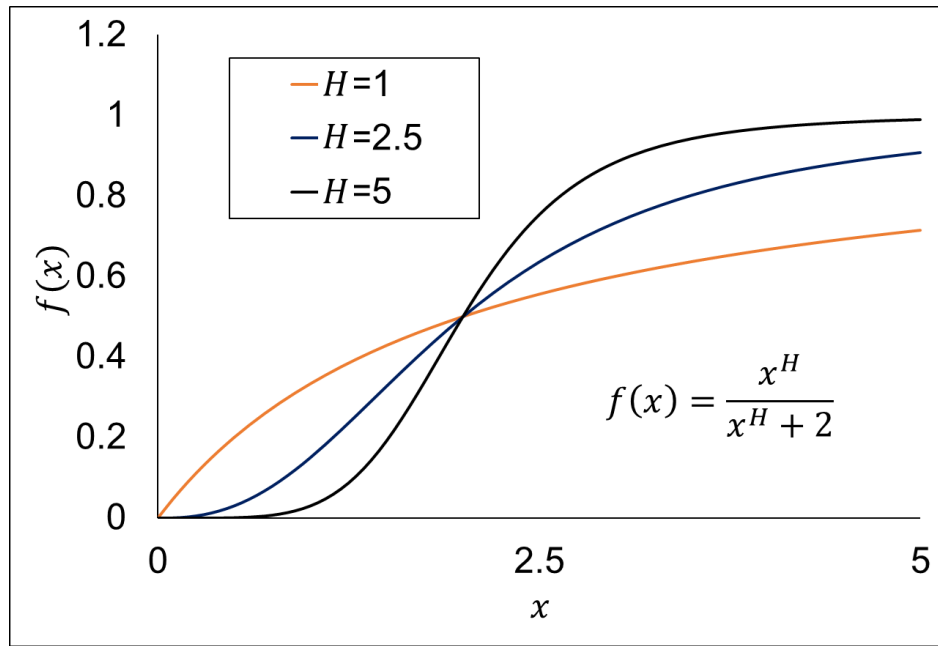


Figure 2.4: Plot of a Hill Function for  $H = 1$ ,  $H = 2.5$ , and  $H = 5$

In nature, QS is known to regulate the expression of a variety of genes in bacteria, but can be utilized in practice for the production of pharmaceuticals or therapeutic proteins, for instance. The function of the QS circuit can be studied using a fluorescent protein as a visual reporter. To this end, the gene for GFPmut3b, an engineered derivative of wild-type GFP for improved fluorescent properties, was placed downstream of the *luxI* promoter in experimental studies [90].

In order to accurately compare modeled and experimental results, the kinetics of immature protein ( $G_i$ ) translation and maturation into its fluorescent conformation  $G_m$  were modeled, following the approach of Leveau and Lindow [91], as the coupled system of ordinary differential equations (ODEs),

$$\frac{dG_i}{dt} = k_{tr} \frac{Q^H}{Q^H + Q_0^H} - k_{G_m} G_i - \mu G_i - k_{deg} \frac{G_i}{G_i + G_m + K_m} \quad 2.11$$

and

$$\frac{dG_m}{dt} = k_{G_m} G_i - \mu G_m - k_{deg} \frac{G_m}{G_i + G_m + K_m}, \quad 2.12$$

where  $k_{tr}$  is the maximum rate of production of  $G_i$ ,  $k_{G_m}$  is the rate of GFP maturation,  $\mu$  is time-dependent growth rate (representing dilution due to cell division),  $k_{deg}$  is the maximum rate of protease-mediated protein degradation,  $K_m$  is the concentration of GFP (assumed equivalent for both  $G_i$  and  $G_m$ ) at which the rate of degradation is half its maximum rate, and  $k_{G_m}$  is the rate of maturation of  $G_i$  into  $G_m$ .

The main goal of the model developed in this thesis was to predict the QS “activation” time, which was based upon the expression of GFP. Since *gfpmut3b* was promoted by the *luxI* promoter, the rate of GFP expression was assumed to be negligible in the absence of AHL. Therefore, it was also assumed that the metabolic load of GFP production had no effect on AHL synthesis prior to activation. This allowed Equations 2.11 and 2.12 to be solved independent of the main simulation using the `odeint` solver of the `scipy.integrate` module, part of the open-source scientific computing library SciPy (version 0.18.0).

In nature, AHL freely diffuses through the cell membrane [92]. Its transport through the environment and degradation over time is governed by

$$\frac{\partial Q}{\partial t} = \nabla \cdot (D_{\text{AHL}} \nabla Q) - \nabla \cdot (\vec{V} Q) - R_d Q \quad 2.13$$

where  $D_{\text{AHL}}$  is the diffusivity of AHL,  $\vec{V}$  is the local fluid velocity field, and  $R_d$  is the relative rate of AHL degradation. Numerically solving Equation 2.13 is a computationally-intensive task, primarily due to the need to solve for the flow field  $\vec{V}$ . One of the desired features of the model developed in this work was scalability and a relatively low computational expense. Therefore, the relative importance of advection to diffusion was analyzed in order to determine its importance as a mechanism of AHL transport. Over the average length of a bacterium run  $L_c$  (assuming  $\tau \sim 1$  s,  $V_b \sim 20 \mu\text{m/s}$ , and  $D_{\text{AHL}} = 490 \mu\text{m}^2/\text{s}$ ), the Péclet Number  $\text{Pe} = \frac{L_c V_b}{D_{\text{AHL}}}$  is on the order of 1, suggesting that the advection of AHL could be significant relative to diffusion. However, this would represent an “overestimated scenario” for advection, since the flow field around a swimming bacteria decays with the square of distance from the center of the cell [93]. Nevertheless, the contribution of advection to the transport of micron-sized particles (approximately  $1 \mu\text{m}$  to  $10 \mu\text{m}$ ) in bacterial suspensions, even at relatively dilute populations, has been well documented [94]–[99]. In order to determine whether or not swimming bacteria affect the transport of small molecules such as AHL (molecular weight, MW of 213 Da), a series of microfluidic experiments were performed in which the effective diffusivity of fluorescein (MW of 332 Da) was measured in the presence of highly motile *E. coli* at concentrations ranging from  $5 \times 10^8$  CFU/ml to  $1 \times 10^{10}$  CFU/ml (detailed in Section 3.3.1). In all cases, the measured diffusivity was not significantly different than the diffusivity in the absence of bacteria, thus it was assumed that the advection term  $\nabla \cdot (\vec{V} Q)$  could be neglected. In this two-dimensional model, Equation 2.13 simplifies to

$$\frac{\partial Q}{\partial t} = D_{\text{AHL}} \left( \frac{\partial^2 Q}{\partial x^2} + \frac{\partial^2 Q}{\partial y^2} \right) - R_d Q. \quad 2.14$$

## 2.4 Modeling Quorum Quenching

In nature, some bacteria are capable of quorum quenching (QQ) by degrading the autoinducers (AIs) of other microbes. One mechanism for QQ is the hydrolyzing activity of an AHL inactivation enzyme, AiiA [100]. This enzyme has been discovered in a number of *Bacillus* species and is commonly employed as a tool for programmed behavior in synthetic constructs [101]. In addition to simulating AHL-producing agents, the capability to model a distinct population of QQ agents was also included in the model. The only difference between these agents and QS agents was that instead of generating AHL molecules, they removed local AHL at a rate determined from:

$$Q^- = k_{\text{cat}} A \frac{Q}{K_A + Q}, \quad 2.15$$

where  $k_{\text{cat}}$  is the specific activity of the enzyme,  $A$  is the concentration of AiiA, and  $K_A$  is the concentration of  $Q$  at which the rate of degradation is half of its maximum value. AiiA is not secreted but remains within the cell at all times. The production, accumulation, and degradation of AiiA inside each QQ agent was modeled as

$$\frac{dA}{dt} = k_A - \mu A - k_{A,\text{deg}} A, \quad 2.16$$

where  $k_A$  is the constitutive rate of AiiA expression,  $\mu$  is the growth rate, and  $k_{A,\text{deg}}$  is the relative rate of AiiA degradation.

## 2.5 Modeling Bacterial Growth in an Agent-based Model

Another critical component of a population-scale model of bacteria is the inclusion of a growth model to facilitate the multiplication of agents over time. In this model, growth was included by defining a function  $P^*(t) = P(t)/P_0$  giving the population size relative to the initial population at any point in time. Thus, for bacteria growing a constant rate with doubling time  $\tau_g$ ,  $P^*(t) = 2^{t/\tau_g}$ . This formulation was chosen to simplify experimental validation, as it was found that the

relative population size increased linearly with time (meaning that doubling time increased significantly over the course of experiments). At each time step and for each agent, the decision whether the agent should divide or not was made by calculating the probability of division per agent,

$$p_{\text{dbl}} = \frac{\Delta t \Delta P}{\Delta t_g P(t)} = \frac{\Delta t P_0 [P^*(t) - P^*(t - \Delta t_g)]}{\Delta t_g P(t)}, \quad 2.16$$

where  $\Delta t$  is the simulation time step, and  $\Delta t_g$  is the time required for the population to increase by one agent according to  $P(t)$ .

In experiments, growth is usually measured at the population level. An important note to make is that differences between the population scale and individual scale must be reconciled when comparing experimental data to an agent-based model. In the context of growth, assigning individual agents a doubling time from experimental measurements will result in error if the doubling time is not constant over time. That is, population-level measurements provide the population-average doubling time (as a function of time), as opposed to the doubling time of only the agents that divided. To demonstrate this, consider the case of a doubling time defined by  $\tau_{\text{dbl}}(t) = \alpha t + \tau_{\text{dbl},0}$ . At  $t = 0$ , each agent will be assigned an initial doubling time from 0 to  $\tau_{\text{dbl},0}$  (to account for heterogeneity in the cell cycle). No agent in the population will take longer than  $\tau_{\text{dbl},0}$  to replicate from the simulation start, though the doubling time for the population changes continuously over the interval  $t \in [0, \tau_{\text{dbl},0}]$ . The population average doubling time integrated over this interval therefore cannot be greater than  $\tau_{\text{dbl},0}$ , inevitably resulting in error for  $\alpha > 0$ . This problem will continue to propagate throughout the simulation as new doubling times are set according to  $\tau_{\text{dbl}}(t)$ . For the case of increasing  $\tau_{\text{dbl}}(t)$ , the simulated population will grow

too rapidly, while it will grow too slowly if  $\tau_{dbl}(t)$  is decreasing in time. This result is demonstrated in Figure 2.5.

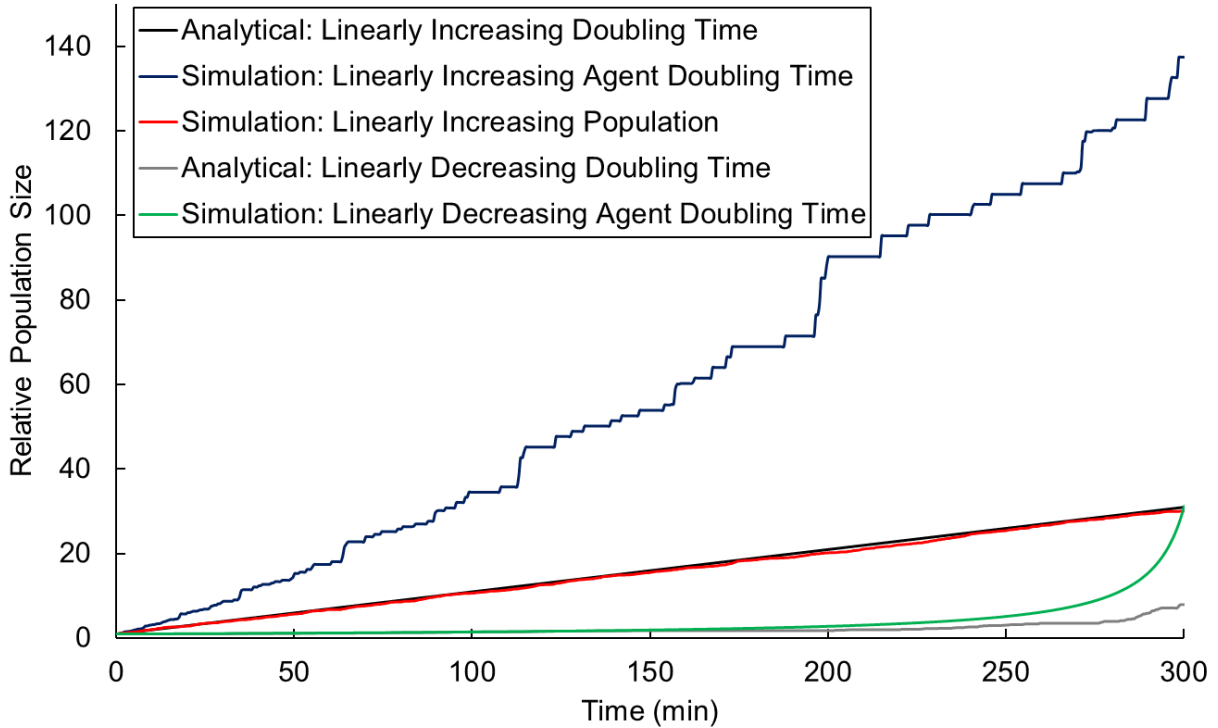


Figure 2.5: Plot of Relative Population Size vs Time for non-constant Doubling Times: Agent Growth Determined by Doubling Time or Doubling Probability. Discrete doubling times were sampled and used to set “division timers” for simulations with increasing or decreasing agent doubling times, while the continuous probability-based method described above was used for the simulation of a linearly increasing population.

## 2.6 Numerical Model and Functional Process Flow

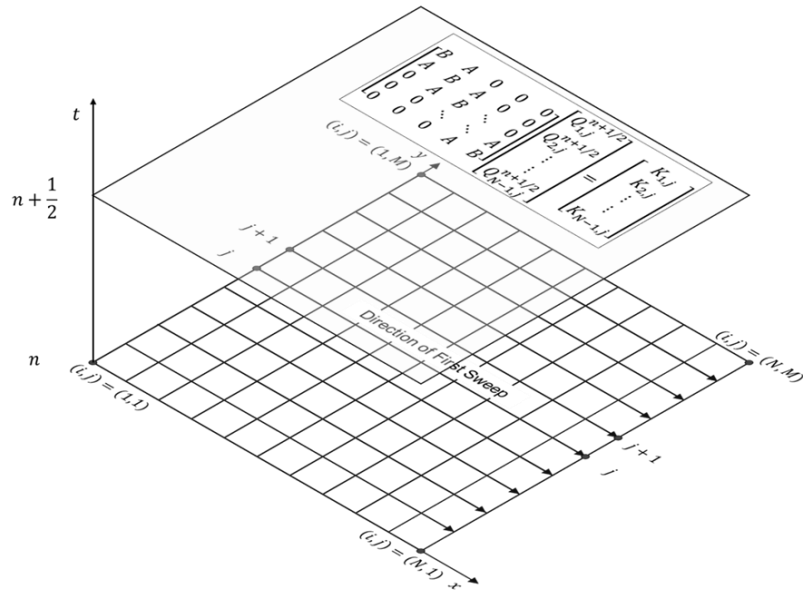
The following sections describe the numerical techniques used to solve governing differential equations and the process flow for determining the behavior of each agent. Finally, the effects of mesh size and time step on simulation results are analyzed.

### 2.6.1 Numerical Computation Scheme

The partial differential equation (PDE) in Equation 2.14 was solved using the alternating difference implicit (ADI) technique [102]. This technique holds particular advantage over more

traditional methods such a Crank-Nicolson scheme for a PDE that is unsteady in time and involves multidimensional space, because it allows the finite difference equations to reduce to tridiagonal matrices that can be solved using Thomas' algorithm [102]. This is achieved by using a two-step process to solve for values of  $Q(t + \Delta t)$  by separating the spatial derivatives and implicitly solving only one direction at a time over a half-time step. Mathematical details are given by Anderson [102]. Figure 2.6 shows conceptually how the ADI method is implemented. For stability of this method, the time step must satisfy  $\Delta t \leq (\Delta s)^2 / 2D_{\text{AHL}}$ , where  $\Delta s = \Delta x = \Delta y$ . In practice, a smaller time step was used in order to provide a closer approximation of continuous AHL contribution as the agents moved through space.

## Step 1: Sweep $x$ -direction



## Step 2: Sweep $y$ -direction

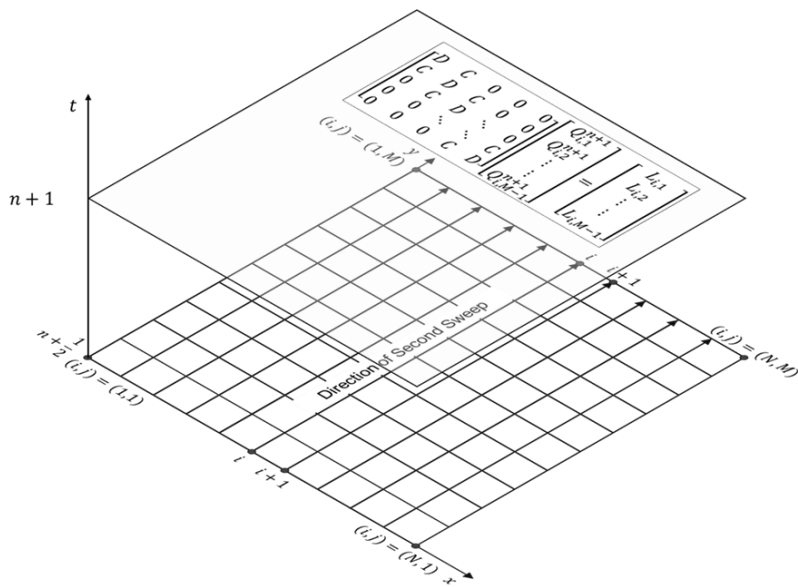


Figure 2.6: Steps for Numerically Solving Equation 2.14 using the ADI Method (figure adapted from [102]). First, the  $x$ -direction is swept at  $t = t^n$  to calculate the values of  $K$ , which are used to solve a tridiagonal matrix system giving the concentrations at  $t^{n+1/2}$ . Next, the  $y$ -direction is swept at  $t^{n+1/2}$  to calculate  $L$ , which is finally used to solve for concentrations at  $t^{n+1}$ .

The code and numerical model were verified by comparing the result of simulated one-dimensional, semi-infinite diffusion to the analytical solution. That is,

$$C^*(x, t) = \operatorname{erfc}\left(\frac{x}{2\sqrt{Dt}}\right) \quad 2.17$$

where  $C^*$  is the concentration field normalized to a non-depleting source with concentration  $C_0$ ,  $x$  is distance from the source, and  $D$  is the diffusion coefficient. Figure 2.7a shows a comparison of the simulated and analytical results for  $C_0$  located at  $x = 350 \mu\text{m}$ . The code was analogously validated in the vertical ( $y$ -) direction by placing  $C_0$  at  $y = 350 \mu\text{m}$  (Figure 2.7b). The diffusivity  $D$  was  $10 \mu\text{m}^2/\text{s}$  in both cases.

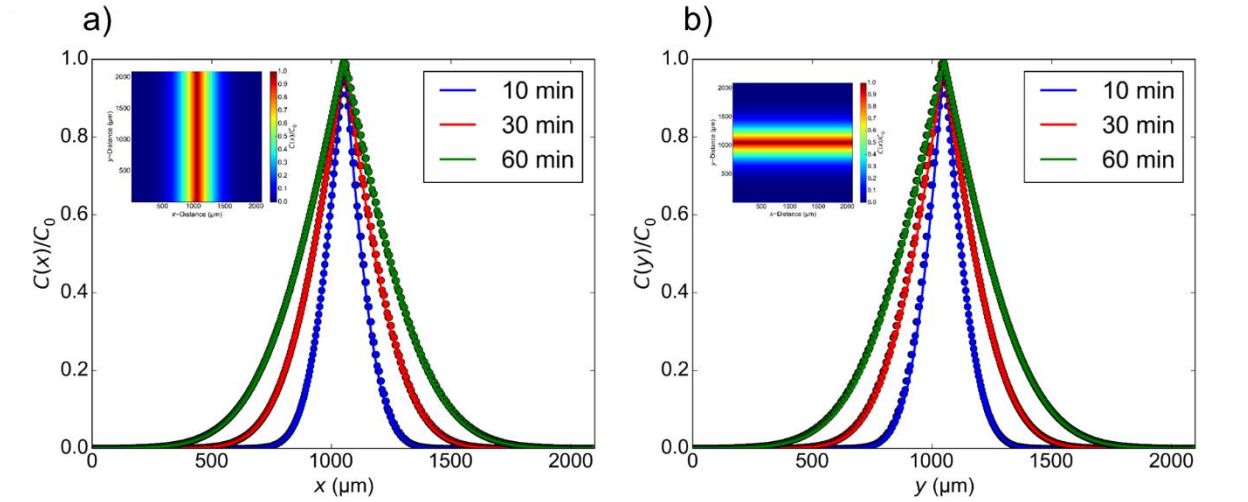


Figure 2.7: Diffusion Simulation Validation in the  $x$ - (a) and  $y$ -directions (b). Data points indicate simulation results and the smooth line indicates analytical results. The colors of correspond to the time values specified in the legend. The inset in each subplot shows a contour plot of the simulated concentration field after 60 min.

### 2.6.2 A Computationally-efficient Method to Account for Cell-cell Interactions

In continuous space, checking for collisions between agents becomes a computationally expensive process as the area around each agent (which is modeled as an infinitesimal point in space) within a finite distance must be checked at each time step to see if any other agent is within its excluded volume. In order to maintain a relatively short time requirement for solving the model, a discretized approach was developed that still allows agents to move in continuous space. This was accomplished by assuming that an average minimum distance exists between cell centers, termed

the interaction distance. This distance was used to define the internodal spacing,  $\Delta s_c$  in an “interactions mesh” on which approximate agent locations were recorded. This technique helped to maintain computational efficiency by allowing the number of agents closest to each node to be recorded in one efficient loop at each time step. If necessary, positions were then adjusted accordingly at the following time step. Specifically, if the node nearest to agent  $i$  at  $t^n$ , or if any one of the four nodes neighboring this node, was occupied at time  $t^{n-1}$ , then that agent was “snapped” to the nearest node that was unoccupied at  $t^{n-1}$ . Additionally, agents that were moved due a collision event were rotated in a random direction by a mean of  $83.6^\circ$  (sampled from a uniform distribution) according to experimental measurements of bacterial angle change before and after a cell-cell collision ( $n = 90$ ). This process is shown graphically in Figure 2.8. It was assumed that, for a small enough time step  $\Delta t$ , inherent errors in this method were negligible. Errors in space were also assumed negligible in the overall emergent behavior of the population

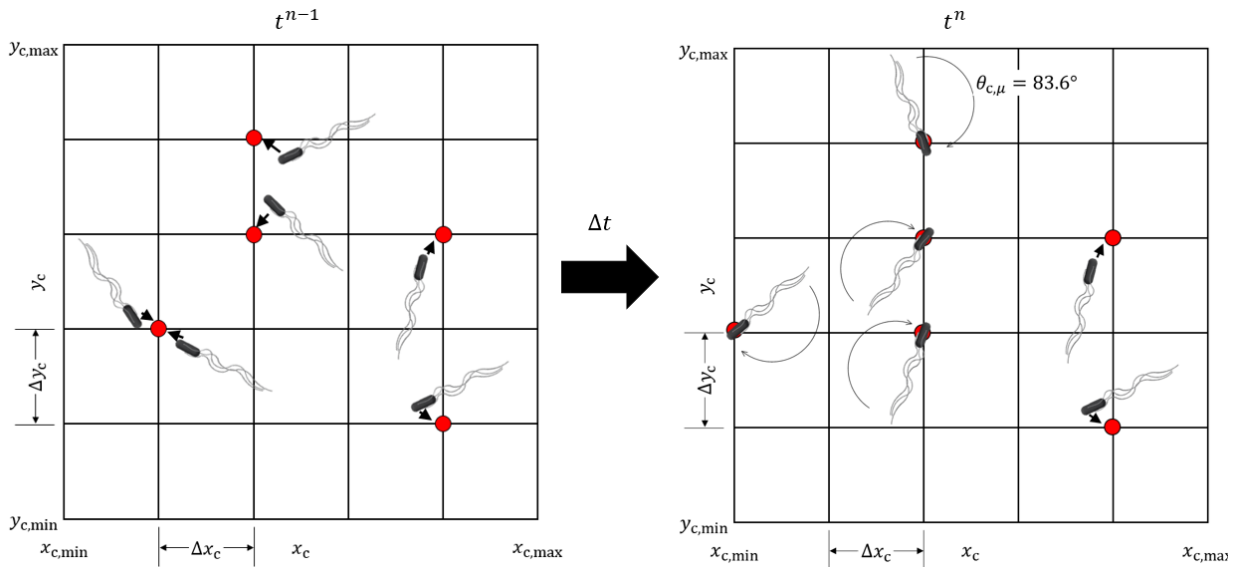


Figure 2.8: Efficient Modelling of Cell-cell Collision Events. At time  $t^{n-1}$ , agents located in continuous space are counted on the discrete interactions mesh at the nodes indicated (left). In the following time step, agents whose positions were recorded adjacent to or overlapping with other agents were relocated and reoriented instantaneously (right). Note that the two agents near the right-hand side border in both subfigures were not disturbed since they were more than  $\Delta s_c$  from one another as determined by the distance between their nearest nodes ( $\Delta x_c = \Delta y_c = \Delta s_c$ ).

and should well-approximate bacterial aggregation and space exclusion due to physical size alone. In simulations, the mesh spacing was set to  $2\ \mu\text{m}$ , approximately half the measured length of bacteria corresponding to the scenario being modeled. From a physical standpoint, this treatment is equivalent to modeling the agents as spheres with radii equal to half their body length.

Figure 2.9 shows the effects of different internodal spacing values for a non-reproducing population of 500 chemotactic agents. The plot on the left demonstrates how population density is affected and limited depending on the distance between agents for interactions to occur. To reduce noise due to the stochastic movement of agents, the final 10 minutes of data from a 60-minute simulation was averaged to produce the curves shown. The plot on the right-hand side of Figure 2.9 shows the random walk of 50 agents over a 1000-second simulation with a mesh spacing of  $100\ \mu\text{m}$ . This large spacing value was chosen to show the emergent structure of the mesh due to the frequent repositioning of agents as they interacted.

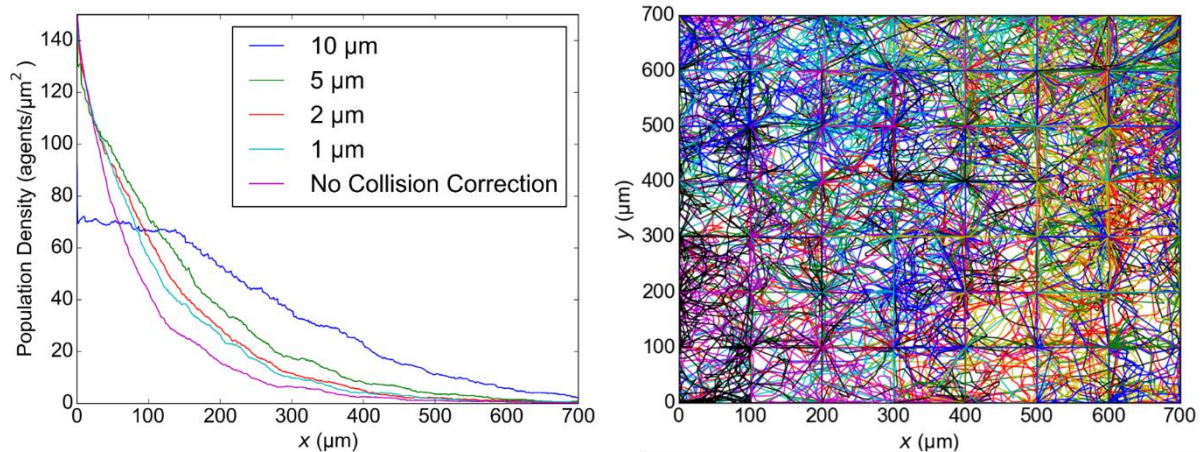


Figure 2.9: 10-minute Average of Population Density as a Function of  $x$ -location (left) and the Emergent Structure of a Coarse Interactions Mesh as Demonstrated by Trajectories of 50 Agents over a 1000 s (right)

### 2.6.3 Model Information and Process Flow

A simulation begun by constructing a list of agents and randomly assigning a run or tumble phase.

During each time step, the list of agents is iterated one by one to allow each to interact with its

environment. A chart showing the main flow of information and processes is shown in Figure 2.10. If the simulation involved QS, then each agent released a number AHL molecules into the nearest four concentration field nodes according to the rate calculated from Equation 2.10,  $N_{QS}(x, y) = A_t(x, y)\Delta t$ . The specific number that was input into each node was interpolated linearly, as were concentration values sensed by the agents. If the current agent represented a QQ bacterium, then a fraction of the local AHL is removed based on the result of Equation 2.15,  $N_{QS}^-(x, y) = Q^-(x, y)\Delta t$ . Next, motility functions were called, causing the agent to take a step in space according to  $\vec{V}_b\Delta t$  or to remain stationary if it was in the tumble phase. In either case, running or tumbling, the timer for that respective phase was compared to the time step to determine if it was time for the agent to change phase. That is, if  $\Delta t \geq \tau_{\text{remain}}$  then new timers were set and the bacterium started the next time step in the opposite phase. With each iteration within the list of agents, the procedure described in Section 2.6.2 was performed to adjust positions based on physical interactions. At the end of the time step, the mesh was updated with counts of agents at each node.



### 2.6.4 Investigation of the Effects of Mesh Size and Time Step on Model Predictions

A critical parameter of any numerical model is proper selection of both time step and mesh size (or mesh spacing) such that further reduction or refinement does not significantly impact the results of interest. To test for this, the impact of the time step selection was first evaluated with respect to agent chemotaxis behavior. The results were quantified using the CMC (chemotaxis migration coefficient) metric, which is a measure bacteria distribution in response to a chemoeffector and is defined as

$$\text{CMC} = \frac{2 \sum xN(x)}{w \sum N(x)}, \quad 2.18$$

where  $N(x)$  is the number of agents located at location  $x$  and  $w$  is the width of the domain. Figure 2.11 shows the CMC as a function of time for a  $700 \times 700 \mu\text{m}^2$  domain at three different time steps. Note that each trace oscillates about the same mean CMC value, indicating that the time step selection has little impact on the agent localization.

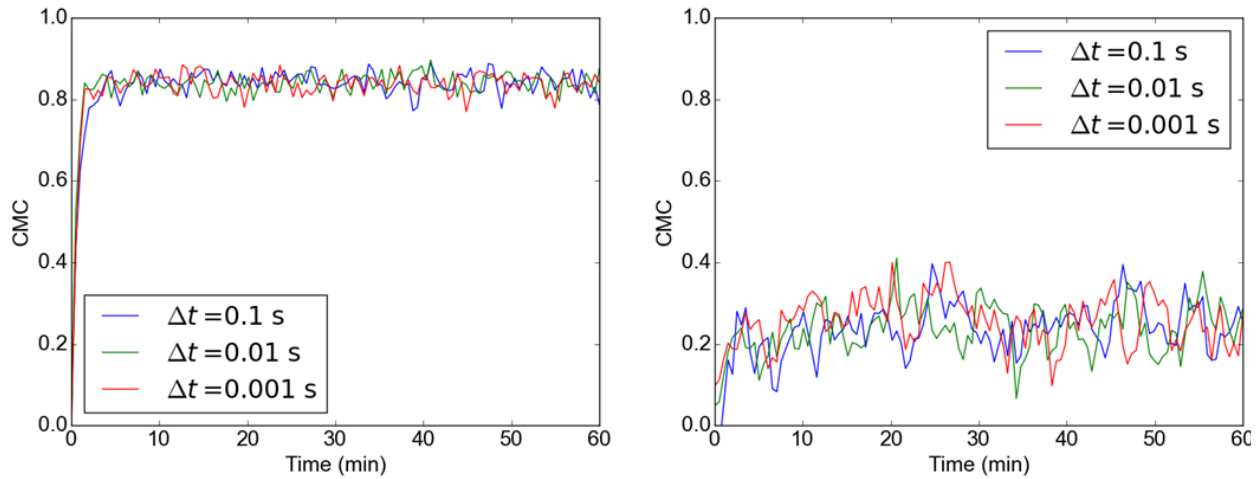


Figure 2.11: The Effect of Time Step on Simulated Chemotaxis for an Optimized Chemical Gradient (left) and a Non-optimal Chemical Gradient (right)

Since the primary metric associated with QS studies was the activation time, this was used as a metric to investigate the effects of mesh size and time step on emergent behavior. The QS activation time was defined as the time when a detectable threshold concentration of mature GFP (assumed to be on the order of 100 nM) had accumulated inside cells (averaged over the population in the first 50  $\mu\text{m}$  of the domain). It was found that mesh size had a significant impact on this result if a small steady population size (50 agents) was used. The results of a mesh refinement study are shown in Figure 2.12a. In contrast, the mesh size had little effect on simulations when an experimentally-measured growth rate was used. This was likely due to AHL concentrations being forced to be more homogenous for coarser meshes versus finer meshes. In simulations with larger numbers of agents (*i.e.* a growing population), concentrations are relatively homogeneous regardless of mesh size, meaning that using a coarser mesh produces little change in activation time. Figure 2.12b shows mean activation time versus mesh size for the case that with the greatest experimental activation time (270 min; detailed experimental results are in Section 3.4.3). The physical domain size was  $2100 \times 2100 \mu\text{m}^2$ . Note that a large difference was observed between the two coarsest meshes (50 $\times$ 50 nodes and 100 $\times$ 100 nodes), but differences were relatively small

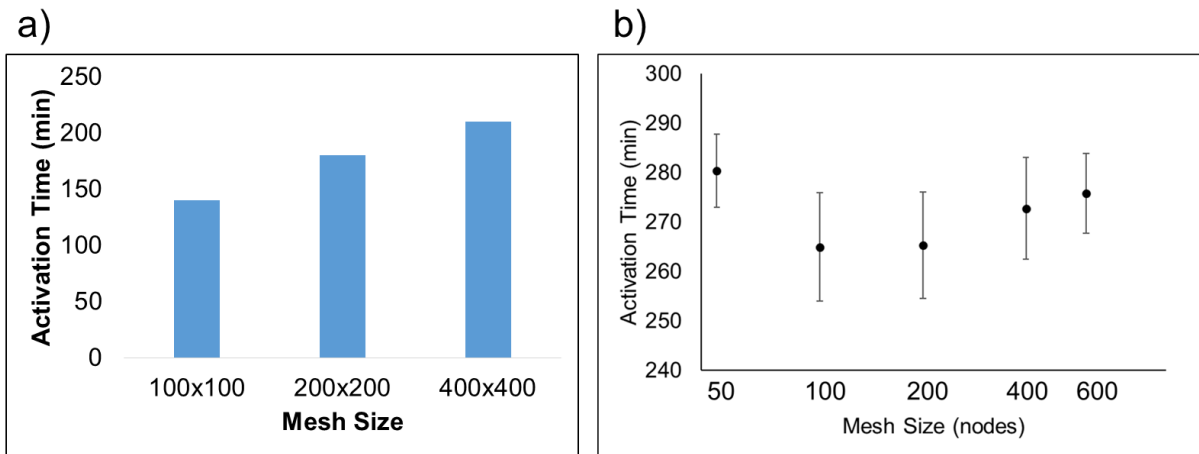


Figure 2.12: The Effect of Mesh Size on Activation Time for (a) a Static Population of 50 Agents and (b) the “weakest” experimentally-tested QS construct with a growth rate defined by  $P^*(t) = 0.073t + 1$

thereafter. Since the relative change between a  $100\times 100$  mesh and  $600\times 600$  mesh was less than 5%, all simulations were run using this mesh size.

## **Chapter III: Experimental Validation of the Model**

In order to ensure that the model accurately recapitulates chemotaxis as a function of chemoattractant gradient and emergent QS behavior for a variety of initial conditions, degrees of localization, a community with QQ bacteria, and variance in AHL generation rates, a series of microfluidic experiments were performed to validate model results. First, chemotaxis assays were performed for gradients of L-aspartic acid spanning three order of magnitude. Optimizing the kinetic parameters resulted in modeled chemotaxis migration coefficients (CMCs) within about 8% of experimental measurements. The model was then used to predict QS activation times in a series of experiments with various starting conditions in order to determine AHL generation parameters. The utility of the model as a design tool was demonstrated by predicting activation for greatly decreased generation rates, which was implemented in practice by designing synthetic ribosomal binding sites (RBSs) to scale rates of protein translation. Finally, the model was used to show the importance of spatial distribution in emergent behavior, including in a microbial community with QQ bacteria.

### **3.1 Microfluidic Platform Utilized for Chemotaxis and QS Experiments**

A microfluidic platform previously developed in our lab [103] to study bacterial responses to chemical gradients was used to perform chemotaxis assays and QS/QQ experiments. This device has several advantages, including ease of fabrication, low cost, spatiotemporal invariance in the chemo-effector gradient [104], and ease of modeling the environment created inside.

#### *3.1.1 Microfluidic Device Design*

The microfluidic device used for experiments was previously developed by Traore and Behkam [103], who described the fabrication and design of the device in detail. In short, the device, shown schematically in Figure 3.1a, utilizes a polyethylene glycol diacrylate (PEG-DA)-based gel to

separate three parallel, fluid-filled channels. The device is sealed by a glass slide on the bottom and by a slab of polydimethylsiloxane (PDMS) on the top, sandwiched between two pieces of Plexiglass and clamped together using four bolts (Figure 3.1b and 3.2b). By establishing flow of a buffer solution through one of the outside channels and chemo-effector solution in the opposite outside channel, a constant-concentration boundary condition is imposed on the inner PEG-DA walls that border the flow. At steady state, a quasi-linear chemical gradient is established across the width of the center channel. For experiments, a bacterial suspension was flowed into the center channel, and the inlet and outlet were sealed to prevent flow, which would have disrupted the gradient.

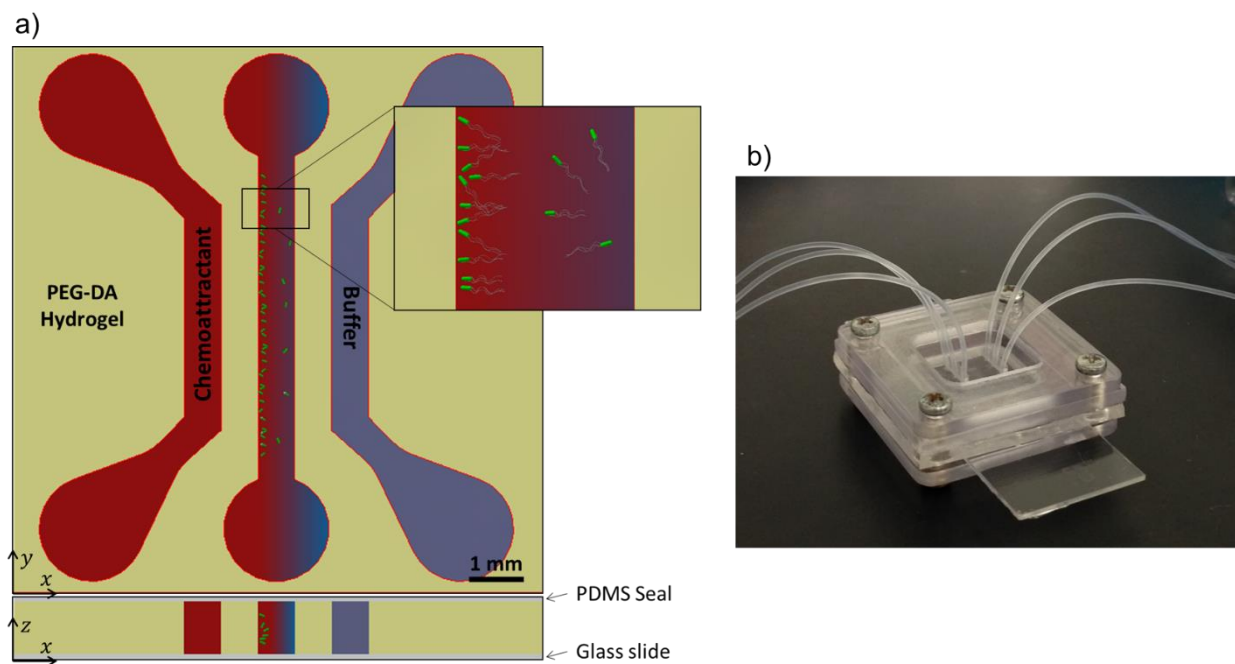


Figure 3.1: Microfluidic Device used for Experiments. **(a)** A schematic of the device design, layout, and function, and **(b)** a photograph of a fully-assembled device

### 3.1.2 Device Fabrication

Microfluidic devices were fabricated following the protocol in [103]. First, a new  $4 \times 1$  in<sup>2</sup> glass microscope slide was cleaned by rinsing with acetone, followed by deionized (DI) water and

isopropyl alcohol (IPA). The slide was then air dried, and liquid PDMS (10:1 base-to-curing agent; Dow Corning, Auburn, MI) was spin-coated onto the top surface for 30 s at 800 RPM resulting in an approximate 100  $\mu\text{m}$ -thick PDMS film. After curing for 4 hr at 70° C, a rectangular piece of the film was cut out of the center, and the glass surface was re-cleaned using IPA, acetone, and DI water, concluding with a final IPA rinse. The slide was air-dried and cleaned in air plasma for 40 s (200 mTorr, 18 W) to remove organic surface contaminants. The surface of the cleaned substrate was functionalized at room temperature by adding a monolayer of 3-(trichlorosilyl) propyl methacrylate (TPM; Sigma-Aldrich, St. Louis, MO) using a 1% solution in mineral oil to promote bonding with PEG-DA gel. After hard-baking the TPM at 95° C for 30 min, a large droplet of liquid PEG-DA (Sigma-Aldrich) solution supplemented with 0.5% (w/v) Irgacure 2959 (Sigma-Aldrich) photoinitiator was placed on the treated glass inside the rectangular cutout. The desired channel height was achieved by placing a coverslip on top of the PDMS-coated slide, causing the PEG-DA to fill the rectangular enclosure created by the PDMS-cutout region. A photomask printed with the desired pattern was placed on top of the coverslip, and the PEG-DA was cross-linked to form a gel by exposing to broadband ultraviolet (UV) light (320-500 nm;  $\sim 340 \text{ mJ/cm}^2$ ). Patterned slides were soaked in 70% ethanol for at least 8 hr followed by PBS for  $\sim 20$  min prior to being used for assembly to remove excess photoinitiator. Figure 3.2 shows the patterning and assembly process.

### *3.1.3 Microfluidic Device Modeling*

In order to determine the concentrations required to establish the desired steady state chemical gradients in the device, as well as to determine the time required to reach steady state, simulations were performed using the COMSOL Multiphysics finite element-based software package (COMSOL Inc., Burlington, MA). Figure 3.3a shows the normalized concentration of L-aspartic

acid, the chemoattractant used for chemotaxis model validation, at steady state. The diffusivity was assumed to be equivalent to that of fluorescein since the two compounds have similar molecular weights (133 Da and 232 Da, respectively). The diffusivity of fluorescein was taken to be  $2.7 \times 10^{-6} \text{ cm}^2/\text{s}$  and  $1.8 \times 10^{-6} \text{ cm}^2/\text{s}$  in PBS (phosphate buffered saline) and 700 Da PEG-DA (same MW used in all experiments), respectively [103]. In the COMSOL simulation, these values were employed locally according to regions of gel or liquid-only. Quasi-steady state chemical gradients were established after approximately 45 minutes. Figure 3.3b shows several concentration profiles between the side channel walls plotted at various points in time.

For all QS experiments, casamino acids, rather than L-aspartic acid, was used as a chemoattractant unless otherwise noted. Similar COMSOL simulations were performed to determine the flow channel concentrations required to produce the optimum gradient for *E. coli* chemotaxis ( $5 \times 10^{-4} \text{ g/ml/mm}$ ) based on diffusivities in PBS and PEG-DA (700 Da) of  $8.0 \times 10^{-6} \text{ cm}^2/\text{s}$  and  $1.5 \times 10^{-6} \text{ cm}^2/\text{s}$ , respectively [105].

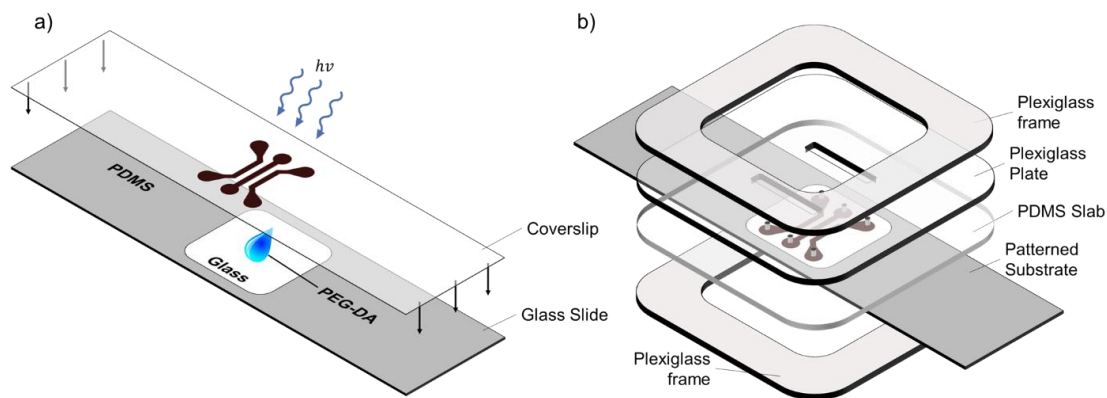


Figure 3.2: Fabrication of Microfluidic Device. **(a)** The hydrogel pattern was made by depositing a small amount of liquid PEG-DA onto a bare glass cutout framed by PDMS and sealing with a coverslip prior to UV exposure. **(b)** The device was then assembled by sandwiching the patterned slide and a PDMS slab sealing layer between Plexiglass.

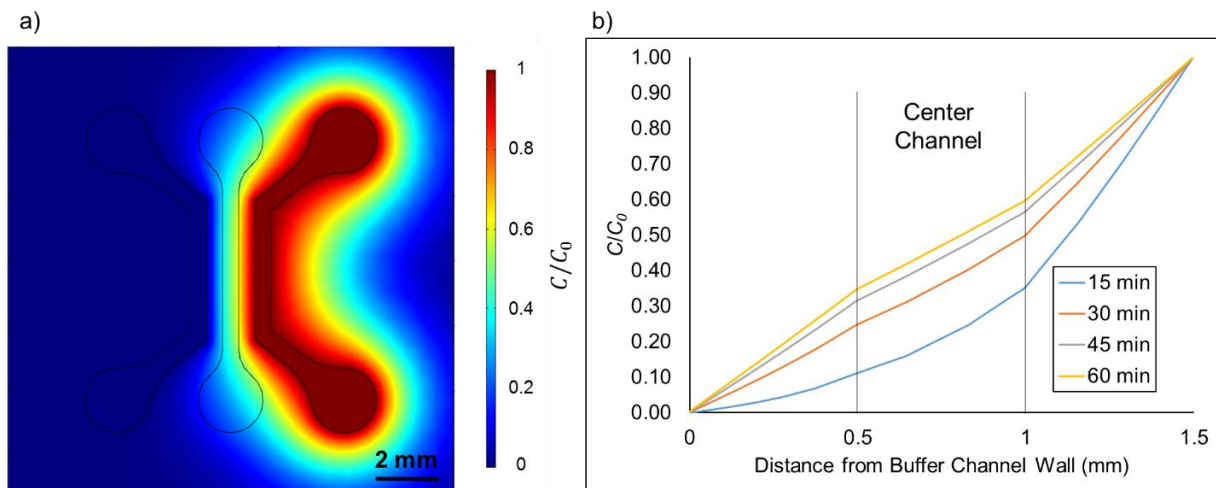


Figure 3.3: COMSOL Simulations of L-aspartic Acid Diffusion in PEG-DA Device. (a) normalized concentration at steady state and (b) normalized concentration profile at various points in time between the source and sink (chemoattractant and buffer, respectively) channels

### 3.2 Experimental Validation of the Chemotaxis Model

The chemotaxis model was validated independent of the QS model by measuring the steady state CPC and CMC of a population of highly-motile *E. coli* MG1655 in a PEG-DA microfluidic device with 500  $\mu\text{m}$ -wide channels and walls (spacing between each channel) at various L-aspartic acid gradients. These results were then used to determine optimal values of the product  $\sigma C_T$  and the dissociation constant  $K_D$  that gave the least amount of error between modeled and measured values. Given the accuracy of the model, the experimentally-determined motility parameters, and the biological-relevance of the fitted parameters, this model could be used to predict chemotaxis responses in a variety of hypothetical settings.

#### 3.2.1 Microfluidic Experiments and Data Analysis

Much of the data for chemotaxis model validation was derived from experiments performed previously in our lab by Sahari *et al.* [106]. Nevertheless, all experiments were performed according to the same protocol and all previously recorded images were re-processed and re-measured for chemotaxis metrics.

Chemotaxis experiments were performed using *E. coli* MG1655 that were isolated for increase motility and expressing the plasmid pHC60 for constitutive GFP expression [107], [108]. Bacteria were grown for experiments by diluting overnight cultures 100× and shaking at 32° C and 150 RPM in tryptone broth (1% tryptone, 0.5-1% NaCl) supplemented with 10-15 µg/ml oxytetracycline until an OD<sub>600</sub> of 0.5 was reached. The bacteria were then resuspended in motility buffer (0.01 M potassium phosphate, 0.067 M sodium chloride, 10<sup>-4</sup> M ethylenediaminetetraacetic acid, 0.01 M glucose, and 0.002% (v/v) Tween-20, pH=7.0) and diluted to an OD<sub>600</sub> of either 0.05 or 0.10 before introduction into the microfluidic device. Prior to the start of an experiment, a linear gradient of L-aspartic acid was established by flowing the chemoattractant solution and motility buffer alone through the outer channels of the device for at least 45 min. This allowed the same linear gradient to be re-established quickly after flowing bacteria into the center channel. Experiments were performed at room temperature.

Measurements of cell size and swimming speed were made on dilute suspensions of the bacteria inside the microfluidic device and used as the corresponding parameters in simulations. The mean cell length and diameter were found to be 2.55±0.61 µm and 0.85±0.16 µm, respectively (*N*=50). The mean swimming speed, which was measured using the “Manual Tracking” plugin for ImageJ (National Institutes of Health, Bethesda, MD), was found to be 51.7±7.2 µm/s (*N*=51). This speed was used as the constant agent swimming speed  $|\vec{V}_b|$  in the motility model.

Fluorescence images of steady-state bacterial distributions were recorded and analyzed using a custom image processing routine developed in ImageJ. Images (recorded across the channel width) were first cropped to remove the PEG-DA walls where a few cells inevitably became lodged during experiments (Figure 3.4a). The images were then corrected for background fluorescence using the “Subtract Background” tool with a rolling ball radius of 50 px [109]. Images

were smoothed by averaging pixel intensities over localized  $3 \times 3$  px<sup>2</sup> bins in one to several iterations depending on the amount of noise in the original image (determined by comparing the results and raw images manually). Edges of individual cells were detected using a Sobel edge detector, and images were then made binary by local Bernsen thresholding using a 15 px radius [110]. The result was a binary image with minimal noise or clumps of coalesced cells (inverted image shown in Figure 3.4b). Finally, these images were segmented using the “Analyze Particles” tool of ImageJ, which counts discrete objects by detecting edges and attempting to trace the border of the object (Figure 3.4c). By first detecting edges and then locally thresholding the image, the routine robustly and consistently segmented individual cells in various experiments and for differing cell densities.

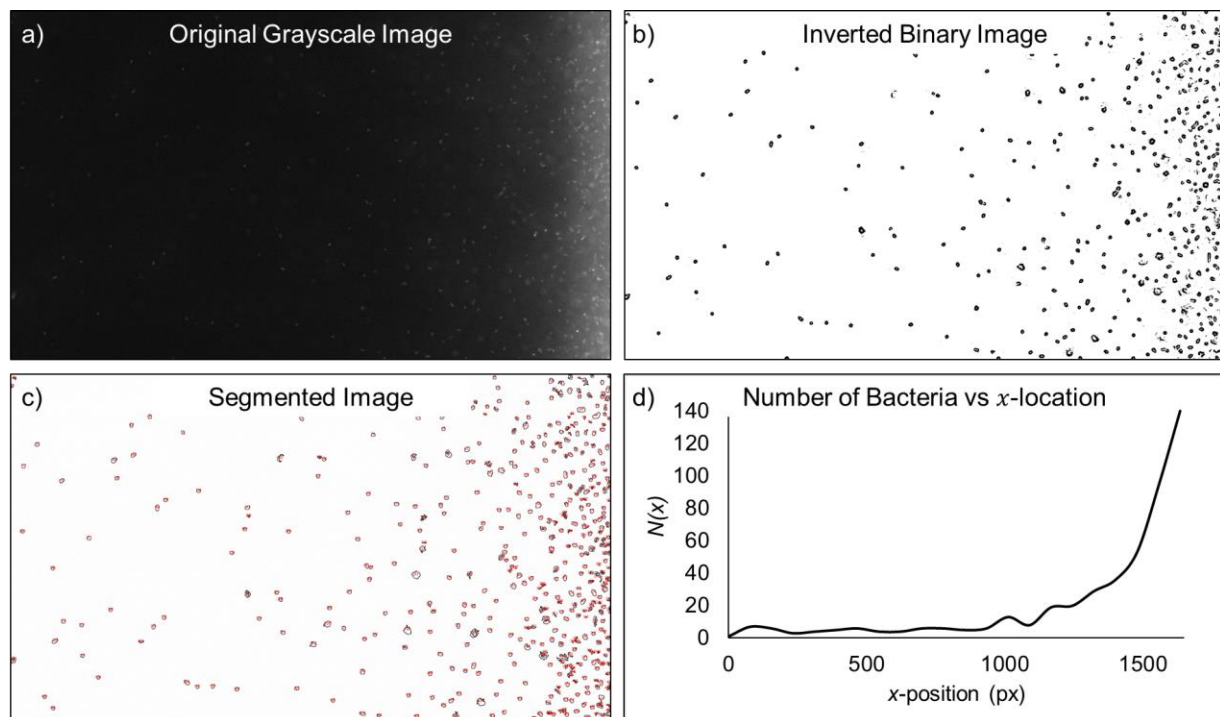


Figure 3.4: Image Processing for Measuring Chemotaxis Metrics. **(a)** original micrograph, **(b)** the inverted, binary image produced following background correction, smoothing, edge detection, and Bernsen thresholding of **(a)**, **(c)** the final segmented image showing discrete objects counted as cells, **(d)** a plot of the number of bacteria vs location on the horizontal axis (dimension along the width of the microfluidic channel)

The locations of segmented cells were used to calculate the CPC and CMC metrics for comparison to simulation results. The CPC and CMC are defined as

$$\text{CPC} = \frac{N_{\text{RHS}} - N_{\text{LHS}}}{N_{\text{RHS}} + N_{\text{LHS}}} \quad 3.1$$

and

$$\text{CMC} = \frac{2 \sum xN(x)}{w \sum N(x)}, \quad 3.2$$

where  $N_{\text{RHS}}$  and  $N_{\text{LHS}}$  is the number of bacteria in the right-hand half and left-hand half of the channel, respectively,  $N(x)$  is the local number of bacteria along the channel width ( $x = 0$  at the center), and  $w$  is the total width of the channel.

### 3.2.2 Determination of Kinetic Parameters and Model Validation

The kinetic parameters  $\sigma C_T$  and  $K_d$  in Equation 2.9 were determined using a differential evolution algorithm (`differential_evolution` of the `scipy.optimize` module) to stochastically search for values that minimized the sum of the squared error between the model and measured results [111]. Bounds for the optimization scheme were determined by estimating biologically-realistic ranges for the parameters. It was assumed that the product  $\sigma C_T$  for *E. coli* responding to L-aspartic acid was near the value of 75 s determined by Ford and Lauffenburger [63] for gradients of serine. The *E. coli* Tar receptor has been suggested to exist in both active and inactive conformations, which have lower and higher  $K_D$  values, respectively [70]. Published estimates of the apparent value vary by approximately an order of magnitude, with many estimates falling near 3-6  $\mu\text{M}$  [70], [71], [112], [113].

Simulations were performed using a  $500 \times 500 \mu\text{m}^2$  domain with 100 agents initiated at random locations. Since the channel of the microfluidic device was long ( $\sim 6$  mm), periodic boundary conditions were used for agents moving across the  $y$ -limits of the domain. Channel walls

were modeled as hard stops employed at the  $x$ -limits. That is, an agent moving past one of these limits was stopped and held stationary until a tumble event caused it to be reoriented away from the boundary. This was assumed to recapitulate the experimental response as obstacles have been observed to cause cells to “idle” during the run phase [114], [115]. The chemoattractant concentration profile was employed as a continuous linear function of  $x$  according to steady-state COMSOL results. For an individual simulation, CPCs and CMCs were determined by taking an average over the final 10 min of simulated data. Final model results are reported as the average  $\pm$  standard deviation of these values over 10 simulations.

Figure 3.5 shows the results of the optimized chemotaxis simulations as well as the experimental measurements. The best value of  $\sigma C_T$  was determined to be 47 s, and the optimized  $K_D$  was found to be 18.0  $\mu\text{M}$ . It was assumed that these numbers represent biologically realistic parameters given their agreement with published results. One possible explanation for finding a somewhat high  $K_D$  value is that the bacteria used in experiments were derived from a highly-motile subpopulation isolated according to the methods described in [108]. Since isolation of these

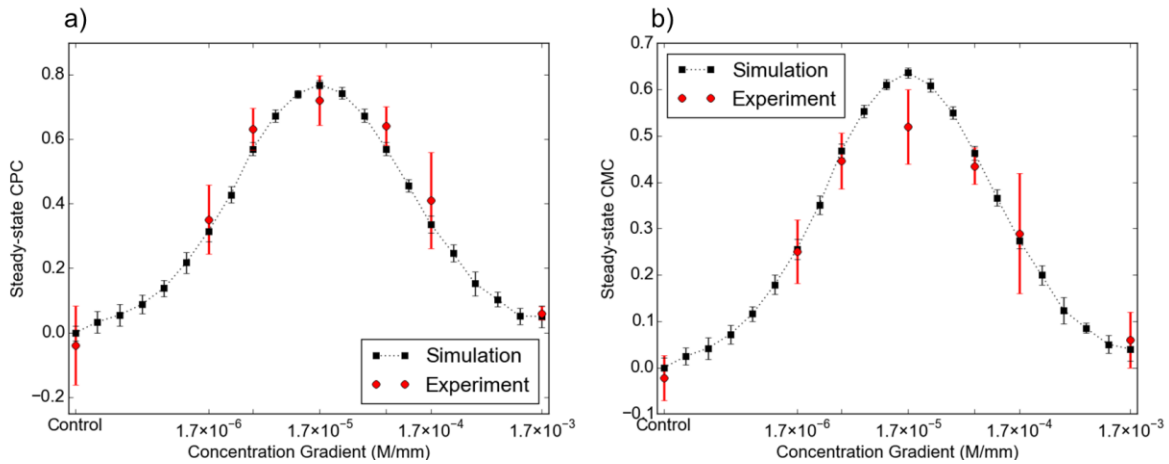


Figure 3.5: Simulated and Experimental Chemotaxis Response as Measured by (a) CPC and (b) CMC

cells depends on their ability to outperform the bulk population with respect to chemotactic migration, it is reasonable to assume that they may possess a larger fraction of active Tar receptors.

After optimizing the kinetic parameters, the model correctly predicted steady state CPCs and CMCs for L-aspartic acid gradients spanning three orders of magnitude within about 11% and 8.2%, respectively, on average (end points at 0 M/mm and  $1.7 \times 10^{-3}$  M/mm not included in error calculation). Most error in CMC is due to data at the peak response, however. This can be attributed to the fact that bacteria localized along edge of the microfluidic channel cannot be accurately counted and are excluded from experimental analysis. This is not a limitation in simulation, thus the simulated CMC values at gradients giving a strong response better capture experimental results than Figure 3.5 indicates. Excluding this data point, the mean relative error in CMC is 4.6% Table 3.1 summarizes the parameters used in the model for chemotaxis validation.

Table 3.1: Parameters used in Simulations for Chemotaxis Model Validation

Parameter	Variable	Value	Source
Average run duration in absence of chemo-effector gradient	$\tau_0$	0.6 s	[83]
Average tumble duration	$\tau_T$	0.16 s	[83]
Chemotactic Sensitivity	$\sigma C_T$	47 s	Estimated
Dissociation constant for L-aspartic acid binding with the Tar receptor	$K_d$	18 $\mu$ M	Estimated
Magnitude of the bacterial velocity vector (cell swimming speed)	$ \vec{V}_b $	$51.7 \pm 7.2$ $\mu$ m/s	Measured
Mean change in bearing between successive run phases	$\theta_{T,\mu}$	$42^\circ$	[83]
Standard deviation in bearing change between run phases	$\theta_{T,\sigma}$	$36^\circ$	[36]
Time step	$\Delta t$	0.1 s	N/A

### 3.3 Experimental Validation of QS Model

QS behavior in bacteria can often be characterized as a switch-like change in gene expression in response to a threshold concentration of AI being surpassed in the local environment [19], [116]–

[118]. Given that there currently is no precise method by which to measure transient AHL concentrations during experiments, this trait was utilized to define a QS activation time as the metric by which to compare simulations to experiments. To this end, a variety of experiments were performed in order to validate model assumptions, determine parameters for the model, and to test whether or not the model could be used to predict the activation time for variant QS constructs and in heterogeneous cell populations.

### 3.3.1 Measurement of the Effective Diffusivity of a Small Solute in Dense Populations of Motile Bacteria

As alluded to in Section 2.3, a series of experiments were performed in order to validate the assumption that diffusion dominates advection in the transport of AHL in motile cell suspensions. Experiments were modeled after those by Kim and Breuer [95], who measured the effective diffusion of a macromolecular substance (77 kDa Dextran labeled with FITC) in suspensions of *E. coli* up to approximately  $2 \times 10^9$  CFU/ml in density. This was accomplished by measuring fluorescence intensity profiles and comparing the result to an analytical solution. While these

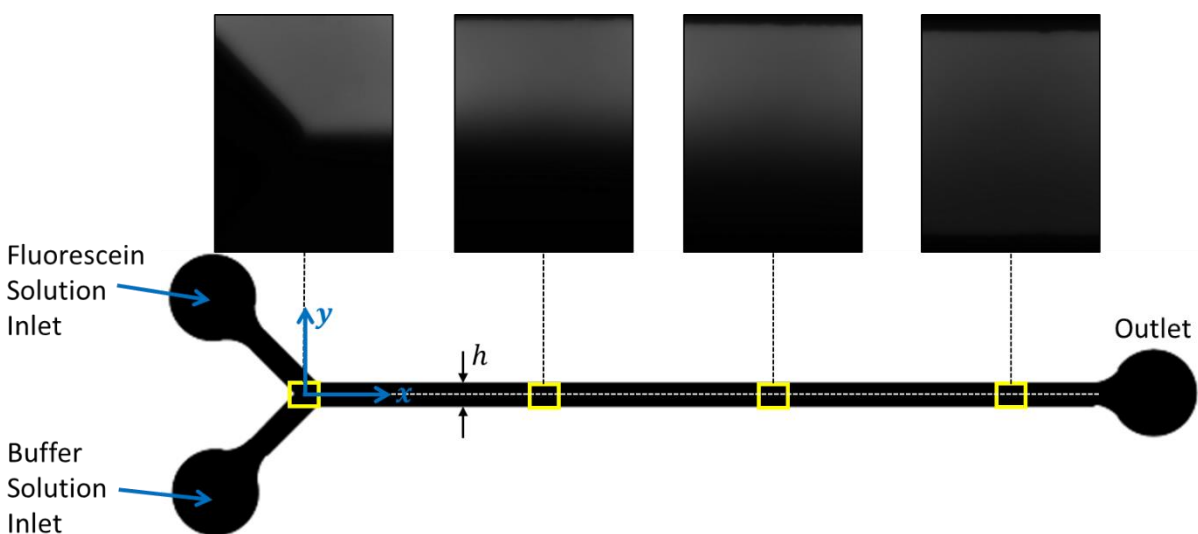


Figure 3.6: Schematic of the Microfluidic Device Used to Measure Effective Diffusivity in the Presence of Motile Bacteria

researchers found that diffusivity was enhanced by up to 8-fold, the basal diffusion coefficient of the substance is three orders of magnitude smaller than that which was assumed for AHL. Pure fluorescein was therefore used in our experiments, as it is a small molecular substance with a similar diffusivity in water as AHL. Figure 3.6 shows the microfluidic device used for these experiments.

Microfluidic devices were fabricated according to standard soft lithography techniques. Briefly, SU-8 2025 (MicroChem, Westborough, MA) was spin coated onto a silicon wafer for a film thickness of 85  $\mu\text{m}$  and patterned with a photomask, followed by treatment with trichloro(1H,1H,2H,2H-perfluorooctyl) silane (Sigma-Aldrich) to render the surface hydrophobic. Microfluidic channels were molded in PDMS by casting over the SU-8 template. The devices were completed by bonding the PDMS to glass slides.

The design of the microfluidic device shown in Figure 3.6 takes advantage of the fact that its geometry dictates a laminar flow regime over a large range of flow rates. This feature precludes mixing of the two inlet streams by advection. Transport of a chemical species in the channel is therefore governed by

$$\frac{\partial C}{\partial t} = D_{\text{eff}} \left( \frac{\partial^2 C}{\partial x^2} + \frac{\partial^2 C}{\partial y^2} \right) - u \frac{\partial C}{\partial x} \quad 3.3$$

where  $C$  is the concentration of the solute,  $D_{\text{eff}}$  is the effective diffusion coefficient, and  $u$  is the streamwise velocity. For sufficiently high flow rates, diffusion in the  $x$ -direction can be neglected as advection is primary mechanism of streamwise transport. Coupling this assumption with steady flow, Equation 3.3 reduces to

$$\frac{\partial C}{\partial x} = \frac{D_{\text{eff}}}{u} \frac{\partial^2 C}{\partial y^2} \quad 3.4$$

which has the general solution

$$C(x, y) = A + B \operatorname{erf}\left(\frac{y}{2\sqrt{D_{\text{eff}}\frac{x}{u}}}\right), \quad 3.5$$

where  $A$  and  $B$  are constants. At  $x = 0$ , the normalized concentration in the device is given by

$$C(0, y) = \begin{cases} 0 & \text{for } -h/2 \leq y < 0 \\ 1 & \text{for } 0 < y \leq h/2 \end{cases}$$

indicating that  $0 = A - B$  and  $1 = A + B$  must be satisfied. Noting that the normalized concentration at  $C(x, 0) = 1/2$  for all  $x$ ,  $A = B = 1/2$ .

Since fluorescence intensity is linearly proportional to fluorophore concentration, Equation 3.5 can be used to find  $D_{\text{eff}}$  given a measured intensity profile at a location  $x$  for a known velocity  $u$  [119]. Following Kim and Breuer's approach [95], fitting the gradient of the theoretical concentration profile to the gradient of normalized fluorescence measurements rather than fitting Equation 3.5 directly provided better sensitivity to  $x$ -location and resulted in less variability between results. That is,

$$\frac{\partial C}{\partial y} = -\frac{1}{2\sqrt{\pi D_{\text{eff}}\frac{x}{u}}} \exp\left(-\frac{y^2}{4D_{\text{eff}}\frac{x}{u}}\right). \quad 3.6$$

Experiments were carried out by flowing a 100  $\mu\text{M}$  fluorescein solution in chemotaxis buffer (CB;  $1\times$  PBS, 0.1 mM EDTA, 0.01 mM L-methionine, and 10 mM DL-lactate [120]) or CB alone at equal rates into each of the inlet ports. For each scenario tested, approximately equal concentrations of *E. coli* were suspended in each of the solutions. For each set of experiments, flow rates ( $Q$ ) of 0.5  $\mu\text{l}/\text{min}$ , 1  $\mu\text{l}/\text{min}$ , and 2  $\mu\text{l}/\text{min}$  were established using a syringe pump (PHD Ultra, Harvard Apparatus, Holliston, MA). The velocity  $u$  was taken as the mean velocity in the channel,  $u = Q/A_c$  where  $A_c$  is the channel cross-section normal to the flow. Each time the flow rate was changed, steady state was allowed to establish for a short period of time ( $\sim 2$  min) before

recording images at known locations along the length of the channel. A set of baseline images was also recorded by flowing a 100  $\mu\text{M}$  fluorescein solution through both of the device inlets.

For these experiments, *E. coli* MG1655 harboring a plasmid with only BBa\_K546000 (the *luxIR* components of the QS circuit) were cultured overnight at 37° C and 100 RPM in lysogeny broth (LB; 1% tryptone, 0.5% yeast extracts, 1% NaCl) supplemented with 35  $\mu\text{g/ml}$  chloramphenicol and diluted 100 $\times$  to start fresh cultures. The bacteria were harvested at an OD<sub>600</sub> of 1.0 and concentrated approximately 1 $\times$ , 2 $\times$ , 10 $\times$ , and 20 $\times$  in CB and a solution of fluorescein in CB.

Data analysis was performed using a custom image processing routine written in Python. All images were output using the same set of parameters as high-quality TIFF files (0.323  $\mu\text{m/px}$ ). Each image was then normalized to its respective baseline image to remove intrinsic biases in the photodetector, excitation source, etc. Measurements of the fluorescence intensity were made by integrating the data over approximately 33  $\mu\text{m}$ -wide bins (10 per image) stretching between the channel side walls. It was assumed that the small variation in  $x$  within each bin was negligible. The gradient of each profile was calculate using second-order accurate central differences, and the optimal value of  $D_{\text{eff}}$  was calculated from a least-squares fit of Equation 3.6 (in practice, this was implemented by calculating the gradient of Equation 3.5 in a manner identical to that used for experimental data). It was observed during data acquisition that small perturbations in the pressure of each stream occurred transiently, causing the interface between the two streams to shift in  $y$  slightly. To correct for this, an optimum offset was also calculated such that  $y_0 = y - y_{\text{offset}}$  where  $y_0$  is defined as the location of the peak of the absolute value of the gradient. It was assumed that these disruptions in steady flow averaged out over experiments. Figure 3.7 shows examples of data processing and the fitting of an optimized theoretical gradient.

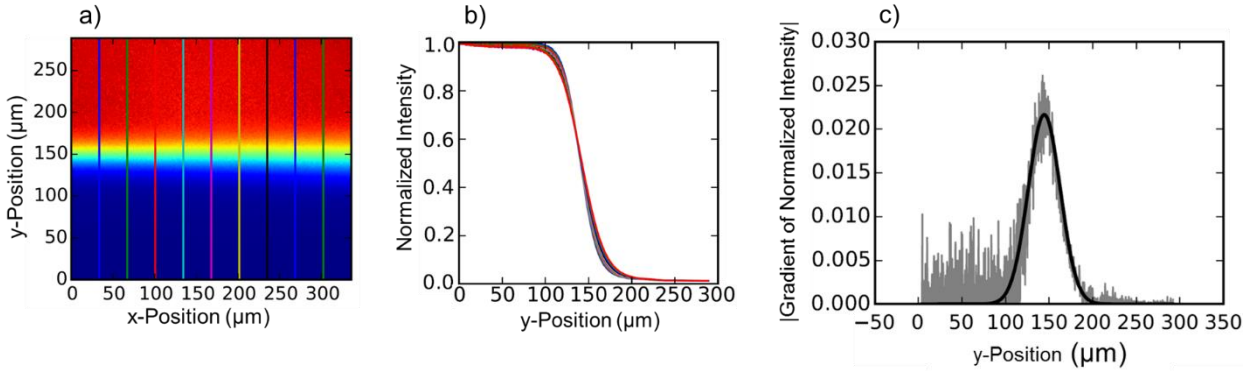


Figure 3.7: Image Processing and Data Analysis for Diffusivity Measurements. **(a)** An example heat map showing fluorescence intensity at a location centered 0.48 mm downstream of the Y-channel junction and the bins used to calculate 10 discrete values of  $D_{\text{eff}}$  (red indicates 1, blue indicates 0), **(b)** the normalized fluorescence intensity profiles in each bin shown in (a), and **(c)** the absolute value of the intensity gradient for the 5<sup>th</sup> bin shown in (a) (gray) and the best fit of the theoretical gradient (black)

The resulting measurements of  $D_{\text{eff}}$  are shown in Figure 3.8. Each final result was taken as the mean of optimized values of  $D_{\text{eff}}$  across all bins and imaging locations between 0.48 mm and 16.22 mm ( $N=20$  images) downstream of the Y-junction. No significant differences between any of the five cases were found, even for extremely dense suspensions of approximately  $10^{10}$  CFU/ml. Moreover, no trend was observed with respect to bacterial density, validating the assumption that advection may be neglected in the model of AHL transport. The mean of approximately  $250 \mu\text{m}^2/\text{s}$  is consistent with values reported in literature for aqueous solutions of fluorescein [121], [122] (although it should be noted that larger values have also been reported [123]).

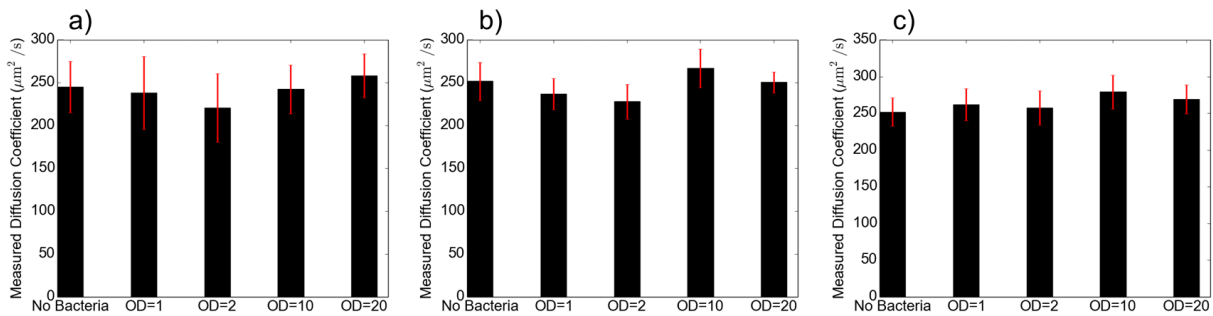


Figure 3.8: Results of Diffusivity Measurement Experiments. **(a)** 0.5  $\mu\text{l}/\text{min}$ , **(b)** 1.0  $\mu\text{l}/\text{min}$ , and **(c)** 2.0  $\mu\text{l}/\text{min}$ . Error bars show  $\pm$  standard deviation.

### 3.3.2 Experimental Methods for QS Validation

In order to validate the model for QS activation time, the microfluidic device described in Section 3.1.3 (except with 700  $\mu\text{m}$ -wide channels and spacing between channels) was used to create a locally dense bacterial population via chemotaxis. This made an excellent setting to study emergent behavior that could be relevant in practical applications, such as bacterial biosensors chemotactically migrating to a source of an environmental toxin or the localized production of therapeutic drugs inside a tumor [1], [87]. Casamino acids (CA) was used as a chemoattractant for QS experiments rather than a simple amino acid, as it provided for greater localization and a more robust response. As in chemotaxis experiments, the chemoattractant and buffer solution were flowed through the two side channels of the microfluidic device for at least 45 min to allow quasi-steady conditions to be established before introducing bacteria. It was found that the bacteria were unable to become QS-activated without a nutrient source during experiments, thus the chemoattractant solution was prepared by mixing 1 part LB with 9 parts CB. The solution was supplemented with 0.41% casamino acids, the concentration that results in the optimal gradient of  $5 \times 10^{-4}$  g/ml/mm for a chemotaxis response [105].

A QS plasmid encoding GFP expression as an indicator of QS activity was constructed from BioBrick parts (iGEM Foundation, Cambridge, MA) and used to transform motile isolates of *E. coli* MG1655. The plasmid was assembled with BBa\_K546000 (encoding constitutive and feedback-controlled LuxR and LuxI expression, respectively) ligated upstream with BBa\_R0062 and BBa\_I763020 (*luxI* promoter and LVA-tagged *gfpmut3b*, respectively) in pSB1K3, a high-copy number standard plasmid backbone encoding resistance to kanamycin [124]. The full part is registered in the iGEM catalog as BBa\_J0329000. Note that the LVA tag on GFP serves as a degradation marker for the protein, decreasing its *in vivo* half-life from greater than 1 day to 40

minutes or less [125]. This was essential for both accurate quantification of the QS activation time and for repeatable experiments, as the bacteria are inevitably QS-activated when initially grown on agar plates. The rapid degradation of intracellular GFP upon the removal of AHL allowed for the majority of the population to be non-fluorescent at the start of an experiment.

The bacteria culture method was found to be critical for experiment repeatability. For all experiments, the bacteria were streaked onto a cold (4° C), 1.5% LB agar plate from a -80° C stock. The plate was incubated for 10 hr at 37° C and promptly used to inoculate liquid cultures or placed at 4° C for later use (but not kept for more than 1 day). For each experiment, a single colony was used to inoculate 10 ml of LB and shaken at 100 RPM and 37° C until the OD<sub>600</sub> reached 0.05 (about 3.5 hr). At that time, the culture was harvested by centrifugation at 1.7×g for 5 min and re-suspended (concentrating up to approximately 4×) in 1:9 LB-to-CB. Because the time to QS activation was relatively short, the final OD<sub>600</sub> of the sample was not measured until after introducing cells into the microfluidic device, thus resulting in slight variations in the starting concentration. Precise OD measurements were made by taking an average of 6 readings in an Agilent Cary 60 spectrophotometer (Agilent Technologies, Santa Clara, CA). After gently flowing the bacteria into the center channel of the device via a syringe, the inlet and outlet tubes were clamped to prevent flow. Experiments were performed at 37° C.

All data acquisition was performed using a Zeiss AxioObserver.Z1 inverted microscope equipped with a 40× objective and an MRm high-sensitivity camera (Carl Zeiss AG, Oberkochen, Germany). Images were recorded at a 2.5 min sampling interval in six locations along the length of the center channel.

In order to accurately model the spatial dependency of the QS activation time, the CPC and CMC in QS experiments were measured and used to determine kinetic parameters for the

chemotaxis model with casamino acids. CPCs and CMCs were determined from fluorescence images recorded shortly after the bacteria became fluorescent, and it was assumed that the chemotaxis response was steady throughout the experiments. Casamino acids is a mixture of a large number of amino acids, the average molar weight of casamino acids has been estimated to be about 250 Da [103]. Given the optimum mass concentration gradient of  $5 \times 10^{-4}$  g/ml/mm, its equivalent molar concentration gradient was estimated to be  $2.0 \times 10^{-3}$  M/mm. The mean CPC and CMC values measured were  $0.88 \pm 0.03$  and  $0.78 \pm 0.02$ , respectively. These values were used to fit the model for optimal values of  $\sigma C_T$  and  $K_D$  as previously described, which were determined to be 590 s and 597  $\mu$ M, respectively. These parameters resulted in a mean simulated CPC of 0.97 and mean simulated CMC of 0.78 ( $\theta_\mu = 68^\circ$ ).

The experimental QS activation time was defined in an effort to quantify the time when the rapid onset of QS-controlled gene expression began at the population-scale. To this end, a time lapse series of fluorescence images were cropped to include only a 50  $\mu$ m-wide region at the chemoattractant source wall where bacteria were densely aggregated. Likewise, simulated activation times were determined by measuring the average AHL concentration in a 50  $\mu$ m bin at the simulated chemoattractant source and using the information to solve the pair of ODEs describing GFP production and maturation (Equations 2.11 and 2.12). The average fluorescence intensity in experiments was measured by integrating over each cropped image. The data was then averaged over 4-6 imaging positions and normalized to the maximum average intensity, resulting in a single mean fluorescence curve as a function of time. The data was then analyzed to find the point when fluorescence became approximately linear in time (after increasing from the baseline). This point was identified by measuring the change in the slope  $m_i$  of a line fit through every three consecutive data points,  $x_i$ ,  $x_{i+1}$ , and  $x_{i+2}$ . The QS activation time was defined as the point in time

$t_i$  when the change in slope,  $m_i - m_{i-2}$ , first peaked (above a threshold of  $0.005 \text{ min}^{-1}$ ). In simulations, the solution to the GFP model was assumed to be proportional to the average fluorescence response of the population binned in experiments. The simulated activation time was determined by setting an absolute concentration threshold representing the assumed average concentration inside each cell in the binned region. Thus, this method of comparison between simulation and experiment depends on several key assumptions:

1. The response inside the  $50 \mu\text{m}$  bin could be regarded as homogeneous
2. A quasi-linear increase in mean fluorescence over time indicated that the majority of the population inside the bin had become fluorescent (and thus fluorescence in each cell was increasing quasi-linearly)
3. The experimental analysis approach developed allows quantitation of QS activation time in a manner that is independent of cell concentration. Thus, this approach can be used to compare results across experiments regardless of the number of cells in each bin
4. The average concentration of GFP in each cell at the activation time was the same across experiments

Assumptions 3 and 4 are of critical importance for comparing modeled results to experimental results. The rationale for Assumption 4 was based on the fact that GFP must mature inside a cell before becoming fluorescent. Based on the switch-like behavior of the QS circuit (and of the Hill function governing AHL production in Equation 2.10), it is reasonable to assume that the mature GFP concentration is increasing quasi-linearly near its maximum rate by the time enough accumulates in a cell to be detected by the sensor in the camera. Together with Assumptions 1 and 2, activation time served as a robust metric to compare simulations to experiments.

Assumption 3 was requisite in order to decouple the perceived effects of having variable numbers of fluorophores (fluorescent bacteria) between experiments from the actual onset of emergent behavior. This stipulation was the motivation for using a pseudo-derivative-based definition, as opposed to defining a simple threshold fluorescence in experiments.

Figure 3.9a shows representative normalized mean fluorescence curves vs. time for different starting concentrations ( $OD_{600}$  values shown), and Figure 3.9b shows the corresponding curves of change in slope values, with the activation times indicated by the arrows. Fluorescence and bright-field micrographs recorded at the corresponding times are shown in Figure 3.9c-e. Note that most of the bacteria inside a bin at the activation time were faintly fluorescent, as desired to determine the timeline for emergent behavior.

For a strong QS circuit with a low cell density activation threshold, such as the one employed in the validation experiments, the initial conditions relating to the feedback control of the circuit may not be zero, even after heavily diluting a population of cells. It was observed that a fraction of the cells introduced into the microfluidic device were initially fluorescent, and that this fraction correlated to an extent with activation time (*i.e.* the trend in activation time with respect to starting numbers was inconsistent if the fraction of fluorescent cells was significantly different between experiments). It was hypothesized that if these cells were producing enough GFP to be detected in fluorescence images, they were also producing LuxI above its baseline rate. We assumed the effect of this could be captured in the model by defining a simple metric,

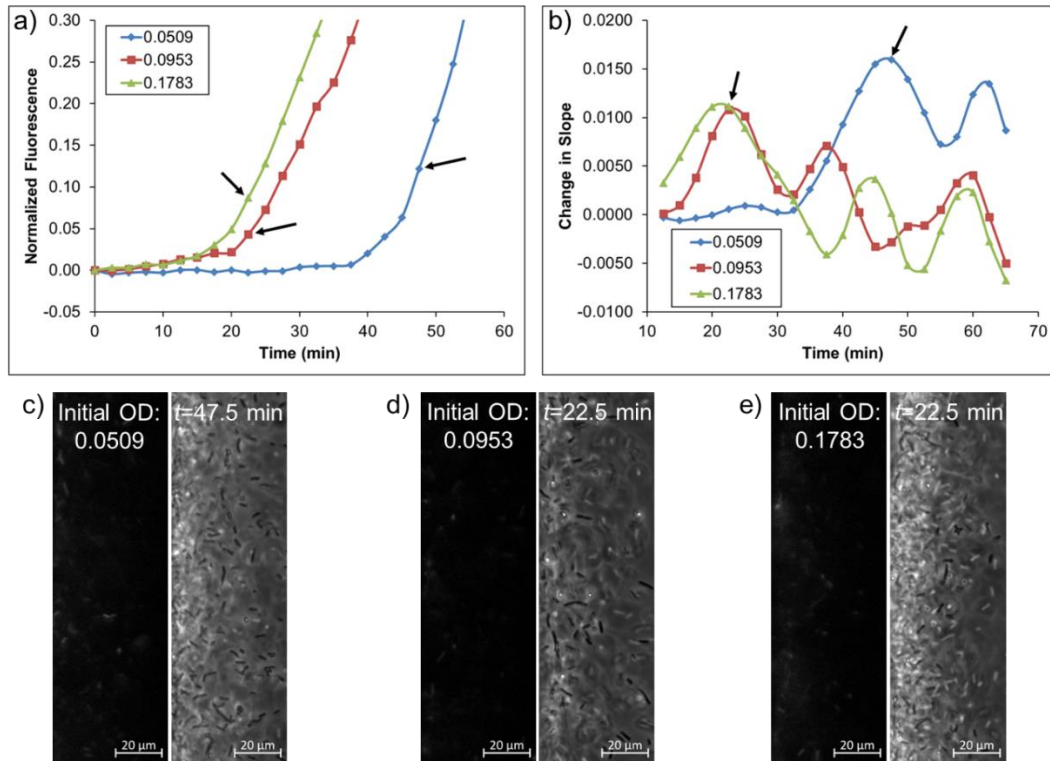


Figure 3.9: Determination of Experimental QS Activation Time. **(a)** A representative plot of normalized fluorescence intensity vs time, **(b)** the plot of change in slope through every three fluorescence data points corresponding to (a), **(c-e)** fluorescence (left) and bright-field (right) micrographs at the activation times determined in (b). The arrows on the two plots indicate activation times. Note that the images shown represent the 50 μm-wide bin in which average fluorescence data was measured.

$$Q_{IC} = \alpha\beta \quad 3.7$$

where  $Q_{IC}$  is an initial concentration of AHL inside each simulated agent,  $\alpha$  is a scaling parameter, and  $\beta$  is the number of fluorescent cells at  $t = 0$  detectable at each imaging location normalized to the initial  $OD_{600}$ . Figure 3.10 shows representative composite bright-field and fluorescent micrographs of an experiment with a relatively high (a) and relatively low (b) initial condition, as well as a plot showing both experimental activation times and the value of  $\beta$  versus the corresponding number of agents simulated (based on a unit micron thickness assumption). Note that a second-order polynomial can be well-fit to the four data points of similar, high  $\beta$  values. All data above this line has a  $\beta$  of 222 or less, while the four intersecting points had values of 275 or greater. This demonstrates the great impact that the initial condition has on results, particularly in the cases of the longest activation time at 47.5 min or for the largest corresponding initial number of agents of 66. In the former case, the activation time was delayed by 12.5 minutes when compared to the far left-most value at  $x = 8$  agents, although 50% more bacteria were present at the start. In the latter example, it took 5 min longer for activation to occur in the experiments corresponding to 66 agents versus 62 agents. Although the difference in the initial number of bacteria was only 6% in this case, the value of  $\beta$  was more than 6-fold greater in the 62 agent case.

Simulations of each experiment were run such that the physical environment of the microfluidic device were best captured. Based on the diameter of an *E. coli* bacterium being on the order of 1  $\mu\text{m}$  (bacteria harboring QS circuit were measured to have a diameter of 1.22  $\mu\text{m}$ ), it was assumed that the bacteria in the  $z$ -dimension of the microfluidic channel were homogeneously distributed and that the simulation accurately represented a unit-micron-thick section parallel to the glass surface. The number of agents used in a simulation was calculated based on this assumption,  $N_{\text{agents}} = C_{\text{cell}} * wht$ , where  $C_{\text{cell}}$  is the measured concentration of bacteria

introduced into the device,  $w$  is the width of the channel,  $h$  is the height ( $y$ -dimension) of the simulation domain, and  $t \cong 1 \mu\text{m}$  is the assumed thickness of the simulation. The simulated domain for agent movement was  $700 \times 700 \mu\text{m}^2$  based on the actual channel width, but AHL transport (Equation 2.14) was solved over the additional space between channels,  $w_s$  ( $700 \mu\text{m}$  in all QS experiments), in  $x$  on either side to account for AHL draining into the flow channels. The boundary conditions were defined as

$$\frac{\partial Q}{\partial y}\bigg|_{y=h} = \frac{\partial Q}{\partial y}\bigg|_{y=0} = 0,$$

$$D_{\text{gel}} \frac{\partial Q}{\partial x}\bigg|_{x=-w_s} = uQ(-w_s),$$

and

$$-D_{\text{gel}} \frac{\partial Q}{\partial x}\bigg|_{x=w+w_s} = uQ(w+w_s),$$

where  $D_{\text{gel}}$  is the diffusivity of AHL in the PEG-DA gel, and  $u$  is the average velocity of flow in the side channels. These conditions represent no-flux through the  $y$  boundaries since only a small portion of the length of the channel was simulated and the loss of AHL to flow in the side channels through the  $x$  boundaries. AHL diffusivity in the gel,  $D_{\text{gel}}$ , was assumed to be 72% of the value in water based on the known diffusivity of fluorescein in the gel relative to PBS [103].

The parameters  $A_1$ ,  $A_2$ ,  $Q_0$ , and  $\alpha$  were determined in a manner similar to that of chemotaxis model optimization, as described in Section 3.2.1. A differential evolution global optimization scheme was bounded by rates of AHL synthesis that were physiologically feasible. The parameters for modeling GFP were separately optimized using a least squares fitting routine to find optimal values of  $k_{tr}$ ,  $k_{G_m}$ ,  $k_{deg}$ , and  $K_m$  after a number of simulation were run to cover a large parameter space. This process was repeated in a series of iterations, wherein the optimal GFP parameters determined for each set of differential evolution solutions were incorporated into the next differential evolution search. This improved the efficiency of finding the best solution since the differential evolution algorithm stochastically determined new parameter guesses based on the error in the solution from previous guesses. The final set of optimized parameters are shown in Table 3.2. Note that many of the parameters used in the final model were taken either directly from literature or remain near estimates reported in literature after optimization. For example, the maximal rate of ClpXP-mediated degradation of LVA-tagged GFPmut3b was estimated from the reported specific activity rate of  $0.94 \text{ min}^{-1}$  and the average enzyme concentration of 100-150 nM, giving a  $k_{deg}$  of  $1.96 \text{ nM/s}$  [126], [127]. Since the actual rates are condition-dependent, the

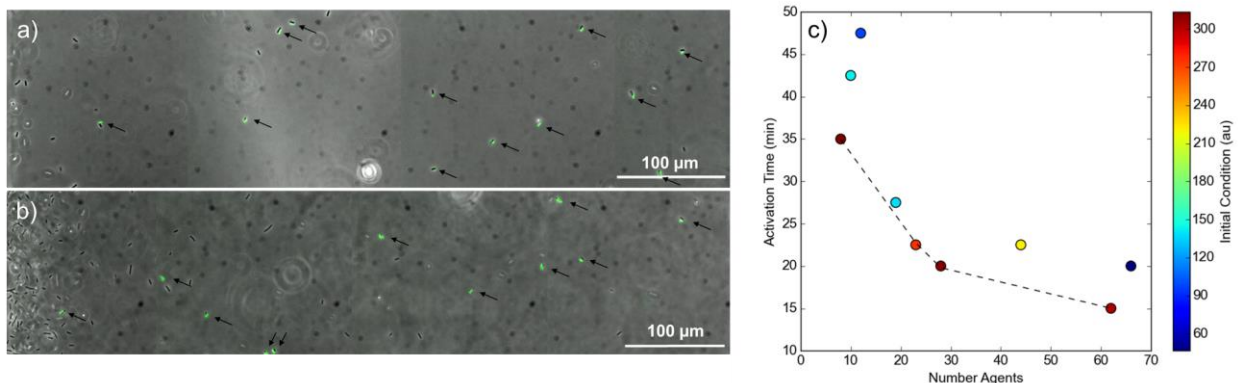


Figure 3.10: Activation Time Depends in Part on Initial Conditions. **(a)** Composite bright-field and fluorescence micrographs showing bacteria in the microchannel at  $t = 0$  with  $\beta = 313$  **(a)** and  $\beta = 47$  **(b)**, and **(c)** a scatter plot of experimental activation times and  $\beta$  values vs. the number agents corresponding to the initial  $OD_{600}$  for a unit-micron thickness assumption. Arrows on **(a)** and **(b)** mark fluorescent cells. The black dashed line in **(c)** represents a 2<sup>nd</sup> order polynomial fit of the four intersecting data points with similar  $\beta$  values.

difference found in the optimal solution (1.37 nM/s) was considered feasible. The value that are not based as closely to values from literature were considered to be more strongly dependent on specific genetic construct, strain, environmental conditions, etc.

Table 3.2: Optimal QS Parameters

Parameter	Variable	Value	Source
Basal AHL generation rate	$A_1$	3.07 molecules/s	Estimated
Upregulated AHL generation rate	$A_2$	222.3 molecules/s	Estimated
Hill coefficient	$H$	2.5	[88], [89]
Scaling parameter for initial conditions	$\alpha$	$1.33 \times 10^{-3}$ nM	Estimated
AHL Upregulation Threshold	$Q_0$	1.86 nM*	[128], [129]
Rate of GFP translation	$k_{tr}$	$4.53 \times 10^{-1}$ molecules/s	Estimated
Rate of GFP maturation	$k_{G_m}$	$2.79 \times 10^{-3}$ s <sup>-1</sup> *	[130]
Maximum rate of GFP degradation	$k_{deg}$	1.37 nM/s*	[126], [127]
Half-maximal concentration for GFP degradation	$K_m$	1620 nM*	[126]
Diffusion coefficient for AHL in PBS	$D_{AHL}$	490 $\mu\text{m}^2/\text{s}$	[131]
Diffusion coefficient for AHL in 700 Da PEG-DA	$D'_{AHL}$	353 $\mu\text{m}^2/\text{s}$	Estimated
Rate of AHL degradation	$R_d$	10.8% hr <sup>-1</sup>	[132]

\*Values that were guessed based on literature and changed by relatively small amounts to optimize the solution

Figure 3.11 shows representative spatiotemporal results from experiments and simulations (a-c) and the mean QS activation times for all nine simulation cases and experiments (d). Each set of three experiments was performed in succession on a single day (each in a new microfluidic device) with all bacteria originating from separate colonies on the same agar plate. Experiment sets were separated by several days. In each set, a low (initial OD<sub>600</sub> of ~0.05 or 12 agents), medium (OD<sub>600</sub> of ~0.10 or 25 agents), and high (OD<sub>600</sub> of ~0.20 or 49 agents) initial concentration of bacteria was used. Simulation results are presented as the mean of 10 runs using 0.01 s time step plus or minus the standard deviation. Experimental QS activation times represent a single

determination from each experiment, with an assumed uncertainty of the sampling interval (2.5 min). Each number of agents simulated corresponds to the number of bacteria introduced into the microfluidic device in a unit-micron thick  $700 \times 700 \mu\text{m}^2$  domain in  $x$  and  $y$ . The average error in simulated activation times relative to experimental results was 6.6%.

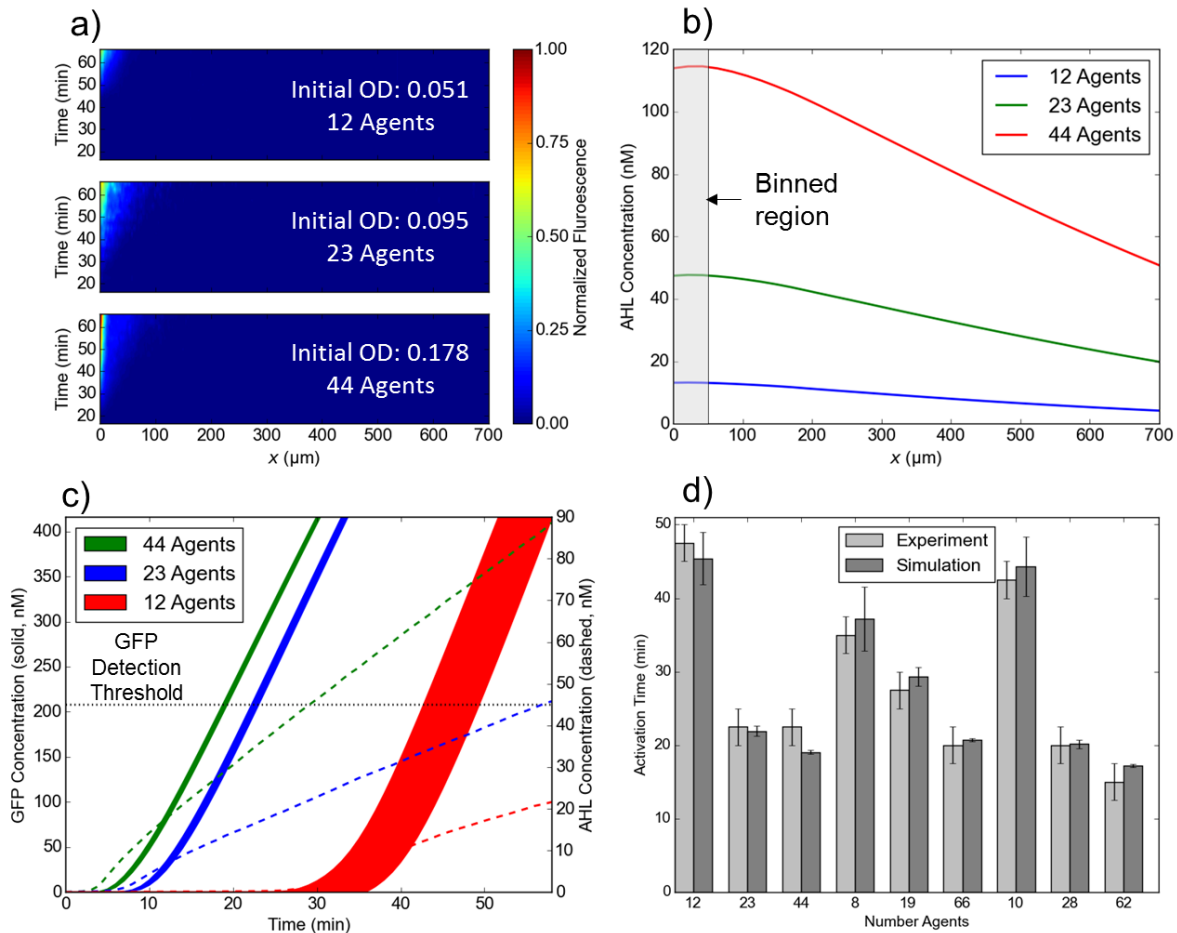


Figure 3.11: Experimental Validation of the QS Model. Nine experiments were performed at low, medium, and high starting concentrations, which were simulated accordingly. **(a)** Heat maps showing the spatiotemporal evolution of fluorescence (normalized to maximum in highest concentration case) for representative experiments, **(b)** simulated AHL profile across the channel after 44 minutes for the cases shown in (a), **(c)** simulated intracellular GFP (showing mean  $\pm$  S.D.) and mean AHL concentration (dashed lines) vs. time in the  $50 \mu\text{m}$  bin and cases shown in (b), and **(d)** all results from validation experiments and corresponding simulations. Error bars represent sampling interval for experiments or the standard deviation over 10 simulations.

### 3.4 Engineering a QS Response: Model Utility for Application-driven Design

Experimentally validating the model with a single genetic construct and defined chemotactic response provided a way to find parameters for the particular QS circuit implemented, given a set of assumptions and measurements of population dynamics (*i.e.* growth rate, chemotactic response, etc.). However, the model only holds true utility if it can be used to engineer and predict an emergent response in a complex environment and for a wide range of circuit sensitivities. In this section, the results of Section 3.3.2 are used to predict QS activation in the absence of chemical gradient, for variant circuits with tuned LuxI translation rates, and in a microbial community.

#### 3.4.1 QS Response in the Absence of a Chemical Gradient

In order to test both the sensitivity of the QS circuit to population topology and the model's ability to capture density-dependent changes in activation time, experiments were performed without the chemoeffector gradient that was used for the earlier model validation. We hypothesized that QS activation would be delayed in this case due to the lack of chemotactic migration and presence of a locally dense population. These experiments were performed in the exact manner used for

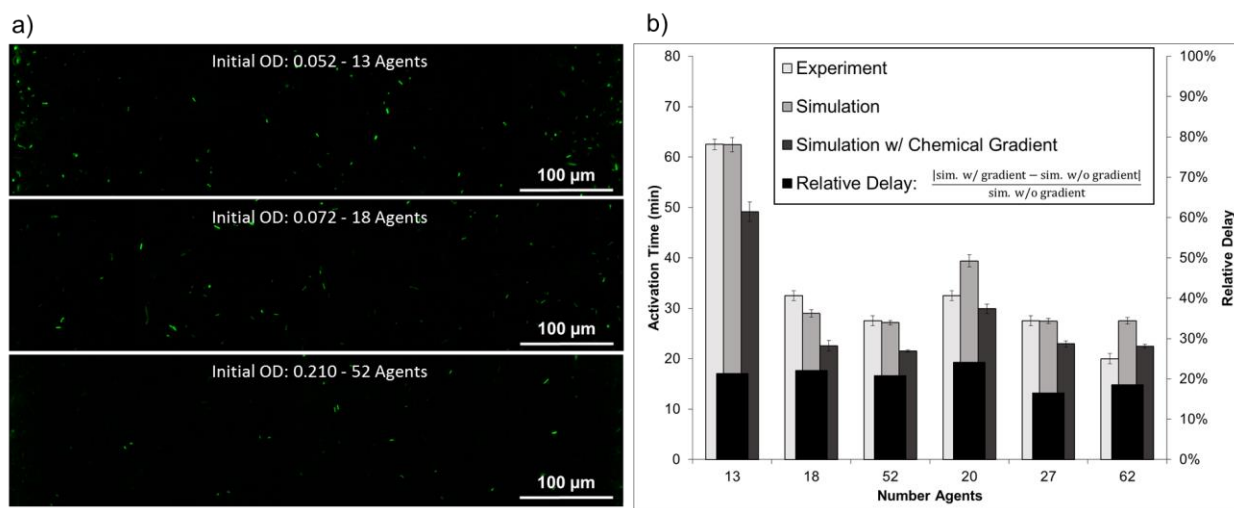


Figure 3.12: QS Activation in a Homogeneous Distribution of Bacteria. (a) Fluorescence images of the three experimental cases at activation and (b) experimental and simulated QS activation times in the absence of a chemical gradient. Also shown are simulated activation times if a  $2.0 \times 10^{-3}$  M/mm gradient of casamino acids is used to invoke a chemotaxis response and the relative differences between the predicted activation times

validation experiments, except the chemoattractant solution (0.41% casamino acids in 1:9 LB:CB) was flowed through both side channels instead of using CB alone as a buffer in one. This resulted in a pseudo-homogeneous distribution of cells until activation occurred. As in validation experiments, high, medium, and low starting density cases were tested (two of each). The results are presented in Figure 3.12, along with corresponding modeled activation times.

Using the initial condition measured at the start of each experiment, the model was also employed to predict activation times if a chemical gradient had been applied. As expected, the QS activation time was delayed relative to these predictions. Note that, while the absolute differences are only on the order of several minutes, the relative differences in activation were predicted to be up to about 20% on average for the cases tested (ranging from 16% to 24%). Coupling this with the relatively small error in modeled results without a gradient (11.8% on average; 6.8% excluding the 62 agent case) demonstrates the ability of the model to capture changes due to spatial distribution.

It should be noted that the bacteria began chemotaxing towards both PEG-DA walls near the activation time in the experiments described above. This was likely due to the generation of chemical gradients with heightened nutrient consumption as QS genes were upregulated, exacerbated by population growth. It was assumed that this did not significantly impact QS behavior since most chemotaxis took place after activation.

#### *3.4.2 QS Response in a Community of QS and QQ Bacteria*

In nature, microbes exist in heterogeneous communities that interact in a variety of ways often not captured in laboratory experiments. While some interactions are mutually beneficial and may indeed be requisite for survival, many interactions involve competition for space and resources. In practice, an engineered QS system must face such competitions and overcome them in order to

fulfill its purpose. The ability to model a community therefore is very important. Towards this end, we engineered *E. coli* MG1655 with a simple circuit encoding constitutive expression of the autoinducer inactivation enzyme AiiA, which hydrolyzes AHLs to serve as a QQ strain [100], [133].

The plasmid was constructed according to standard methods in the high-copy pSB1T3 backbone [124]. The strong synthetic promoter BBa\_J23100 and RBS BBa\_B0034 were ligated upstream of BBa\_C0160, the gene encoding AiiA (non-degradation tagged). The terminator BBa\_B0015 was placed at the end of the part, which is registered in the iGEM catalog as BBa\_J329050. Motile isolates of *E. coli* MG1655 were transformed with the resulting plasmid.

Experiments were performed in the three-channel microfluidic device described earlier. For each experiment, QS bacteria were cultured and harvested as previously described, while AiiA-expressing strain was cultured by diluting a stationary-phase culture to 0.1-0.2% in 10 ml of LB supplemented with 15 µg/ml oxytetracycline. The QQ bacteria were harvested at an OD<sub>600</sub> between 0.26 and 0.59. Since the cultures were seeded with a relatively small number of cells (starting of OD<sub>600</sub> of approximately 0.001) and since the range of harvesting densities is well within the limits of exponential growth, it was assumed that the amount of AiiA inside each cell and the expression rates were constant between experiments.

A series of experiments were performed at various ratios of QQ-to-QS bacteria in order to determine how the presence of the quenching strain affected the activation time of the QS strain. Each was performed in a manner similar to that of the validation experiments, with the only difference being that the two strains were mixed prior to being flowed into the center channel of the microfluidic device. The starting OD<sub>600</sub> for the QS strain was kept constant at approximately 0.05 across experiments. Following the experiments, the AiiA model described in Section 2.4 was

fit to the results in order to find the best constitutive AiiA production rate  $k_A$  and the initial concentration of AiiA inside each cell  $A_{init}$  in the same way that the QS model was fit to the validation experiments. Figure 3.13 shows the experimental and simulated results of the eight experiments performed, including the activation times in the presence of the QQ strain, the IC of the QS strain, and the predicted activation time if no QQ cells were present.

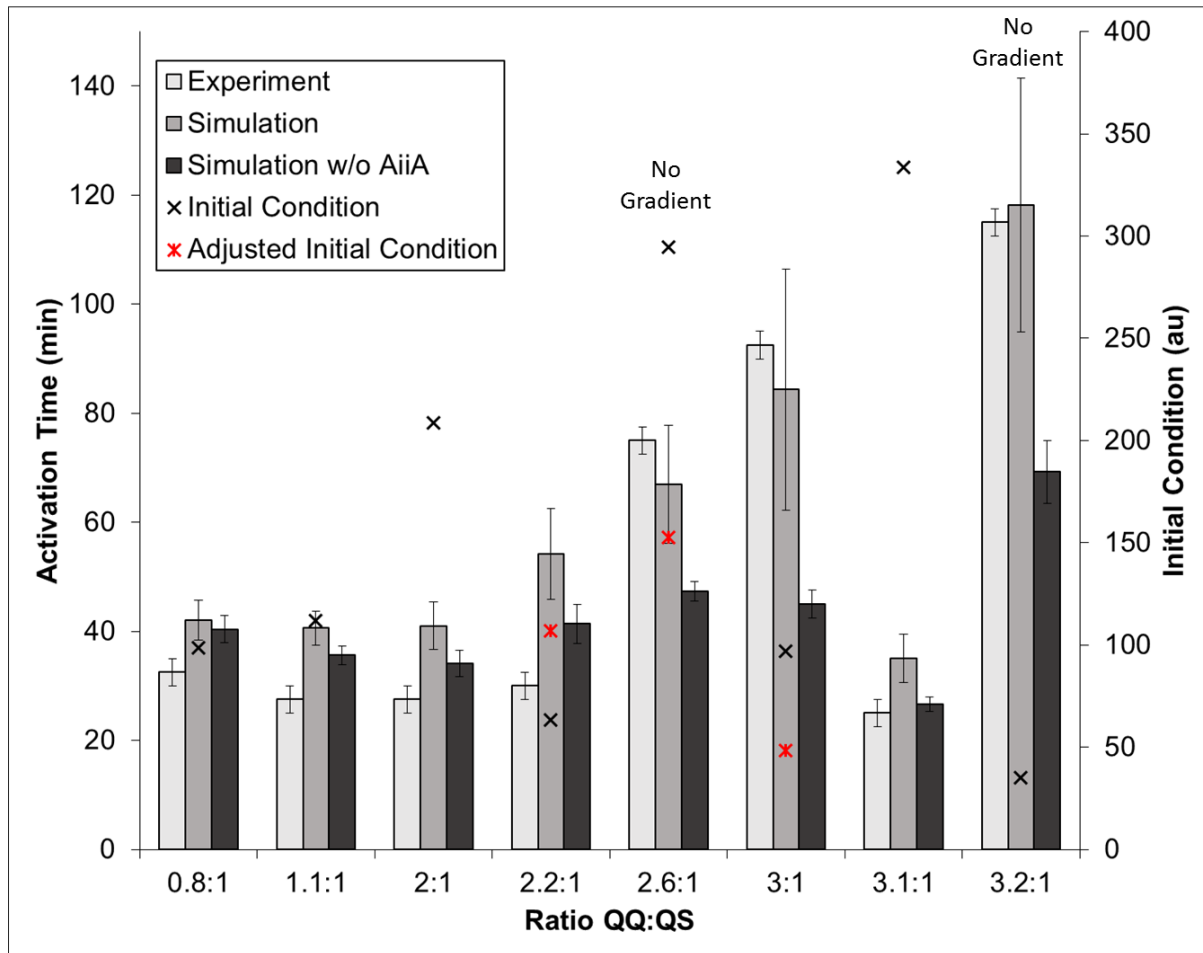


Figure 3.13: Experimental and Simulation Results for Mixed QQ and QS Bacterial Communities. Error bars on simulation results indicate the standard deviation ( $n=33$  for results w/ AiiA;  $n=10$  for results w/o AiiA). Note that the QS initial condition for the 2.2:1, the 2.6:1, and the 3.0:1 cases were adjusted by raising and lowering their ICs by their respective standard deviations (shown by red cross marks). The text “No Gradient” above a set of results indicates that chemoattractant solution was flowed through both side channels of the microfluidic device.

The results shown in Figure 3.13 show good agreement between simulations and experiment for experiments in the microbial community. However, it is important to note the sensitivity of the results to the QS IC. For instance, the QQ cells in the 3.1:1 case did not appear to have an effect on activation time of QS bacteria with an IC of almost 350 au. In contrast, a large delay was observed in the 3.0:1 case, where the QS IC was only around 100 au. The presence of a chemical gradient facilitating chemotaxis-based localization may have also been a significant factor, as a delay was observed in the 2.6:1 case, although the QS IC was relatively high. Also, a significantly greater relative delay occurred when no gradient was used for a ratio of about 3:1 (compare 3.0:1 and 3.2:1 cases). The parameters used in the AiiA model, including enzymatic parameters derived from literature and the protein dynamic parameters fit to experimental data are shown in Table 3.2.

Table 3.2: Parameters Used in the AiiA Model

Parameter	Variable	Value	Source
Michaelis-Menten Constant	$K_A$	1.0 mM*	[133]
Catalytic Constant	$k_{\text{cat}}$	22.68 s <sup>-1</sup>	[133]
AiiA Degradation	$k_{A,\text{deg}}$	0.1% hr <sup>-1</sup>	
Constitutive Rate of AiiA Production	$k_A$	105.7 molecules/s	
Initial Concentration of AiiA	$A_{\text{init}}$	125 μM	

\*Values that were guessed based on literature and changed by small amounts to optimize the solution

The IC parameter, which is measured by averaging the number of initially-fluorescent cells in four imaging locations and dividing the value by the initial OD<sub>600</sub>, in general had a relatively large amount of standard deviation (about 50% average for the 8 experiments). While using its average value alone gave a relatively good model fit for experiments with QS bacteria only, errors may have been exacerbated in community experiments. It is thought that the primary reason for

this is that, relative to the activation time, the community experiments took a significantly larger amount of time to prepare prior to the start of imaging. That is, it was estimated that there was approximately an additional 4-5 minutes between the time the bacteria were harvested from a culture flask and the time that imaging began. This reasoning may explain the general overestimation of the activation time for the results presented in Figure 3.13. Additionally, the average relative standard deviation of the IC in the nine QS validation experiments was much lower (approximately 20%). This can be attributed to the fact that a low concentration of QS bacteria was used in each of the quenching experiments, whereas the  $OD_{600}$  in the earlier set of experiments was greater than 0.05 in 6 of the 9 cases. Because of this, the QS ICs for the 2.2:1, 2.6:1, and 3.0:1 cases were adjusted by their respective standard deviations in order to provide a better model fit (indicated by red markers in Figure 3.13).

Figure 3.14 shows the characteristic behavior of the AiiA model, which is a direct result of the values of the fit initial concentration and production rate. Interestingly, it was found that the initial concentration is relatively high but decreases over time due to growth. This result makes intuitive sense because the bacteria are removed from an exponential-phase culture, wherein recombinant protein production should be highest, and kept at room temperature for close to 10 minutes before being inserted into the microfluidic device. This postulate is also consistent with the observation that growth rate was observed to be very high early in experiments but slows over time (evidenced by the linear increase in relative population size).

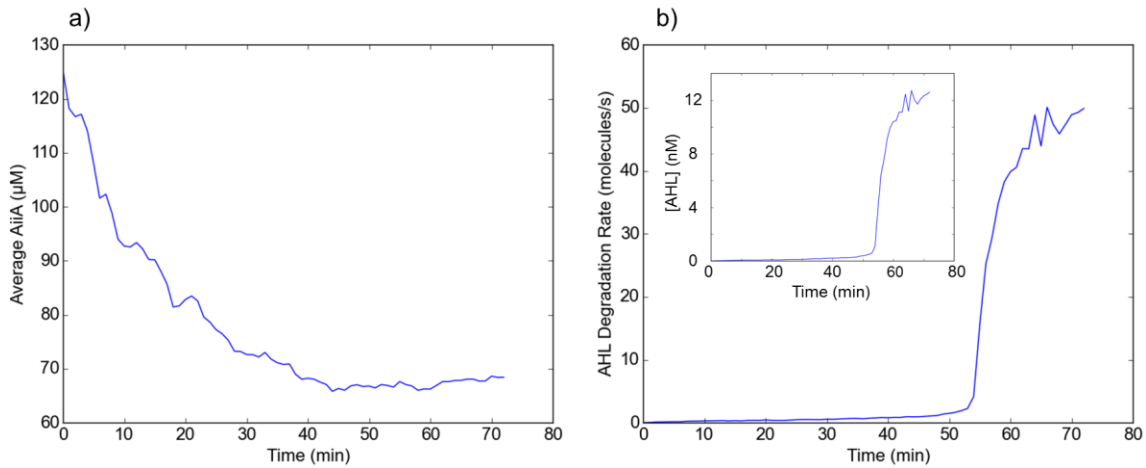


Figure 3.14: AiiA Protein Dynamics and Enzymatic Degradation of AHL. **(a)** The average concentration of AiiA inside the population of agents as a function of time and **(b)** the average rate of AHL degradation by AiiA in the 50  $\mu\text{m}$  binned region versus time. The inset in (b) shows the average concentration of AHL in the binned region.

Figure 3.15 shows representative micrographs from quenching experiments and corresponding simulations. Note that the two populations appear homogeneously mixed within the biased distributions due to chemotaxis.

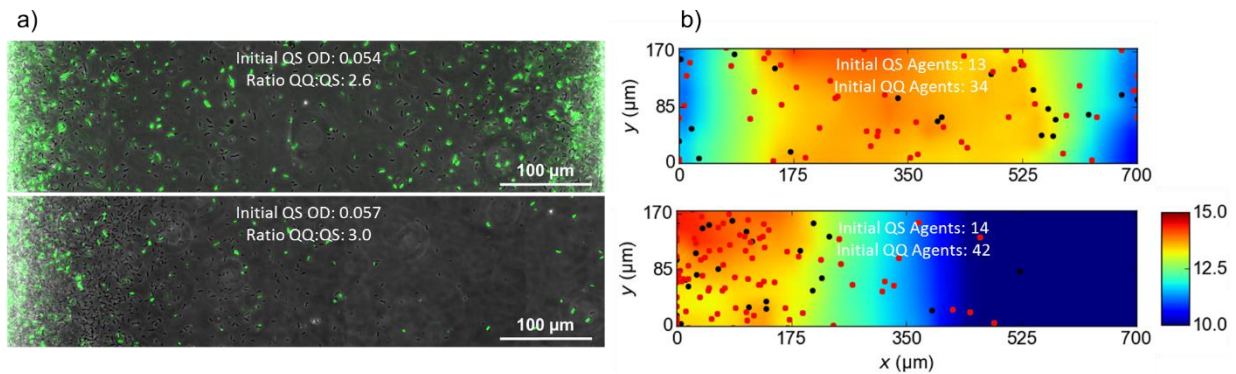


Figure 3.15: Representative Images of QS-QQ Experiments and Simulations. **(a)** Superimposed bright-field and fluorescence micrographs after QS activation for a case with no chemoattractant concentration gradient (top) and with a gradient (bottom) and **(b)** corresponding simulations (QS agents are represented by black points and QQ agents by red ones).

An additional observation of simulation results is the relatively large standard deviation in the 3.0:1 and 3.2:1 cases. This was found to be caused by the stochastic population dynamics of

the two strains. Specifically, the model captured pseudo-random fitness advantages of one strain over the other as variations in the mean activation time. Figure 3.16 shows plots of the relative population size for each of the two populations (QQ and QS) for the 3.0:1 case and the corresponding activation times for 6 independent simulations. Both are modeled with same average growth rate, but actual division events are chosen stochastically. It can be noted that divergence between the relative size of the two populations typically occurs after ~40 min. This is thought to be the reason for low standard deviations in shorter simulations. Additionally, it should be noted that there was less variability in the QQ fitness than in the QS fitness. This is likely due to QQ population being ~3 times larger in these cases, meaning that random fluctuations in growth rate are damped out over the population.

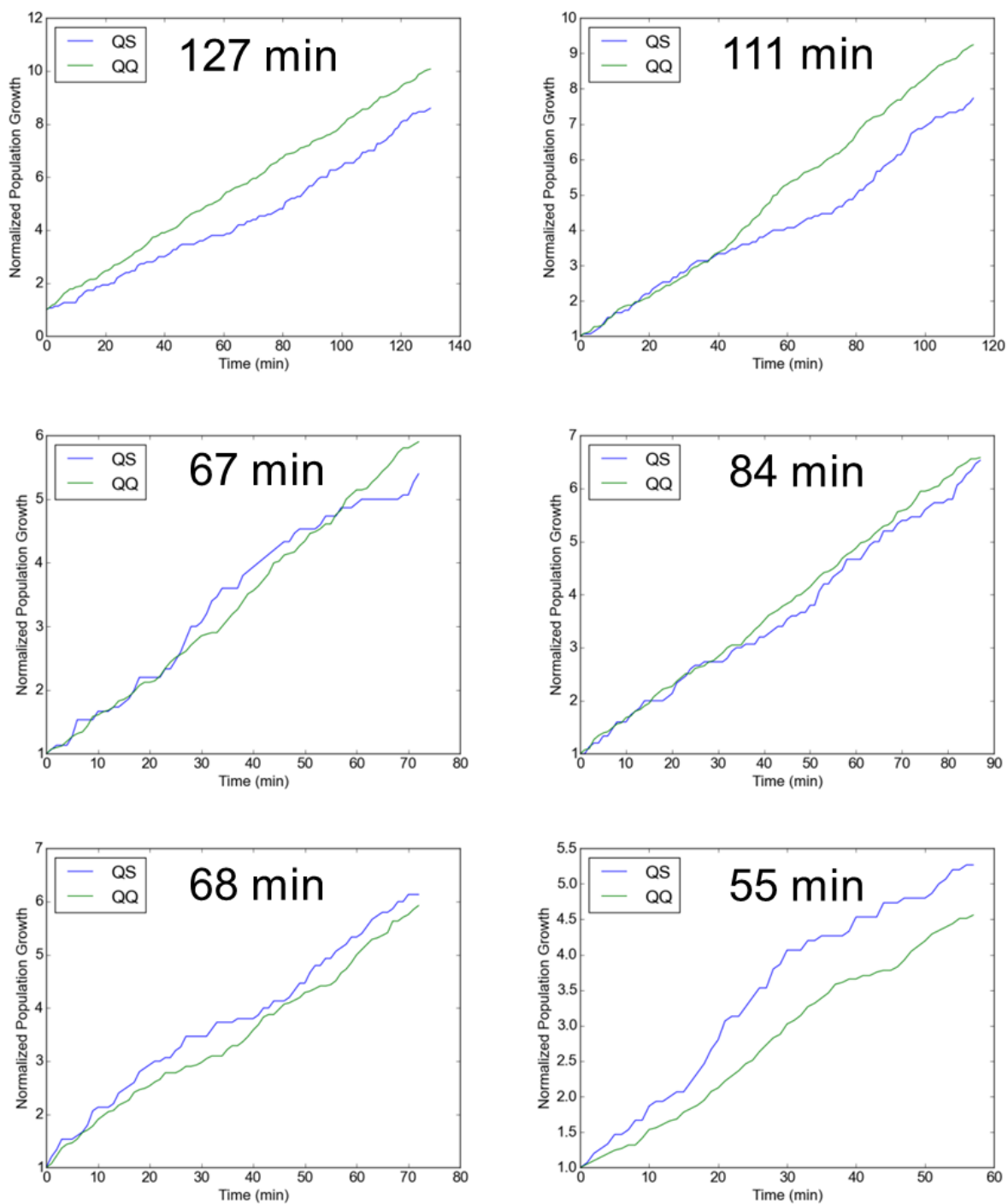


Figure 3.16: Population Dynamics in 6 Simulations of the 3.0:1 Scenario for QS and QQ Strains. The text on each plot indicates the activation time for that simulation.

Note from Figure 3.16 that the simulations that predicted an activation time closest to the experimental result were those in which the fitness was most similar between the two strains. This was also true in the 3.2:1 case, in which the standard deviation was also high. Figure 3.17 shows the relative population sizes versus time for one of the most accurate individual results (simulated activation time of 107 min compared to an experimental result of 112.5 min), wherein two strains exhibited a similar trend in growth.

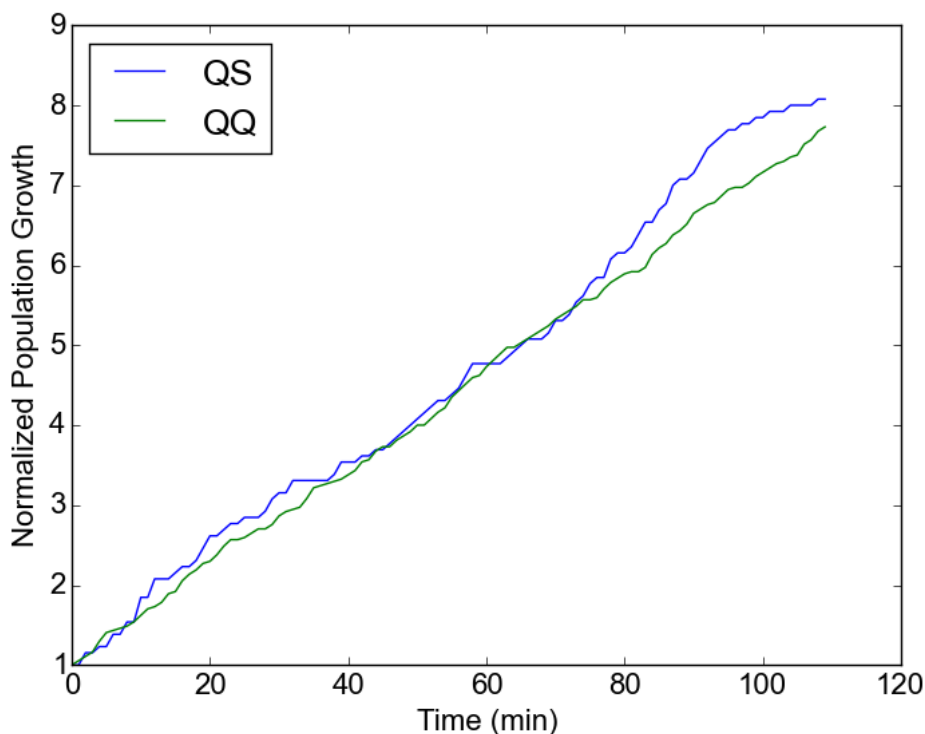


Figure 3.17: Relative Population Size versus Time for a Simulation of the 3.2:1 Case (simulated activation time of 107 min; experimental activation time of 112.5 min)

### 3.4.3 Designing and Modeling QS Constructs with Altered Sensitivity

The QS circuit employed for the experiments detailed in Sections 3.2 and 3.3.1 is extremely sensitive to AHL (*i.e.* it is switched into its up-regulated state at low threshold population densities) and may not be appropriate for downstream applications. For engineering purposes, such as

building biosensing strains, environmental toxin remediation systems, or for biomedical function, it is critical that the construct be tunable. The model presented herein should therefore be capable of robust predictions of QS activation given a set of tuned parameters. This ability was tested by using the freely-available RBS Calculator (v2.0, <https://salislab.net/software/>) to design synthetic ribosomal binding sites (RBSs) to be placed upstream of *luxI* in order to modulate its rate of translation [134], [135]. In bacteria, the RBS functions is in part to initiate protein translation based on molecular interactions with the 16S rRNA [134]. This translation initiation rate (TIR) is a major factor in determining the amount of a particular protein that is expressed and can be tuned using thermodynamic models [134].

Towards the future application of making rational system design decisions based on model predictions, two synthetic RBSs with TIRs of 24 au and 99 au (arbitrary units) were designed and registered in the iGEM catalog as BBa\_J329999 and BBa\_J329998, respectively. These design TIRs were chosen in order to produce circuits that are significantly less sensitive to cell density than the one utilized for validation experiments, which uses an RBS with a predicted TIR of 1262 au (BBa\_B0034) to initiate LuxI translation. Primers containing the sequences were synthesized (Integrated DNA Technologies, Coralville, IA) and used to perform substitutions in BioBrick part BBa\_K546000 via site-directed mutagenesis (Thermo Fisher Scientific, Waltham, MA), replacing the existing RBS BBa\_B0034. The resulting parts were ligated upstream of BBa\_I763020 and inserted into the high-copy plasmid backbone pSB1T3. Additionally, a second variant of each construct was made by adding an additional copy of the LuxI expression sequence (BBa\_R0062, BBa\_J329999 or BBa\_J329998, BBa\_C0061, BBa\_B0015) to the part and inserting it into the backbone pSB1C3. Thus, two variant constructs expressing a single copy or double copies of *luxI* (denoted *sluxI* and *dluxI*, respectively) were made with each RBS. Note that all three

plasmid backbones used in experiments contain the same origin of replication (pMB1) and are similar in copy number.

Microfluidic experiments with the alternative constructs were performed according to the experimental procedures previously described (with a chemoattractant gradient). For the 99 au RBS, the activation times were 205 min and 270 min for the *sluxI* and *dluxI* constructs, respectively (starting OD<sub>600</sub> of 0.10). The 24 au, *dluxI* construct was activated in 255 min at an initial OD<sub>600</sub> of 0.15.

Since the rate of protein expression scales linearly with TIR, it was assumed that the model could be adjusted to account for alternative RBSs by scaling  $A_1$  and  $A_2$  (basal and upregulated rates of AHL production, respectively) accordingly. That is, a scaling factor was defined as  $\eta_{\text{RBS}} = R_{\text{RBS}}/R_{\text{B0034}}$  where  $R_{\text{RBS}}$  is the TIR of the alternative RBS and  $R_{\text{B0034}} = 1262$  au is the TIR of the RBS used in the plasmid constructs for QS validation experiments and model fitting. To account for the additional copy of the *luxI* gene in the *dluxI* constructs, the basal generation term  $A_1$  was multiplied by the number of copies of *luxI* in the construct,  $n_{\text{luxI}}$  ( $n_{\text{luxI}} = 1$  or  $2$ ). This method of accounting for the changes in gene expression behavior was based on the premise that the Hill term (second term) of Equation 2.10 represents the dynamic (switch-like) behavior of the circuit, which fundamentally does not change with the number of gene copies. This is because the maximum rate of new LuxI production (and AHL production) is limited by translation (*i.e.* the probability of ribosome association, which is indicated by the TIR value). In contrast, the basal generation rate stems from low, unsaturated LuxI production. This production is nevertheless reduced relative to constitutive production in the reference construct (BBa\_B0034 RBS), but can be assumed proportional to the number of gene copies. The scaled rate of AHL production is then

$$A_t = n_{luxI} \eta_{RBS} A_1 + \eta_{RBS} A_2 \frac{Q^H}{Q^H + Q_0^H} \quad 3.8$$

The results of experiments and corresponding simulations are shown in Figure 3.18. Using the nominal TIRs for scaling resulted in relatively low error between simulated and experimental activation times considering the factor of 2.3 uncertainty in TIR predictions. Moreover, TIRs did not require large adjustment to provide optimal fits of the data (24 au increased by 60% to 38.4 and 99 au reduced by 10% to 89 au). While more designs should be considered, these results show that the model can be combined with thermodynamic predictions of translation to provide a design tool for synthetic biology.

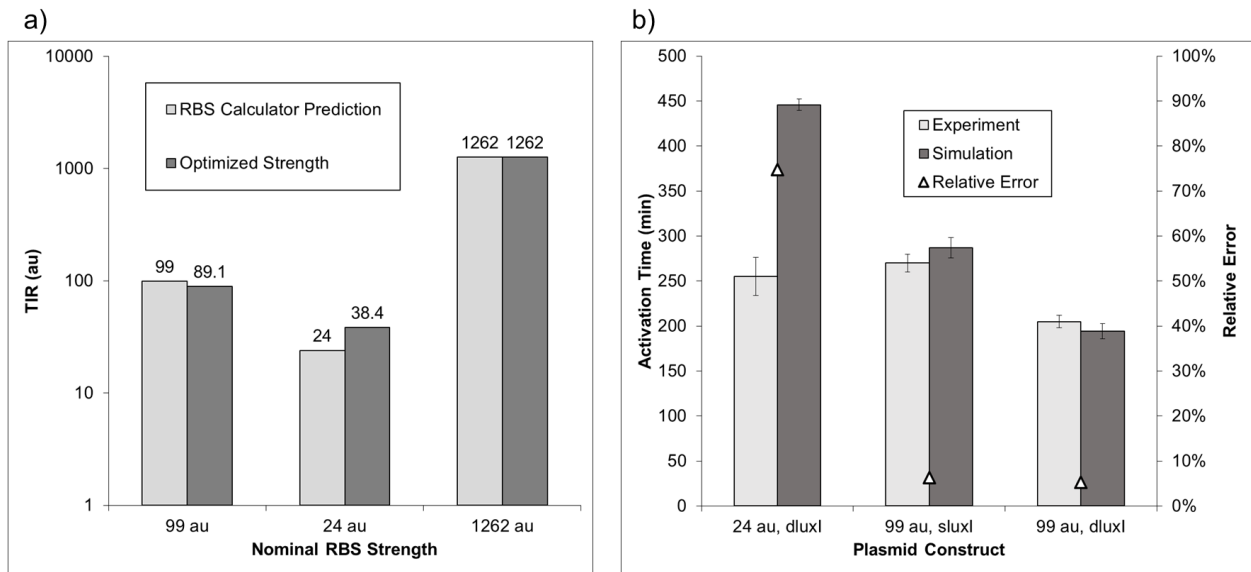


Figure 3.18: Application of the Model as a Genetic Design Tool for Synthetic Biology. (a) The RBS Calculator-predicted RBS TIR values, and the optimized values found to produce accurate activation time predictions, and (b) experimental and simulated activation times using the RBS Calculator-predicted TIR values for scaling  $A_1$  and  $A_2$ . Results for the two *dluxI* constructs represent the mean  $\pm$  standard deviation for two independent experiments. The 99 au, *sluxI* results represents a single experiment.

## **Chapter IV Discussion of Results and Future Work**

Given relative RBS strength, growth rate, and initial bacterial numbers, and chemo-effector concentration gradient information, the model developed in this work can provide an estimate of the amount of time required for a genetic “switch” to be flipped in a QS population, leading to a high rate of expression of proteins of interest. This capability could be of great benefit to a number of bacteria-based technologies, including toxin remediation, biosensing, and disease treatment or prevention. It also provides an insightful and computationally efficient approach to study of microbial communities in variety of settings including the human microbiome. In this concluding chapter, we discuss some of the insights gained through work that will prove beneficial in future genetic circuit design and highlight some of the future work planned towards model refinement and utilization.

### **4.1 Discussion**

The model developed in this thesis is unique in its scalability and computational efficiency as an agent-based model. This was made possible through a number of simplifying assumptions that were justified based on the population-scale metrics of interest such as CMC and QS activation time. Specifically, the assumptions that a bacterial population can be modeled in two-dimensions as a unit micron-thick slab and that complex flow fields (*i.e.* advection) may be neglected when solving chemical species transport provides the greatest reduction in computational time relative to a non-simplified model. The first assumption should be a good approximation of population-averaged behavior given that the simulation represents a relatively thick domain, such as the 100  $\mu\text{m}$ -thick microfluidic channel in which experiments were performed. Direct experimental evidence was presented in support of the latter assumption. The model was also simplified with respect to intracellular signaling and protein dynamics. This was considered a particularly good

choice for chemotaxis modeling, as bacterial run time have been demonstrated to be well-approximated as a logarithmic function of chemoattractant-receptor binding [72], [73]. The QS circuit dynamics were represented using a single Hill function, which can be considered a lumped model capturing AHL-controlled transcription of *luxI*, translation to the LuxI protein, and AHL synthesis by mature LuxI. While this too improves computation time, a noteworthy consequence is the inability to simulate noisy circuit dynamics and stochastic AHL production on an individual basis. With respect to physical cell-cell interactions, accounting for volume exclusion and cell reorientation during collision events should well-approximate relatively dense populations of (1 agent/mm<sup>2</sup> is a simulation translates to 10<sup>6</sup> cell/ml in experiment), where such events occur regularly.

Despite the model's simplicity, its ability to give accurate, quantitative insight was evidenced by its fit to chemotactic behavior for L-aspartic acid concentration gradients spanning three orders of magnitude and QS-based GFP expression for nine experiments of different starting cell densities and initial conditions. Further, using the fit parameters and making appropriate assumptions to scale rates of AHL production resulted in well-predicted QS activation times for three relatively much weaker synthetic constructs. Such scalability provides confidence in extrapolating predictions, while the model's efficiency could make it a valuable design tool capable of optimizing a large number of tunable variables in a short amount of time. The agent-based framework is easily adaptable to future models where individual genetic circuits are simulated to better estimate heterogeneities in a population.

To demonstrate how the model may be used in bacteria-based system design, the QS activation time was predicted as a function of both RBS strength and growth rate. In practice, RBSs of a desired strength can be deterministically designed using the thermodynamic model described

in [135], while growth rate, chemotaxis, and potentially quorum quenching will primarily be a function of the environment in which the bacteria-based system will be utilized. The simulations were run using the same geometry, boundary conditions, and chemical gradient as in simulations of microfluidic experiments, and each contained an initial population of 25 agents. The results are shown in Figure 4.1.

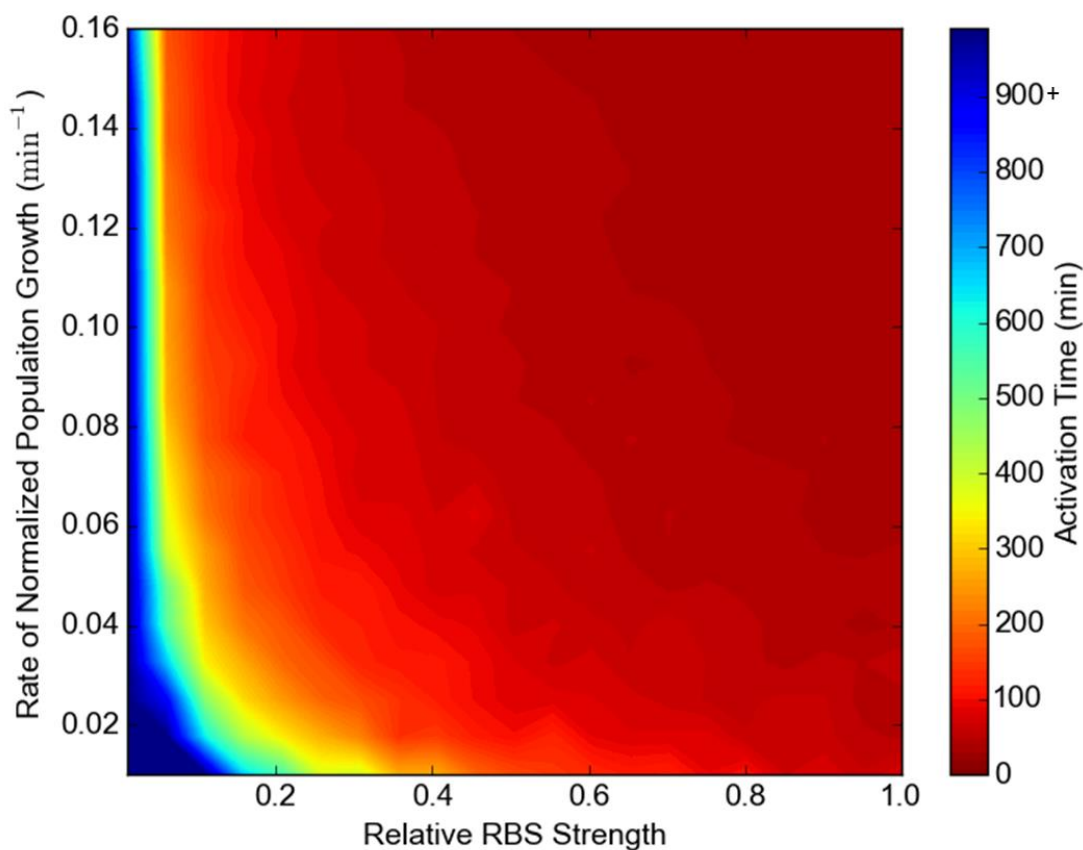


Figure 4.1: Activation Time as a Function of Normalized Population Growth Rate ( $dP^*/dt$ ) and RBS Strength Relative to BBa\_B0034

Note the robustness of the QS activation time predicted in Figure 4.1. The time required for activation is less than 100 min for RBSs TIRs greater than about 0.6 relative to BioBrick part BBa\_B0034 (1262 au) for any growth rate greater than  $0.02 \text{ min}^{-1}$ . Moreover, 93% of the entire

parameter space shown gave an activation time of less than 500 min. Only very weak RBSs (TIR less than 0.16) results in activation times that were greater than 900 min.

Towards the rational and application-driven design of bacteria-based systems, a scenario with two small point-like sources of chemoattractant located at  $x_1 = 900 \mu\text{m}$ ,  $y_1 = 900 \mu\text{m}$  and  $x_2 = 1200 \mu\text{m}$  and  $y_2 = 1200 \mu\text{m}$  in a  $2400 \times 2400 \mu\text{m}^2$  domain was considered with zero-concentration boundary conditions. The diffusion of the chemical from the sources was

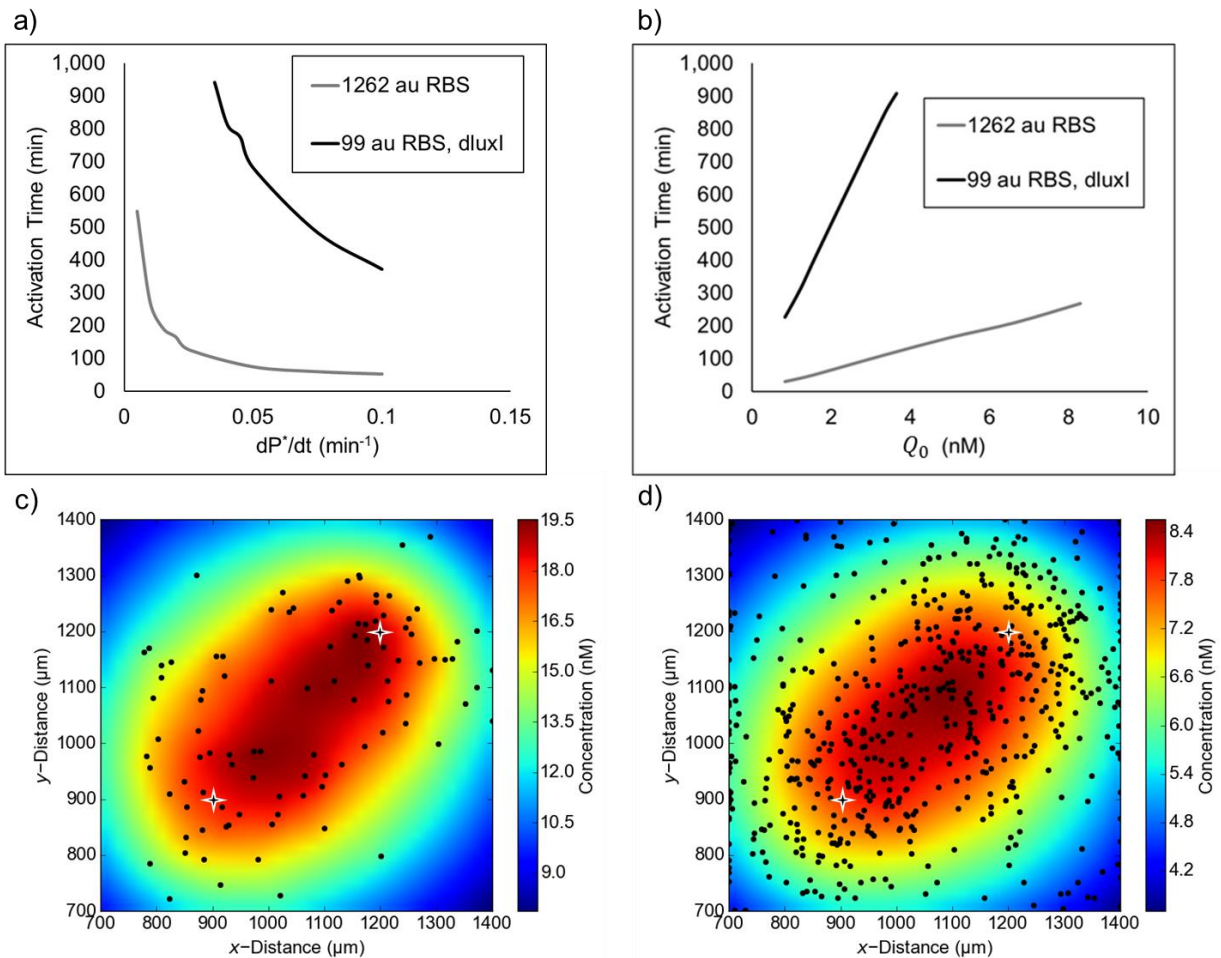


Figure 4.2: The Effects of Growth Rate **(a)** and Up-regulation Threshold  $Q_0$  **(b)** on Activation Time. Also shown are AHL concentrations and bacterial distributions at activation for representative simulations using  $Q_0 = 1.7 \text{ nM}$  (approximate fit value from experiments) using the **(c)** 1262 au RBS and the **(d)** 99 au RBS with double copies of *luxI*. The locations of the chemoattractant sources in (c) and (d) are indicated by the star symbols. Note that the full domain size in (c) and (d) is  $2400 \times 2400 \mu\text{m}^2$ , but only a subset is shown.

approximated using the analytical solution developed by Futrelle and Berg [136] for a finite amount of a chemical diffusing from the end of a capillary tube. Such a scenario could represent bacteria colonizing a small piece of semi-solid matter in the environment or a piece of tissue in the human body where AHL would be drained by surrounding fluid flow and chemical gradients attracting bacteria are transient. Simulations were performed to elucidate the effects of growth rate and up-regulation threshold  $Q_0$  on the QS behavior, showing in Figures 4.2a and 4.2b, respectively.

It is interesting to note how constructs of different RBS strengths are affected differently by changes in growth rate or upregulation threshold. For a relatively strong RBS (1262 au), the activation time was not strongly impacted for the wide range of normalized population growth rates between about  $0.05 \text{ min}^{-1}$  and  $0.1 \text{ min}^{-1}$  (Figure 4.2a). The activation time for this RBS was strongly affected at near-zero growth rates, asymptotically approaching infinity as  $dP^*/dt \rightarrow 0$ . In contrast, the weaker construct was sensitive to growth rate throughout the range of values tested. In theory, any  $dP^*/dt > 0$  would eventually become activated, though simulations were cut off after 1000 min. For a single growth rate of  $0.07 \text{ min}^{-1}$ , the slope of activation time versus RBS strength was much steeper when agents with the weaker RBS were used, compared to those with a stronger one (Figure 4.2b). Changing the threshold in practice could be accomplished by altering the transcriptional activation characteristics of LuxR-AHL by altering the strength of the *luxI* promoter, engineering synthetic promoters, or by changing the specificity of LuxR for AHL [137]–[140]. The linear trend demonstrated here could be exploited for system design by engineering a synthetic promoter and estimating  $Q_0$  from a simple sensitivity assay using exogenous AHL. Combined with the appropriate RBS choice from simulation results, the activation time of the system could be tuned with relatively low uncertainty.

Also interesting to note are the differences in AHL concentrations at the time when activation occurred between the agents with a strong 1262 au RBS (55 min) and those with the much weaker construct utilizing a 99 au RBS with two copies of *luxI* (408 min). Despite the greater number of agents in the latter case, the AHL concentrations at activation were much higher in the case of a stronger RBS. The dynamics of mature GFP expression was the limiting factor in this case; AHL accumulated so quickly in the environment when the stronger RBS was used that the agents did not become activated until well after the up-regulation threshold of AHL had been surpassed. This also demonstrates that the robustness of QS activation shown in Figure 4.1.

Examples of the applications of bacteria using QS-based genetic circuits are prevalent throughout literature, including recent examples of bacteria-based therapeutic systems for cancer treatment. Notably Swofford *et al.* [87] engineered attenuated *Salmonella* Typhimurium VNP20010 with a plasmid to promote the expression of  $\alpha$ -hemolysin from *Staphylococcus aureus* to help destroy cancer tissue only upon colonization at a high density. The working principle of the system was centered on the strain's preference for tumor tissue over healthy tissue, thereby precluding colonization outside of tumors. In another recent study, Din *et al.* [141] engineered a "synchronized lysis circuit," in which a bacteriophage protein causing bacterial cell lysis was expressed upon QS activation. Additionally, the authors incorporated the gene for a Haemolysin E, a protein that can lyse tumor cells, into the circuit. Upon activation, the bacteria therefore released the cytotoxic protein into their immediate environment due to the disintegration of their own cell wall. This bacterial suicide also resulted in a form of negative feedback for the QS circuit, since a relatively small number of bacteria survived the emergent event. Those remaining then began to proliferate and the cycle repeated. Studies such as these are exciting demonstrations of the possible applications of QS and bacteria in emerging biotechnologies. In principle, any gene

that can be expressed by a bacterium could be placed under the control of a QS promoter so that a protein of interest is expressed under the correct conditions.

To investigate QS-based drug delivery in solid tumors, a series of pilot experiments were performed using HCT-116 multicellular tumor spheroids (an *in vitro* tumor model), and *Salmonella* Typhimurium VNP20009 engineered to constitutively express a red fluorescence protein (RFP) in addition to the same 99 au RBS QS circuit utilized elsewhere in this thesis. Figure 4.3 shows representative composite bright-field, red, and green fluorescence images of a tumor slice. Areas of red indicate the presence of bacteria, while green indicates QS activation. GFP was detected in the densely colonized regions. Such a result is promising, since QS activation and production of a drug or cytotoxin outside of the tumor would cause damage to healthy tissue *in vivo*. The model could be used in the future to predict optimal QS parameters that would preclude QS activation outside of the tumor (where the population density is lower).

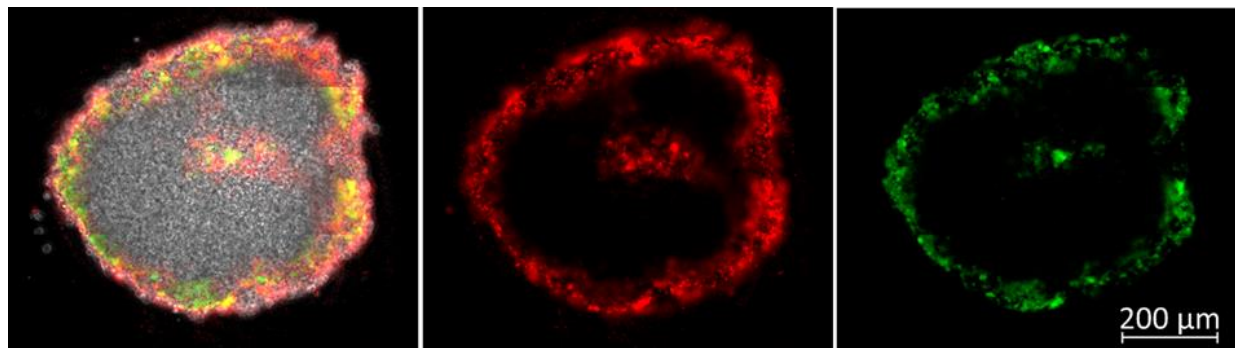


Figure 4.3: HCT-116 Tumor Spheroid Colonized with QS *Salmonella* Typhimurium VNP20009 Expressing GFP as an Indicator of QS Activation while Constitutively Expressing RFP. This sample was fixed after 12 hr of incubation.

## 4.2 Future Work

The model developed in this thesis demonstrated that emergent behavior in a QS bacterial population, which is fundamentally based on complex, non-linear dynamics, can be accurately predicted in an efficient computational framework based on justified simplifying assumptions.

Nevertheless, much work lies ahead to extend the capabilities of the model to capture behavior in more complex environments and in order to capture intracellular processes at greater resolution (*i.e.* individual gene regulation, transcription, and translation). Specifically, the model will be used towards the design of optimized bacteria-based tumor treatment strategies.

Currently, the model can only truly be used to model fluidic environments, such as the microfluidic channel in which experiments were performed. Future work will involve implementation of growth, migration, and colonization in tissue, such as the tumor spheroids pictured in Figure 4.3. This work will involve great modifications to the model, as normal run-and-tumble behavior no longer takes place and bacteria, in part, use cell invasion mechanisms to translocate in tissue. It should be noted however that the existence (or lack) of bacterial chemotaxis (which implies swimming motility) in tissue is disputed in literature [142]–[144]. The extension of the model to include emergent behavior in tissue will be hugely beneficial in designing bacteria-based cancer therapy systems.

Additionally, the model will be refined by replacing the Hill function describing AHL production with a set of delay differential equations (DDEs) to model mRNA transcription and protein translation, accumulation, function, and degradation. This will make the model more robust and applicable to variant and more complex genetic circuits. For instance, multiple QS circuits, each utilizing a unique signal, could be employed to control the timing and rate of expression of multiple proteins of interest. Substrate utilization and kinetics will also be modeled, which will prove very important for simulating growth and protein expression in the tumor microenvironment. The model may also be extended to three dimensions, which could be particularly useful for modeling bacterial colonization of tissue. However, while these additions will greatly expand the model's capabilities, computational expense will inevitably increase. For instance, a three-

dimensional model will have a factor of  $n$  more nodes than its corresponding two-dimensional simulation (where  $n$  is the number of nodes along any edge of the mesh), which will increase both the number of computations required at each time step as well as the memory requirements. Tradeoffs between resolution (both spatial accuracy and accuracy at the single-cell level) and computational time will be assessed and implemented according to the needs of specific problems in order to minimize computational requirements.

## References

- [1] G. Pandey and R. K. Jain, "Bacterial Chemotaxis toward Environmental Pollutants: Role in Bioremediation," *Appl. Environ. Microbiol.*, vol. 68, no. 12, pp. 5789–5795, 2002.
- [2] D. H. Pieper and W. Reineke, "Engineering bacteria for bioremediation," *Curr. Opin. Biotechnol.*, vol. 11, pp. 262–270, 2000.
- [3] I. M. Head, D. M. Jones, and W. F. M. Röling, "Marine microorganisms make a meal of oil," *Nat. Rev. Microbiol.*, vol. 4, no. 3, pp. 173–182, 2006.
- [4] C. A. Silva-Valenzuela *et al.*, "Solid tumors provide niche-specific conditions that lead to preferential growth of *Salmonella*," *Oncotarget*, vol. 7, no. 23, pp. 35169–35180, 2016.
- [5] N. S. Forbes, "Engineering the perfect (bacterial) cancer therapy," *Nat. Rev. Cancer*, vol. 10, no. 11, pp. 785–794, 2010.
- [6] H. D. Lu *et al.*, "Modulating *Vibrio cholerae* Quorum-Sensing-Controlled Communication Using Autoinducer-Loaded Nanoparticles," *Nano Lett.*, vol. 15, no. 4, pp. 2235–2241, 2015.
- [7] B. M. Willardson *et al.*, "Development and Testing of a Bacterial Biosensor for Toluene-Based Environmental Contaminants Development and Testing of a Bacterial Biosensor for Toluene-Based Environmental Contaminants," *Appl. Environ. Microbiol.*, vol. 64, no. 3, pp. 1006–1012, 1998.
- [8] H. L. Jin, R. J. Mitchell, C. K. Byoung, D. C. Cullen, and B. G. Man, "A cell array biosensor for environmental toxicity analysis," *Biosens. Bioelectron.*, vol. 21, pp. 500–507, 2005.
- [9] K. Yagi, "Applications of whole-cell bacterial sensors in biotechnology and environmental science," *Appl. Microbiol. Biotechnol.*, vol. 73, no. 6, pp. 1251–1258, 2007.
- [10] H. Tani, K. Maehana, and T. Kamidate, "Chip-based bioassay using bacterial sensor strains immobilized in three-dimensional microfluidic network," *Anal. Chem.*, vol. 76, no. 22, pp. 6693–7, 2004.
- [11] M. Burmølle, J. S. Webb, D. Rao, L. H. Hansen, S. J. Sørensen, and S. Kjelleberg, "Enhanced biofilm formation and increased resistance to antimicrobial agents and bacterial invasion are caused by synergistic interactions in multispecies biofilms," *Appl. Environ. Microbiol.*, vol. 72, no. 6, pp. 3916–3923, 2006.
- [12] F. L. Hellweger, R. J. Clegg, J. R. Clark, C. M. Plugge, and J.-U. Kreft, "Advancing microbial sciences by individual-based modelling," *Nat. Rev. Microbiol.*, vol. 14, no. 7, pp. 461–471, 2016.
- [13] K. Brenner, L. You, and F. H. Arnold, "Engineering microbial consortia: a new frontier in synthetic biology," *Trends Biotechnol.*, vol. 26, no. 9, pp. 483–489, 2008.
- [14] T. Koide, W. L. Pang, and N. S. Baliga, "The role of predictive modelling in rationally re-engineering biological systems," *Nat. Rev. Microbiol.*, vol. 7, no. 41, pp. 297–305, 2009.

- [15] J. A. Shapiro, “Bacteria are small but not stupid: cognition, natural genetic engineering and socio-bacteriology,” *Stud. Hist. Philos. Sci. Part C Stud. Hist. Philos. Biol. Biomed. Sci.*, vol. 38, no. 4, pp. 807–819, 2007.
- [16] A. Persat *et al.*, “The mechanical world of bacteria,” *Cell*, vol. 161, no. 5, pp. 988–997, 2015.
- [17] P. Boyaval, S. Moineau, D. a Romero, and P. Horvath, “CRISPR Provides Acquired Resistance Against Viruses in Prokaryotes,” *Science*, vol. 315, no. 5819, pp. 1709–1712, 2007.
- [18] D. White, J. Drummond, and C. Fuqua, *The Physiology and Biochemistry of Prokaryotes*, 4th Ed. New York: Oxford University Press, 2012.
- [19] C. M. Waters and B. L. Bassler, “Quorum Sensing: Cell-to-Cell Communication in Bacteria,” *Annu. Rev. Cell Dev. Biol.*, vol. 21, no. 1, pp. 319–346, 2005.
- [20] F. C. Neidhardt, *Escherichia coli and Salmonella: Cellular and Molecular Biology*, 2nd ed. Washington: ASM Press, 1996.
- [21] R. M. Harshey, “Bacterial Motility on a Surface: Many Ways to a Common Goal,” *Annu. Rev. Microbiol.*, vol. 57, no. 1, pp. 249–273, 2003.
- [22] F. Jin, J. C. Conrad, M. L. Gibiansky, and G. C. L. Wong, “Bacteria use type-IV pili to slingshot on surfaces,” *Proc. Natl. Acad. Sci. U. S. A.*, vol. 108, pp. 12617–12622, 2011.
- [23] M. L. Gibiansky *et al.*, “Bacteria Use Type IV Pili to Walk Upright and Detach from Surfaces,” *Science*, vol. 330, no. 6001, p. 197, 2010.
- [24] B. Nan and D. R. Zusman, “Uncovering the Mystery of Gliding Motility in the Myxobacteria,” *Annu. Rev. Genet.*, vol. 45, no. 1, pp. 21–39, 2011.
- [25] M. Wartel and T. Mignot, “Nanomicrobiology,” in *Nanomicrobiology*, L. L. Barton, D. A. Bazylinski, and H. Xu, Eds. New York: Springer, 2014, pp. 127–143.
- [26] W. S. Ryu, R. M. Berry, and H. C. Berg, “Torque-generating units of the flagellar motor of *Escherichia coli* have a high duty ratio,” *Nature*, vol. 403, no. 6768, pp. 444–447, 2000.
- [27] H. C. Berg, *E. coli in Motion*. New York: Springer, 2004.
- [28] H. C. Berg, “The Rotary Motor of Bacterial Flagella,” *Annu. Rev. Biochem.*, vol. 72, no. 1, pp. 743–781, 2003.
- [29] P. P. Lele, B. G. Hosu, and H. C. Berg, “Dynamics of mechanosensing in the bacterial flagellar motor,” *Proc. Natl. Acad. Sci. U. S. A.*, vol. 110, pp. 11839–44, 2013.
- [30] M. F. Copeland and D. B. Weibel, “Bacterial swarming: a model system for studying dynamic self-assembly,” *Soft Matter*, vol. 5, no. 6, p. 1174, 2009.
- [31] R. M. Harshey and T. Matsuyama, “Dimorphic transition in *Escherichia coli* and *Salmonella typhimurium*: surface-induced differentiation into hyperflagellate swarmer cells,” *Proc. Natl. Acad. Sci. U. S. A.*, vol. 91, no. 18, pp. 8631–8635, 1994.
- [32] D. B. Kearns, “A field guide to bacterial swarming motility,” *Nat. Rev. Microbiol.*, vol. 8,

- no. 9, pp. 634–644, 2010.
- [33] E. M. Purcell, “Life at Low Reynolds Number,” *Am. J. Phys.*, vol. 45, no. 1, pp. 3–11, 1977.
- [34] M. A. Sleight, “Mechanisms of flagellar propulsion - A biologist’s view of the relation between structure, motion, and fluid mechanics,” *Protoplasma*, vol. 164, no. 1–3, pp. 45–53, 1991.
- [35] H. C. Berg, “Motile Behavior of Bacteria,” *Phys. Today*, vol. 53, pp. 24–30, 2000.
- [36] H. C. Berg and D. A. Brown, “Chemotaxis in *Escherichia coli* analysed by Three-dimensional Tracking,” *Nature*, vol. 239, no. 5374, pp. 500–504, 1972.
- [37] W. Tso and J. Adler, “Negative Chemotaxis in *Escherichia coli*,” *J. Bacteriol.*, vol. 118, no. 2, pp. 560–576, 1974.
- [38] T. M. Yi, Y. Huang, M. I. Simon, and J. Doyle, “Robust perfect adaptation in bacterial chemotaxis through integral feedback control,” *Proc. Natl. Acad. Sci.*, vol. 97, no. 9, pp. 4649–53, 2000.
- [39] J. Adler, “Chemotaxis in bacteria,” in *Biochemistry of Sensory Functions*, L. Jaenicke, Ed. Berlin Heidelberg: Springer, 1974, pp. 107–131.
- [40] B. Bassler and M. Miller, “Quorum Sensing,” in *The Prokaryotes*, 4th ed., Heidelberg: Springer, 2013, pp. 495–509.
- [41] R. J. Redfield, “Is quorum sensing a side effect of diffusion sensing?,” *Trends Microbiol.*, vol. 10, no. 8, pp. 365–370, 2002.
- [42] B. a Hense, C. Kuttler, J. Müller, M. Rothballer, A. Hartmann, and J. Kreft, “Does efficiency sensing unify diffusion and quorum sensing?,” *Nat. Rev. Microbiol.*, vol. 5, no. March, pp. 230–239, 2007.
- [43] K. Papenfort and B. L. Bassler, “Quorum sensing signal-response systems in Gram-negative bacteria,” *Nat. Rev. Microbiol.*, vol. 14, no. 9, pp. 576–88, 2016.
- [44] C. S. Pereira, J. A. Thompson, and K. B. Xavier, “AI-2-mediated signalling in bacteria,” *FEMS Microbiol. Rev.*, vol. 37, no. 2, pp. 156–181, 2013.
- [45] V. Sperandio, A. G. Torres, B. Jarvis, J. P. Nataro, and J. B. Kaper, “Bacteria-host communication: the language of hormones,” *Proc. Natl. Acad. Sci. U. S. A.*, vol. 100, pp. 8951–8956, 2003.
- [46] L. You, R. S. Cox, R. Weiss, and F. H. Arnold, “Programmed population control by cell-cell communication and regulated killing,” *Nature*, vol. 428, no. April, pp. 868–871, 2004.
- [47] S. Basu, Y. Gerchman, C. H. Collins, F. H. Arnold, and R. Weiss, “A synthetic multicellular system for programmed pattern formation,” *Nature*, vol. 434, no. 7037, pp. 1130–4, 2005.
- [48] J. C. Anderson, E. J. Clarke, A. P. Arkin, and C. a. Voigt, “Environmentally controlled invasion of cancer cells by engineered bacteria,” *J. Mol. Biol.*, vol. 355, pp. 619–627,

2006.

- [49] J. J. Tabor *et al.*, “A Synthetic Genetic Edge Detection Program,” *Cell*, vol. 137, no. 7, pp. 1272–1281, 2009.
- [50] L. Tsimring *et al.*, “A synchronized quorum of genetic clocks,” *Nature*, vol. 463, no. 7279, pp. 326–330, 2010.
- [51] A. Prindle, J. Selimkhanov, H. Li, I. Razinkov, L. S. Tsimring, and J. Hasty, “Rapid and tunable post-translational coupling of genetic circuits,” *Nature*, vol. 508, no. 7496, pp. 387–391, 2014.
- [52] A. Sahari, M. a Traore, A. M. Stevens, B. E. Scharf, and B. Behkam, “Towards Development of an Autonomous Network of BacteriaBots: Spatiotemporally High-Throughput Characterization of Bacterial Quorum-Sensing Response,” *Anal. Chem.*, vol. 86, no. 23, pp. 11489–11493, 2014.
- [53] X. Chen, X. Yang, M. Yang, and H. P. Zhang, “Dynamic clustering in suspension of motile bacteria,” *Europhys. Lett.*, vol. 111, no. 5, p. 54002, 2015.
- [54] Y. Dai, B. J. Toley, C. a. Swofford, and N. S. Forbes, “Construction of an inducible cell-communication system that amplifies Salmonella gene expression in tumor tissue,” *Biotechnol. Bioeng.*, vol. 110, no. 6, pp. 1769–1781, 2013.
- [55] Y. Cao *et al.*, “Collective Space-Sensing Coordinates Pattern Scaling in Engineered Bacteria,” *Cell*, vol. 165, no. 3, pp. 620–630, 2016.
- [56] J. Adler, “Chemotaxis in Bacteria,” *Science*, vol. 153, no. 3737, pp. 708–716, 1966.
- [57] R. M. Macnab and D. E. Koshland, “The gradient-sensing mechanism in bacterial chemotaxis,” *Proc. Natl. Acad. Sci. U. S. A.*, vol. 69, no. 9, pp. 2509–2512, 1972.
- [58] E. F. Keller and L. a Segel, “Traveling bands of chemotactic bacteria: a theoretical analysis,” *J. Theor. Biol.*, vol. 30, no. 2, pp. 235–248, 1971.
- [59] M. Rivero, R. Tranquillo, H. Buettner, and D. Lauffenburger, “Transport Models for Chemotactic cell populations based on individual behavior,” *Chem. Eng. Sci.*, vol. 44, no. 12, pp. 2881–2897, 1989.
- [60] L. a Segel, “A theoretical study of receptor mechanisms in bacterial chemotaxis,” *SIAM J. Appl. Math.*, vol. 32, no. 3, pp. 653–665, 1977.
- [61] W. Alt, “Biased Random Walk Models for Chemotaxis and Related Diffusion Approximations,” *J. Math. Biol.*, vol. 9, pp. 147–177, 1980.
- [62] M. a. Rivero, R. T. Tranquillo, H. M. Buettner, and D. a. Lauffenburger, “Transport models for chemotactic cell populations based on individual cell behavior,” *Chem. Eng. Sci.*, vol. 44, no. 12, pp. 2881–2897, 1989.
- [63] R. M. Ford and D. a Lauffenburger, “Measurement of bacterial random motility and chemotaxis coefficients: II. Application of single-cell-based mathematical model,” *Biotechnol. Bioeng.*, vol. 37, no. 7, pp. 661–672, 1991.

- [64] M. R. Evans *et al.*, “Do simple models lead to generality in ecology?,” *Trends Ecol. Evol.*, vol. 28, no. 10, pp. 578–583, 2013.
- [65] R. Dillon, L. Fauci, and D. Gaver III, “A Microscale Model of Bacterial Swimming , Chemotaxis and Substrate Transport,” *J. Theor. Biol.*, vol. 177, pp. 325–340, 1995.
- [66] M. M. Hopkins and L. J. Fauci, “A computational model of the collective fluid dynamics of motile micro-organisms,” *J. Fluid Mech.*, vol. 455, pp. 149–174, 2002.
- [67] J. U. Kreft, G. Booth, and J. W. T. Wimpenny, “BacSim, a simulator for individual-based modelling of bacterial colony growth,” *Microbiology*, vol. 144, no. 12, pp. 3275–3287, 1998.
- [68] J. U. Kreft, C. Picioreanu, J. W. Wimpenny, and M. C. van Loosdrecht, “Individual-based modelling of biofilms,” *Microbiology*, vol. 147, no. 11, pp. 2897–912, 2001.
- [69] R. Paton, R. Gregory, C. Vlachos, J. Saunders, and H. Wu, “Evolvable social agents for bacterial systems modeling,” *IEEE Trans. Nanobioscience*, vol. 3, no. 3, pp. 208–216, 2004.
- [70] D. Bray, M. D. Levin, and K. Lipkow, “The Chemotactic Behavior of Computer-Based Surrogate Bacteria,” *Curr. Biol.*, vol. 17, no. 1, pp. 12–19, 2007.
- [71] N. Vladimirov, L. Løvdok, D. Lebedez, and V. Sourjik, “Dependence of bacterial chemotaxis on gradient shape and adaptation rate,” *PLoS Comput. Biol.*, vol. 4, no. 12, 2008.
- [72] Y. V. Kalinin, L. Jiang, Y. Tu, and M. Wu, “Logarithmic Sensing in *Escherichia coli* Bacterial Chemotaxis,” *Biophys. J.*, vol. 96, no. 6, pp. 2439–2448, 2009.
- [73] D. a Brown and H. C. Berg, “Temporal stimulation of chemotaxis in *Escherichia coli*,” *Proc. Natl. Acad. Sci. U. S. A.*, vol. 71, no. 4, pp. 1388–1392, 1974.
- [74] T. M. Cickovski *et al.*, “A framework for three-dimensional simulation of morphogenesis,” *IEEE/ACM Trans. Comput. Biol. Bioinform.*, vol. 2, no. 4, pp. 273–288, 2005.
- [75] L. A. Lardon *et al.*, “iDynoMiCS: Next-generation individual-based modelling of biofilms,” *Environ. Microbiol.*, vol. 13, no. 9, pp. 2416–2434, 2011.
- [76] T. J. Rudge, P. J. Steiner, A. Phillips, and J. Haseloff, “Computational modeling of synthetic microbial biofilms,” *ACS Synth. Biol.*, vol. 1, no. 8, pp. 345–52, 2012.
- [77] T. J. Rudge, F. Federici, P. J. Steiner, A. Kan, and J. Haseloff, “Cell polarity-driven instability generates self-organized, fractal patterning of cell layers,” *ACS Synth. Biol.*, vol. 2, no. 12, pp. 705–714, 2013.
- [78] G. Wei, P. Bogdan, and R. Marculescu, “Efficient Modeling and Simulation of Bacteria-Based Nanonetworks with BNSim,” *IEEE J. Sel. Areas Commun.*, vol. 31, no. 12, pp. 868–878, 2013.
- [79] G. Wei, C. Lo, C. Walsh, N. L. Hiller, and R. Marculescu, “In Silico Evaluation of the Impacts of Quorum Sensing Inhibition (QSI) on Strain Competition and Development of

- QSI Resistance,” *Sci. Rep.*, vol. 6, p. 35136, 2016.
- [80] V. Arabagi, B. Behkam, E. Cheung, and M. Sitti, “Modeling of stochastic motion of bacteria propelled spherical microbeads,” *J. Appl. Phys.*, vol. 109, no. 11, p. 114702, 2011.
- [81] W. H. Press, B. P. Flannery, S. A. Teukolsky, and W. T. Vetterling, *Numerical Recipes in C: The Art of Scientific Computing*, 2nd ed. Cambridge: Cambridge University Press, 1992.
- [82] T. M. Squires and S. R. Quake, “Microfluidics: Fluid physics at the nanoliter,” *Rev. Mod. Phys.*, vol. 77, no. 3, pp. 977–1026, 2005.
- [83] K. M. Taute, S. Gude, S. J. Tans, and T. S. Shimizu, “High-throughput 3D tracking of bacteria on a standard phase contrast microscope,” *Nat. Commun.*, vol. 6, no. 8776, pp. 1–9, 2015.
- [84] E. Limpert, W. a. Stahel, and M. Abbt, “Log-normal Distributions across the Sciences: Keys and Clues,” *Bioscience*, vol. 51, no. 5, p. 341, 2001.
- [85] S. a. West, K. Winzer, A. Gardner, and S. P. Diggle, “Quorum sensing and the confusion about diffusion,” *Trends Microbiol.*, vol. 20, no. 12, pp. 586–594, 2012.
- [86] K. C. Heyde and W. C. Ruder, “Exploring Host-Microbiome Interactions using an in Silico Model of Biomimetic Robots and Engineered Living Cells,” *Sci. Rep.*, vol. 5, no. 11988, 2015.
- [87] C. A. Swofford, N. Van Dessel, and N. S. Forbes, “Quorum-sensing Salmonella selectively trigger protein expression within tumors,” *Proc. Natl. Acad. Sci. U. S. A.*, vol. 112, no. 11, pp. 3457–62, 2015.
- [88] A. Fekete *et al.*, “Dynamic regulation of N-acyl-homoserine lactone production and degradation in *Pseudomonas putida* IsoF,” *FEMS Microbiol. Ecol.*, vol. 72, no. 1, pp. 22–34, 2010.
- [89] B. A. Hense, J. Müller, C. Kuttler, and A. Hartmann, “Spatial heterogeneity of autoinducer regulation systems,” *Sensors*, vol. 12, no. 4, pp. 4156–4171, 2012.
- [90] B. P. Cormack, R. H. Valdivia, and S. Falkow, “FACS-optimized mutants of the green fluorescent protein (GFP),” *Gene*, vol. 173, no. 1, pp. 33–38, 1996.
- [91] J. H. J. Leveau and S. E. Lindow, “Predictive and Interpretive Simulation of Green Fluorescent Protein Expression in Reporter Bacteria,” *J. Bacteriol.*, vol. 183, no. 23, pp. 6752–6762, 2001.
- [92] H. B. Kaplan and E. P. Greenberg, “Diffusion of Autoinducer is Involved in Regulation of the *Vibrio fischeri* Luminescence System,” *J. Bacteriol.*, vol. 163, no. 3, pp. 1210–1214, 1985.
- [93] K. Drescher, J. Dunkel, L. H. Cisneros, S. Ganguly, and R. E. Goldstein, “Fluid dynamics and noise in bacterial cell – cell and cell – surface scattering,” *Proc. Natl. Acad. Sci.*, vol. 108, pp. 10940–10945, 2011.

- [94] X. L. Wu and A. Libchaber, “Particle diffusion in a quasi-two-dimensional bacterial bath,” *Phys. Rev. Lett.*, vol. 84, no. 13, pp. 3017–3020, 2000.
- [95] M. J. Kim and K. S. Breuer, “Enhanced diffusion due to motile bacteria,” *Phys. Fluids*, vol. 16, no. 2004, p. L78, 2004.
- [96] G. Miño *et al.*, “Enhanced diffusion due to active swimmers at a solid surface,” *Phys. Rev. Lett.*, vol. 106, no. 4, pp. 1–4, 2011.
- [97] A. Jepson, V. A. Martinez, J. Schwarz-Linek, A. Morozov, and W. C. K. Poon, “Enhanced diffusion of nonswimmers in a three-dimensional bath of motile bacteria,” *Phys. Rev. E*, vol. 88, no. 4, pp. 3–7, 2013.
- [98] G. L. Miño, J. Dunstan, A. Rousselet, E. Clement, and R. Soto, “Induced Diffusion of Tracers in a Bacterial Suspension: Theory and Experiments,” *J. Fluid Mech*, p. 20, 2013.
- [99] T. V. Kasyap, D. L. Koch, and M. Wu, “Hydrodynamic tracer diffusion in suspensions of swimming bacteria,” *Phys. Fluids*, vol. 26, no. 8, 2014.
- [100] Y. H. Dong, J. L. Xu, X. Z. Li, and L. H. Zhang, “AiiA, an enzyme that inactivates the acylhomoserine lactone quorum-sensing signal and attenuates the virulence of *Erwinia carotovora*,” *Proc. Natl. Acad. Sci. U. S. A.*, vol. 97, no. 7, pp. 3526–31, 2000.
- [101] C. Grandclement, M. Tannieres, S. Morera, Y. Dessaux, and D. Faure, “Quorum quenching: Role in nature and applied developments,” *FEMS Microbiol. Rev.*, vol. 40, no. 1, pp. 86–116, 2015.
- [102] J. Anderson, *Computational Fluid Dynamics*, 1st ed. New York: McGraw-Hill, 1995.
- [103] M. A. Traore and B. Behkam, “A PEG-DA microfluidic device for chemotaxis studies,” *J. Micromechanics Microengineering*, vol. 23, no. 8, p. 85014, 2013.
- [104] T. Ahmed, T. S. Shimizu, and R. Stocker, “Bacterial chemotaxis in linear and nonlinear steady microfluidic gradients,” *Nano Lett.*, vol. 10, no. 9, pp. 3379–85, 2010.
- [105] S. Suh, M. A. Traore, and B. Behkam, “Bacterial Chemotaxis Enabled Autonomous Sorting of Nanoparticles of Comparable Sizes,” *Lab Chip*, vol. 16, no. 7, 2015.
- [106] A. Sahari, M. a Traore, B. E. Scharf, and B. Behkam, “Directed transport of bacteria-based drug delivery vehicles: bacterial chemotaxis dominates particle shape.,” *Biomed. Microdevices*, vol. 16, pp. 717–725, 2014.
- [107] A. Untergasser, R. Geurts, and H. Franssen, “pHC60 - a very stable plasmid for fluorescence microscopy.” NCBI GenBank Entry, 2008.
- [108] C. S. Barker, B. M. Prüß, and P. Matsumura, “Increased motility of *Escherichia coli* by insertion sequence element integration into the regulatory region of the *flhD* operon,” *J. Bacteriol.*, vol. 186, no. 22, pp. 7529–7537, 2004.
- [109] S. R. Sternberg, “Biomedical Image Processing,” *Computer*, vol. 16, no. 1, pp. 22–34, 1983.
- [110] J. Bernsen, “Dynamic thresholding of grey-level images,” in *International Conference on*

- Pattern Recognition*, 1986, pp. 1251–1255.
- [111] R. Storn and K. Price, “Differential Evolution – A Simple and Efficient Heuristic for Global Optimization over Continuous Spaces,” *J. Glob. Optim.*, vol. 11, no. 4, pp. 341–359, 1997.
- [112] V. Sourjik and H. C. Berg, “Receptor sensitivity in bacterial chemotaxis.,” *Proc. Natl. Acad. Sci. U. S. A.*, vol. 99, no. 1, pp. 123–127, 2002.
- [113] S. Clarke and D. E. Koshland, “Membrane Receptors for Aspartate and Serine in Bacterial Chemotaxis,” *J. Biol. Chem.*, vol. 254, no. 19, pp. 9695–9702, 1979.
- [114] N. A. Licata, B. Mohari, C. Fuqua, and S. Setayeshgar, “Diffusion of Bacterial Cells in Porous Media,” *Biophys. J.*, vol. 110, no. 1, pp. 247–257, 2016.
- [115] A. J. Wolfe and H. C. Berg, “Migration of bacteria in semisolid agar.,” *Proc. Natl. Acad. Sci. U. S. A.*, vol. 86, no. 18, pp. 6973–6977, 1989.
- [116] J. W. Williams, X. Cui, A. Levchenko, and A. M. Stevens, “Robust and sensitive control of a quorum-sensing circuit by two interlocked feedback loops.,” *Mol. Syst. Biol.*, vol. 4, no. 234, p. 234, 2008.
- [117] E. L. Haseltine and F. H. Arnold, “Implications of Rewiring Bacterial Quorum Sensing,” *Appl. Environ. Microbiol.*, vol. 74, no. 2, pp. 437–445, 2008.
- [118] A. B. Goryachev, D. J. Toh, and T. Lee, “Systems analysis of a quorum sensing network: Design constraints imposed by the functional requirements , network topology and kinetic constants,” *Biosystems.*, vol. 83, no. 2, pp. 178–187, 2005.
- [119] J. C. Waters, “Accuracy and precision in quantitative fluorescence microscopy,” *J. Cell Biol.*, vol. 185, no. 7, pp. 1135–1148, 2009.
- [120] D. L. Englert, M. D. Manson, and A. Jayaraman, “Investigation of bacterial chemotaxis in flow-based microfluidic devices,” *Nat. Protoc.*, vol. 5, no. 5, pp. 864–872, 2010.
- [121] N. Periasamy and a S. Verkman, “Analysis of fluorophore diffusion by continuous distributions of diffusion coefficients: application to photobleaching measurements of multicomponent and anomalous diffusion.,” *Biophys. J.*, vol. 75, no. 1, pp. 557–67, 1998.
- [122] D. S. Banks and C. Fradin, “Anomalous Diffusion of Proteins Due to Molecular Crowding,” *Biophys. J.*, vol. 89, no. 5, pp. 2960–2971, 2005.
- [123] C. Culbertson, “Diffusion coefficient measurements in microfluidic devices,” *Talanta*, vol. 56, no. 2, pp. 365–373, 2002.
- [124] R. Shetty, M. Lizarazo, R. Rettberg, and T. F. Knight, “Assembly of BioBrick Standard Biological Parts Using Three Antibiotic Assembly,” in *Methods in Enzymology*, 1st ed., vol. 498, Elsevier Inc., 2011, pp. 311–326.
- [125] J. B. Andersen, C. Sternberg, L. K. Poulsen, S. P. Bjørn, M. Givskov, and S. Molin, “New unstable variants of green fluorescent protein for studies of transient gene expression in bacteria,” *Appl. Environ. Microbiol.*, vol. 64, no. 6, pp. 2240–2246, 1998.

- [126] Y. I. Kim, R. E. Burton, B. M. Burton, R. T. Sauer, and T. a Baker, “Dynamics of substrate denaturation and translocation by the ClpXP degradation machine.,” *Mol. Cell*, vol. 5, no. 4, pp. 639–648, 2000.
- [127] T. A. Baker and R. T. Sauer, “ClpXP, an ATP-powered unfolding and protein-degradation machine,” *Biochim. Biophys. Acta - Mol. Cell Res.*, vol. 1823, no. 1, pp. 15–28, 2012.
- [128] J. B. O. Andersen *et al.*, “gfp -Based N -Acyl Homoserine-Lactone Sensor Systems for Detection of Bacterial Communication,” *Appl. Environ. Microbiol.*, vol. 67, no. 2, pp. 575–585, 2001.
- [129] P. V Dunlap and J. M. Ray, “Requirement for Autoinducer in Transcriptional Negative Autoregulation of the *Vibrio fischeri luxR* Gene in *Escherichia coli*,” *J. Bacteriol.*, vol. 171, no. 6, pp. 3549–3552, 1989.
- [130] R. Iizuka, M. Yamagishi-Shirasaki, and T. Funatsu, “Kinetic study of de novo chromophore maturation of fluorescent proteins,” *Anal. Biochem.*, vol. 414, no. 2, pp. 173–178, 2011.
- [131] P. S. Stewart, “Diffusion in Biofilms,” *J. Bacteriol.*, vol. 185, no. 5, pp. 1485–1491, 2003.
- [132] A. Pai and L. You, “Optimal tuning of bacterial sensing potential.,” *Mol. Syst. Biol.*, vol. 5, no. 286, p. 286, 2009.
- [133] L. H. Wang, L. X. Weng, Y. H. Dong, and L. H. Zhang, “Specificity and Enzyme Kinetics of the Quorum-quenching N-Acyl Homoserine Lactone Lactonase (AHL-lactonase),” *J. Biol. Chem.*, vol. 279, no. 14, pp. 13645–13651, 2004.
- [134] H. M. Salis, E. a Mirsky, and C. a Voigt, “Automated design of synthetic ribosome binding sites to control protein expression,” *Nat. Biotechnol.*, vol. 27, no. 10, pp. 946–950, 2009.
- [135] A. Espah Borujeni, A. S. Channarasappa, and H. M. Salis, “Translation rate is controlled by coupled trade-offs between site accessibility, selective RNA unfolding and sliding at upstream standby sites,” *Nucleic Acids Res.*, vol. 42, no. 4, pp. 2646–2659, 2014.
- [136] R. P. Futrelle and H. C. Berg, “Specification of Gradients used for Studies of Chemotaxis,” *Nature*, vol. 238, p. 37, 1972.
- [137] H. Alper, C. Fischer, E. Nevoigt, and G. Stephanopoulos, “Tuning genetic control through promoter engineering,” *Proc. Natl. Acad. Sci.*, vol. 102, no. 36, pp. 12678–12683, 2005.
- [138] M. R. Schlabach, J. K. Hu, M. Li, and S. J. Elledge, “Synthetic design of strong promoters,” *Proc. Natl. Acad. Sci.*, vol. 107, no. 6, pp. 2538–2543, 2010.
- [139] Y. Lu, “Engineering *Vibrio fischeri* transcriptional activator LuxR for diverse transcriptional activities,” *Biotechnol. Lett.*, vol. 38, no. 9, pp. 1459–1463, 2016.
- [140] C. H. Collins, J. R. Leadbetter, and F. H. Arnold, “Dual selection enhances the signaling specificity of a variant of the quorum-sensing transcriptional activator LuxR,” *Nat. Biotechnol.*, vol. 24, no. 6, pp. 708–712, 2006.
- [141] M. O. Din *et al.*, “Synchronized cycles of bacterial lysis for in vivo delivery,” *Nature*, vol.

536, no. 7614, pp. 81–5, 2016.

- [142] J. Stritzker *et al.*, “Enterobacterial tumor colonization in mice depends on bacterial metabolism and macrophages but is independent of chemotaxis and motility,” *Int. J. Med. Microbiol.*, vol. 300, no. 7, pp. 449–456, 2010.
- [143] D. N. Thornlow, E. L. Brackett, J. M. Gigas, N. Van Dessel, and N. S. Forbes, “Persistent enhancement of bacterial motility increases tumor penetration,” *Biotechnol. Bioeng.*, vol. 112, no. 11, pp. 2397–2405, 2015.
- [144] R. W. Kasinskas and N. S. Forbes, “*Salmonella typhimurium* specifically chemotax and proliferate in heterogeneous tumor tissue in vitro,” *Biotechnol. Bioeng.*, vol. 94, no. 4, pp. 710–721, 2006.
- [145] R. M. Macnab and M. K. Ornston, “Normal-to-curly flagellar transitions and their role in bacterial tumbling. Stabilization of an alternative quaternary structure by mechanical force,” *J. Mol. Biol.*, vol. 112, no. 1, pp. 1–30, 1977.